A determination of Δm from tagged neutral kaons

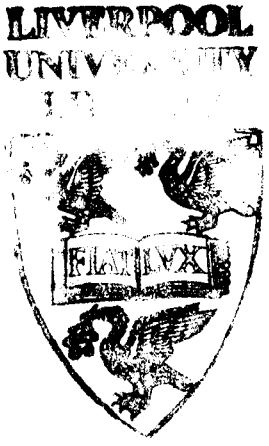

Thesis submitted in accordance with the
requirements of the University of Liverpool for
the degree of Doctor in Philosophy by

Paul David Maley

September 1992

A determination of Δm from tagged neutral kaons

Paul David Maley

September 1992

Abstract

The CPLEAR experiment is a high precision experiment aiming to measure several CP violating parameters in the neutral kaon system.

In order to decouple the errors on the phase angles of these parameters with the error on the $K_L - K_S$ mass difference (Δm), the experiment will also make a measurement of Δm from semileptonic neutral kaon decays. This thesis describes a preliminary determination of Δm from a time dependent asymmetry in the semileptonic decays of tagged K^0s and $\bar{K}^0$s.

In order to select a sample of semileptonic decays it was necessary to develop a method of separating electron and pion tracks. The electromagnetic calorimeter can only separate electrons and pions at momenta above 200 MeV/c. In this thesis the development of a method of separating the two types of particle at momenta below 250 MeV/c is also described.

From data collected between September 1990 and October 1991, a sample of 45 000 semileptonic decays has been isolated and a value of the mass difference determined to be

$$\Delta m/\gamma_S = 0.477 \pm 0.016(\text{stat.}) \left.\begin{matrix} +0.004 \\ -0.001 \end{matrix}\right\} (\text{syst.})$$

Blank Page

Acknowledgments

This thesis is the culmination of four years work and would never have been finished but for the help and support of many people. I would like to take this opportunity to thank a few of them.

I am indebted to my supervisor, Erwin Gabathuler, for giving me the opportunity to do this Ph.D.. He has provided guidance when necessary but also left me with the freedom to develop and find my own way forward, for which I am very grateful.

I would like to thank all the many friends that I have made in Liverpool and who have made life there so much fun. In particular I would like to thank Peter Sanders, Tony Campion, Douglas Gillespie and Jim Bennet for many good times, also Emmet Cawley, Joao Carvalho and José da Cunha.

Thanks to Michael Dodgson and Dave Francis for reading this thesis and providing many helpful comments and corrections.

Thanks also to the Chief, Chris Bee, not only for looking after me and keeping me busy during my time at CERN, but also for an epic trip down the Vallée Blanche.

All of the work in this thesis is based on data collected by the CPLEAR experiment and I would like to thank all of my fellow collaborators who made the experiment and this thesis possible.

Finally I would like to thank my family, especially my parents, without whom this thesis would never have been started, never mind finished. Over the years they have been a constant source of love, support and encouragement. I know that in the past they have sacrificed many things so that I may be where I am now. I could not have got here alone. Thank you.

Blank Page

Contents

Chapter 1

Introduction

1.1 Outline

The existence of CP violation has been experimentally well established for over a quarter of a century, but despite considerable experimental and theoretical effort, its origin is still an open question.

Within the framework of the Standard Model, CP violation has its sole origin in the Cabibbo-Kobayashi-Maskawa (CKM) matrix [1] — the matrix of complex coupling constants between quark currents and the charged electroweak gauge fields. Though there exists at present no evidence contrary to Standard Model predictions, the model itself is unsatisfactory because of the large number of arbitrary parameters that it contains. The CKM matrix is determined by four of these parameters, and thus the Standard Model makes no prediction as to the magnitude of CP violating effects in weak interaction processes. Other models exist to explain the occurrence and magnitude of CP violation, but the current precision of experimental measurements is insufficient to distinguish between these and the Standard Model.

The CPLEAR experiment [2] aims to contribute to the search for the origin of CP violation by making precise measurements of CP violating parameters in the neutral kaon system. Using a source of tagged neutral kaons, i.e. kaons of known initial strangeness, the experiment is designed to study interference phenomena in all of the major neutral kaon decay modes.

In CPLEAR tagged neutral kaons are created from proton-antiproton annihilations at rest to

$$p\bar{p} \longrightarrow \begin{cases} K^-\pi^+K^0 \\ K^+\pi^-\bar{K}^0 \end{cases}$$

Since strangeness is conserved in strong interaction processes, the detection of a single charged kaon (i.e. not $K^+K^-X^0$ annihilations) implies the existence of a neutral kaon. The strangeness of that neutral kaon can be inferred from the strangeness of the charged kaon, i.e. from its charge.

The small, $O(10^{-3})$, branching ratios to kaonic final states means a high statistics experiment is only possible at a machine capable of providing a high flux of low energy antiprotons. The LEAR (Low Energy Antiproton Ring) facility [3] at CERN is such a machine, providing 2×10^6 antiprotons per second at a momentum of 200 MeV/c.

If a neutral kaon decays within the detector, the final state may be identified and the event fully reconstructed. That is, the initial strangeness of the neutral kaon is tagged, the final decay state identified and the time between the creation and the decay of the neutral kaon determined. The CP violating parameters of interest may then be extracted from the data by constructing asymmetries between the rates of K^0 and $\bar{K}^0$ decays as a function of decay time. Typically these parameters are complex and their phase angles, ϕ_f, enter the asymmetries in the form

$$\cos(\Delta m t - \phi_f)$$

where $\Delta m = m_L - m_S$ is the mass difference between the long and short lived eigenstates and t is the decay time. The determination of these angles is thus correlated with and limited by a determination of the $K_L - K_S$ mass difference.

The work presented in this thesis was done with two main aims in mind:

- To develop an algorithm to separate electrons from pions at low momenta.
- To use this algorithm to isolate a sample of semileptonic neutral kaons decays, and to use these events to obtain a preliminary measurement of the $K_L - K_S$ mass difference.

Using data collected in CPLEAR between September and November 1990 and between May and October 1991 I have determined a value for the mass difference of†

$$\Delta m/\gamma_S = 0.477 \pm 0.016$$

with a systematic uncertainty of 4×10^{-3}. The systematic uncertainty is largely a result of low statistics and will scale down as the volume of data increases.

The precision of this result is not comparable with previous measurements, see figure 1.1, but the ultimate goal of the experiment is to make a measurement with a fractional error of the order of $2-3\times 10^{-3}$. The results shown graphically in figure 1.1 are taken from reference [4] where an average over these three results is also quoted

Reference	$\Delta m/\gamma_S$
CULLEN 70 [5]	0.484 ± 0.005
GEWENIGER 74C [6]	0.4764 ± 0.0027
GJESDAL 74 [7]	0.4759 ± 0.0036
World average [4]	0.4772 ± 0.0020

Results prior to these can be found in reference [8].

The sign of the mass difference, $m_L - m_S$, cannot be determined from the data in this thesis. This is because the semileptonic decay rates depend only on $\cos(\Delta m t)$ (see next section) and this is the same for both signs of Δm. In this thesis Δm should be read $|\Delta m|$. The sign of the mass difference has been determined previously from regeneration type experiments, for example see reference [10].

1.2 Theory of strangeness oscillations

This thesis is primarily concerned with the semileptonic decays of neutral kaons, i.e. decays to final states such as $\pi^+ e^- \bar{\nu}$ and $\pi^- e^+ \nu$. This type of decay is interesting, because the $\Delta S = \Delta Q$ rule offers the possibility to tag the strangeness of a neutral kaon at its decay vertex, in addition to its already tagged initial strangeness. Since strangeness is not conserved by the weak interactions, a neutral kaon of initially well

†Both Δm and γ_S are measured in units of inverse seconds (see next section) and thus $\Delta m/\gamma_S$ is dimensionless.

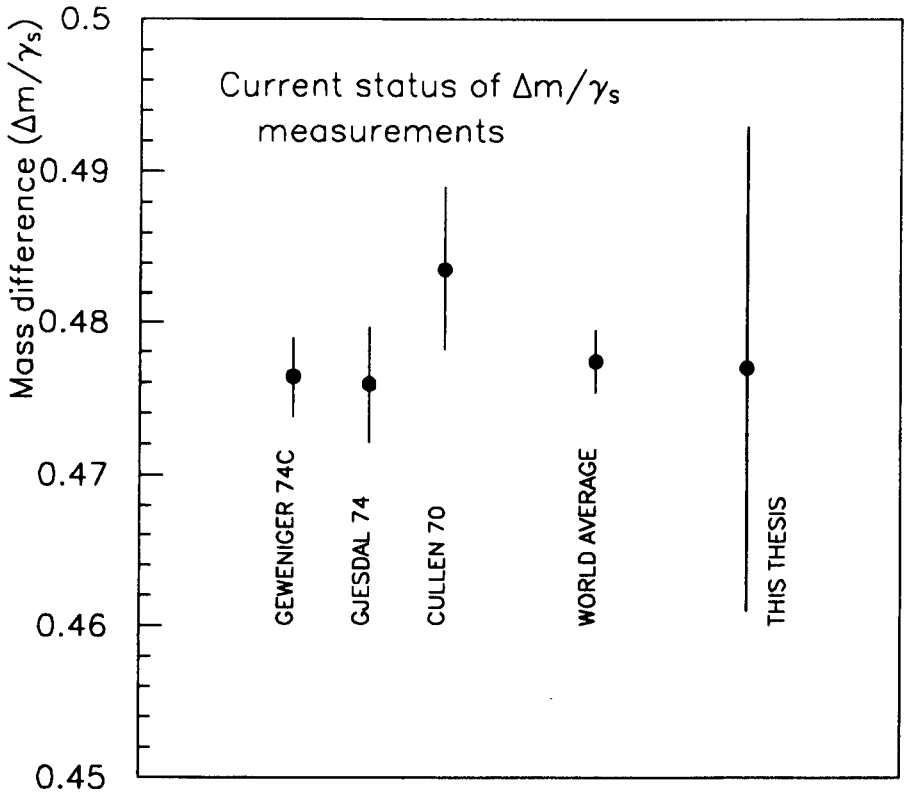

Figure 1.1: Current status of $\Delta m/\gamma_S$ measurements.

defined strangeness will evolve into a linear combination of both K^0 and $\bar{K}^0$ states. Thus using semileptonic decays

$$\begin{aligned} K^0(0) &\to \pi^{\pm} e^{\mp} \nu(t) \\ \bar{K}^0(0) &\to \pi^{\pm} e^{\mp} \nu(t) \end{aligned} \tag{1.1}$$

it is possible to measure the transition rates for $K^0 \to K^0$, $K^0 \to \bar{K}^0$ etc., as a function of time, i.e. to observe neutral kaon strangeness oscillations.

In the Standard Model the $\Delta S = \Delta Q$ rule is a result of the form of the weak charged current vertex [9], see figure 1.2. In the absence of flavour changing neutral

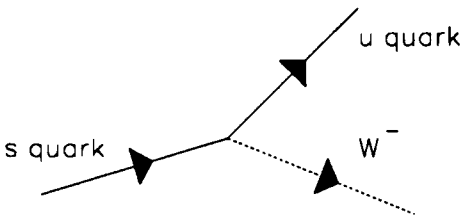

Figure 1.2: Strange quark coupling to an up quark and a W^- vector boson. The amplitude for this vertex contains a factor V_{us} — a CKM matrix element.

currents, a strange quark can decay only to an up quark, and to conserve charge the weak gauge boson radiated must be negatively charged. Similarly an $\bar{s}$ antiquark would decay to a $\bar{u}$ antiquark radiating a W^+. The sign of the final state lepton is the same as that of the gauge boson. Thus a $K^0(d\bar{s})$ can decay to $\pi^- e^+ \nu$, while a $\bar{K}^0(\bar{d}s)$ can decay to $\pi^+ e^- \bar{\nu}$. These are the so called $\Delta S = \Delta Q$ transitions. The decays $K^0 \rightarrow \pi^+ e^- \bar{\nu}$ and $\bar{K}^0 \rightarrow \pi^- e^+ \nu$ ($\Delta S = -\Delta Q$ transitions) are second order weak interactions and thus effectively forbidden.

Phenomenologically the occurrence of $\Delta S = -\Delta Q$ transitions may be parameterized by χ_l and $\overline{\chi}_l$ (l can be either an electron or a muon) where

$$\overline{\chi}_l = \frac{\langle \pi^+ l^- \overline{\nu} | H_W | K^0 \rangle}{\langle \pi^+ l^- \overline{\nu} | H_W | \bar{K}^0 \rangle}$$

$$\chi_l = \frac{\langle \pi^- l^+ \nu | H_W | \bar{K}^0 \rangle}{\langle \pi^- l^+ \nu | H_W | K^0 \rangle}$$

which are related by CPT symmetry: $\overline{\chi}_l = \chi_l^*$. The current best measurements of χ_e are[†] [4]

$$Re(\chi_e) = 0.006 \pm 0.018$$

$$Im(\chi_e) = -0.003 \pm 0.026$$

[†] For $\pi e \nu$ final states χ_e is equal (to an accuracy of $\sim 0.1\%$) to another parameter x. It is the values of $Re(x)$ and $Im(x)$ that I quote here from the Particle Data Book. For a good account of semileptonic form factors, i.e. x and χ_l etc. see reference [11].

In the Standard Model, $\Delta S = -\Delta Q$ transitions are the possible through second order weak transitions and thus $|\chi_e|$ is of the order of 10^{-6} [12], consistent with the above measurements.

There is no evidence for violations of the $\Delta S = \Delta Q$ rule from other decays, e.g. [4]

$$\frac{\Gamma(K^+ \to \pi^+\pi^+e^-\bar{\nu})}{\Gamma(K^+ \to \text{ all})} < 1.2 \times 10^{-8}$$

In this thesis I take $\Delta S = -\Delta Q$ transitions to be absolutely forbidden.

The actual calculation of the decay rates is straight forward. It is simplest to work in the basis of the eigenstates of the Hamiltonian, $\{|K_L\rangle, |K_S\rangle\}$, since as these states propagate through time they simply pick up a phase factor. A state which is initially a linear combination of these states

$$|\psi(0)\rangle = \alpha_L|K_L\rangle + \alpha_S|K_S\rangle$$

will evolve into a state

$$\begin{aligned} |\psi(t)\rangle &= e^{-iHt}|\psi(0)\rangle \\ &= \alpha_L e^{-i\lambda_L t}|K_L\rangle + \alpha_S e^{-i\lambda_S t}|K_S\rangle \end{aligned} \tag{1.2}$$

where λ_S and λ_L are the eigenvalues of the eigenstates of the Hamiltonian. Since these states decay, the eigenvalues are complex

$$\lambda_{L,S} = m_{L,S} + i\gamma_{L,S}/2$$

where m is the mass and γ is the total width of the state.

The masses and widths as defined here are both measured in units of inverse seconds. The quantity $\Delta m/\gamma_S$ is therefore dimensionless.

To calculate transition amplitudes for processes where $|\psi(0)\rangle$ and $|\psi(t)\rangle$ are states of definite strangeness, $|K_L\rangle$ and $|K_S\rangle$ must be expressed in terms of the strangeness basis

$$\begin{aligned} |K_S\rangle &= p|K^0\rangle + q|\bar{K}^0\rangle \\ |K_L\rangle &= r|K^0\rangle + s|\bar{K}^0\rangle \end{aligned} \tag{1.3}$$

where p, q, r and s are such that $|K_L\rangle$ and $|K_S\rangle$ are normalized. Since $|K^0\rangle$ and $|\bar{K}^0\rangle$ are distinct states, the relative phases of p and q and of r and s are arbitrary; only $|p/q|$ and $|r/s|$ are observable, and these are determined by the symmetry properties of the Hamiltonian.

Using equations 1.2 and 1.3 the following amplitudes may be calculated

$$\begin{aligned}
\langle K^0(t)|K^0(0)\rangle &= \frac{1}{qr-sp}\left(rqe^{-i\lambda_L t} - spe^{-i\lambda_S t}\right) \\
\langle \bar{K}^0(t)|K^0(0)\rangle &= \frac{sq}{qr-sp}\left(e^{-i\lambda_L t} - e^{-i\lambda_S t}\right) \\
\langle K^0(t)|\bar{K}^0(0)\rangle &= \frac{-rp}{qr-sp}\left(e^{-i\lambda_L t} - e^{-i\lambda_S t}\right) \\
\langle \bar{K}^0(t)|\bar{K}^0(0)\rangle &= \frac{-1}{qr-sp}\left(spe^{-i\lambda_L t} - rqe^{-i\lambda_S t}\right)
\end{aligned} \tag{1.4}$$

where, say $\langle K^0(t)|\bar{K}^0(0)\rangle$ represents the amplitude for a neutral kaon which is initially a $\bar{K}^0$ to be a K^0 at time t.

The $\Delta S = \Delta Q$ rule, links the amplitudes in equation 1.4 in one to one correspondence with the four processes of 1.1. Defining

$$\begin{aligned}
A &= \langle \pi^- l^+ \nu | H_W | K^0\rangle \\
\bar{A} &= \langle \pi^+ l^- \bar{\nu} | H_W | \bar{K}^0\rangle
\end{aligned}$$

we have

$$\langle \pi^- e^+ \nu(t)|K^0(0)\rangle = A\langle K^0(t)|K^0(0)\rangle$$

and similarly for the other three processes.

If we assume that CPT symmetry holds, then for any process

$$\langle \psi_2|e^{-iHt}|\psi_1\rangle = \langle \Theta\psi_1|e^{-iHt}|\Theta\psi_2\rangle$$

where the state $|\Theta\psi\rangle$ is the CPT transformed state $|\psi\rangle$ and is formed by replacing all particles with their antiparticles and reversing their spins. Applying this theorem to the process $K^0(0) \rightarrow K^0(t)$ we have

$$\langle K^0|e^{-iHt}|K^0\rangle = \langle \bar{K}^0|e^{-iHt}|\bar{K}^0\rangle$$

which from the amplitudes of equation 1.4 implies

$$r/s = -p/q$$

Combining this with the normalization condition on $|K_L\rangle$ and $|K_S\rangle$ gives $|p| = |r|$. Invariance under CPT implies that $A^* = \bar{A}$, and thus $|\bar{A}|^2 = |A|^2$.

If in addition the Hamiltonian was CP symmetric, then we would have

$$\langle K^0|e^{-iHt}|\bar{K}^0\rangle = \langle \bar{K}^0|e^{-iHt}|K^0\rangle$$

giving

$$r/s = -q/p$$

which when combined with the CPT constraint gives $p = \pm q$. Thus $|p/q| \neq 1$ is a measure of CP violation.

The probabilities for the processes are given by the modulus squared of the amplitudes, for example

$$\begin{aligned} |\langle \pi^- e^+ \nu(t)|K^0(0)\rangle|^2 &= |A|^2 \, |\langle K^0(t)|K^0(0)\rangle|^2 \\ &= \frac{1}{4}|A|^2 \left|e^{-i\lambda_L t} + e^{-i\lambda_S t}\right|^2 \\ &= \frac{1}{4}|A|^2 \left(e^{-\gamma_S t} + e^{-\gamma_L t} + e^{-\frac{1}{2}(\gamma_S+\gamma_L)t}\cos(\Delta m t)\right) \end{aligned}$$

where $\Delta m = m_L - m_S$. Defining $f(t)$ and $g(t)$ by

$$\begin{aligned} f(t) &= e^{-\gamma_L t} + e^{-\gamma_S t} + 2e^{-\frac{1}{2}(\gamma_L+\gamma_S)t}\cos(\Delta m t) \\ g(t) &= e^{-\gamma_L t} + e^{-\gamma_S t} - 2e^{-\frac{1}{2}(\gamma_L+\gamma_S)t}\cos(\Delta m t) \end{aligned}$$

we can calculate similarly

$$\begin{aligned} |\langle \pi^- e^+ \nu(t)|K^0(0)\rangle|^2 &= \frac{1}{4}|A|^2 f(t) \\ |\langle \pi^+ e^- \bar{\nu}(t)|K^0\rangle|^2 &= \frac{1}{4}|\bar{A}|^2 \left|\frac{q}{p}\right|^2 g(t) \\ |\langle \pi^- e^+ \nu(t)|\bar{K}^0(0)\rangle|^2 &= \frac{1}{4}|A|^2 \left|\frac{p}{q}\right|^2 g(t) \\ |\langle \pi^+ e^- \bar{\nu}(t)|\bar{K}^0\rangle|^2 &= \frac{1}{4}|\bar{A}|^2 f(t) \end{aligned}$$

the quantity $|p/q|$ can be related to the more commonly used parameter $Re(\epsilon)$ through the lepton charge asymmetry, δ_l

$$\delta_l = \frac{N_{l+} - N_{l-}}{N_{l+} + N_{l-}}$$

where N_{l+} (N_{l-}) is the number of semileptonic decays to positive (negative) leptons. At large decay times, in the absence of $\Delta S = -\Delta Q$ transitions, $\delta_l \to 2Re(\epsilon)$ [11, page 79], which using the asymptotic values of the above rates may be inverted to give $|p/q|^2 = 1 + 4Re(\epsilon)$ and $|q/p|^2 = 1 - 4Re(\epsilon)$.

The value of $|A|^2$ may be deduced by summing over all four rates giving

$$\Gamma_{\text{All semileptonic}}(t) = |A|^2 \left(e^{-\gamma_L t} + e^{-\gamma_S t}\right)$$

which considering the long decay time limit gives $|A|^2 = \gamma_L BR(K_L \to \pi e\nu)$, hereafter denoted $W_{\pi e\nu}$.

For clarity I label the decay rates according to the charges of the particles used to tag the event. At the primary vertex a $K^+(K^-)$ tags the neutral kaon as $\bar{K}^0(K^0)$, while at the decay vertex an $e^+(e^-)$ tags the kaon as $K^0(\bar{K}^0)$. Thus I denote the rate $|\langle \pi^- e^+ \nu(t)|K^0(0)\rangle|^2$ by $N(K^- e^+)(t)$ and similarly for the others.

$$\begin{aligned}
N(K^+e^+) &= \frac{1}{4} W_{\pi e\nu}(1 + 4Re(\epsilon))g(t) \\
N(K^+e^-) &= \frac{1}{4} W_{\pi e\nu} f(t) \\
N(K^-e^+) &= \frac{1}{4} W_{\pi e\nu} f(t) \\
N(K^-e^-) &= \frac{1}{4} W_{\pi e\nu}(1 - 4Re(\epsilon))g(t)
\end{aligned}$$

Since the acceptance of the detector is a function of the neutral kaon decay time, the measured transition rates will differ from those calculated above. In order to cancel out the detector acceptance, the ratios of these rates can be used, thus I define a time dependent asymmetry $A_0(t)$.

$$A_0 = \frac{N(\Delta S = 0) - N(\Delta S = \pm 2)}{N(\Delta S = 0) + N(\Delta S = \pm 2)}$$

where the two rates $N(\Delta S = 0)$ and $N(\Delta S = \pm 2)$ are given by

$$\begin{aligned}
N(\Delta S = 0) &= N(K^-e^+) + N(K^+e^-) \\
N(\Delta S = \pm 2) &= N(K^+e^+) + N(K^-e^-)
\end{aligned}$$

i.e. the four decay rates are grouped into two pairs; those where the neutral kaon has the same strangeness at both vertices ($\Delta S = 0$) and those where the strangeness changes ($\Delta S = \pm 2$). These are shown in figure 1.3.

Substituting in the explicit forms for the transition rates gives the asymmetry as

$$A_0 = 2\frac{e^{-\frac{1}{2}(\gamma_S-\gamma_L)t}\cos\Delta mt}{1+e^{-(\gamma_S-\gamma_L)t}} \tag{1.5}$$

this is shown in the inset of figure 1.3. There are two points to notice. Since $\cos\theta$ is a symmetric function, the sign of the mass difference cannot be deduced from these transition rates. Secondly there is no phase factor in the cosine term, so the error on the mass difference determined in this way is not directly correlated with the error of any CP violating parameter.

It is convenient to measure time in units of the lifetime of the short lived eigenstate. To make the conversion from nanoseconds I use $\gamma_S = 1.121\times10^{10}\text{s}^{-1}$ [4]. The argument of the cosine in equation 1.5 then becomes

$$(\Delta m/\gamma_S)(\gamma_S t) = (\Delta m/\gamma_S)(t/\tau_S)$$

which is one reason why I work with the ratio $\Delta m/\gamma_S$, as opposed to just the mass difference.

1.3 Author's contribution

The first three chapters of this thesis provide background material for the main part: chapters four through seven. The work in the last four chapters is basically all my own. I developed the criteria presented in chapter four from scratch. The event selection presented in chapter five is also my work as is the analysis presented in chapter six. The asymmetry from which I determine the mass difference was suggested by me on the basis of its insensitivity to the normalisations needed. The method of determination of these normalisations; the form of the correction to the asymmetry due to background and the integral fit used were devised by me. Finally I would like to claim sole responsibility for any mistakes in this work.

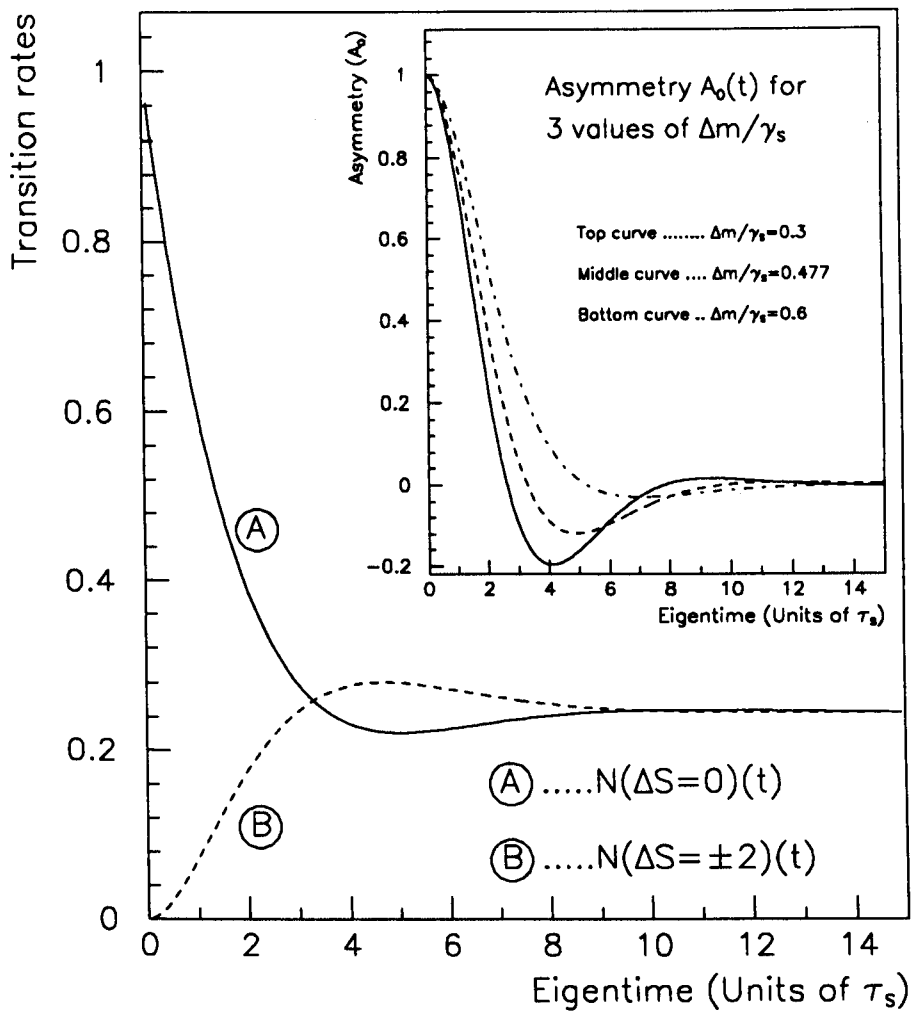

Figure 1.3: The rates $N(\Delta S = 0)$ and $N(\Delta S = \pm 2)$, calculated with a mass difference of $\Delta m/\gamma_S = 0.477$. The inset plot shows the asymmetry, $A_0(t)$, for three values of the mass difference.

Blank Page

Chapter 2

The CPLEAR detector

2.1 Introduction

The CPLEAR detector is a magnetic spectrometer, capable of the full reconstruction of events from proton-antiproton annihilations at rest. It is composed of a number of cylindrical subdetectors arranged concentrically within a solenoidal magnet which provides a constant axial magnetic field of 0.438 Tesla. The axis of the detector defines the Z axis of a Cartesian coordinate system, with $Z = 0$ at the centre of the target. The transverse (XY or $R\phi$) plane is orthogonal to the axis, with the origin again at the centre of the target. Figure 2.1 shows a transverse schematic of the detector through $Z = 0$ and figure 2.2 shows a cut-away view.

From the centre of the detector outwards, the subdetectors are:

- Beam Counter (BC) and target
- Tracking chambers, consisting of
  - Multiwire Proportional Chambers (PCs)
  - Drift Chambers (DCs)
  - Streamer Tubes (STs)
- Particle Identification subDetector (PID), consisting of
  - Inner Scintillator (S1)

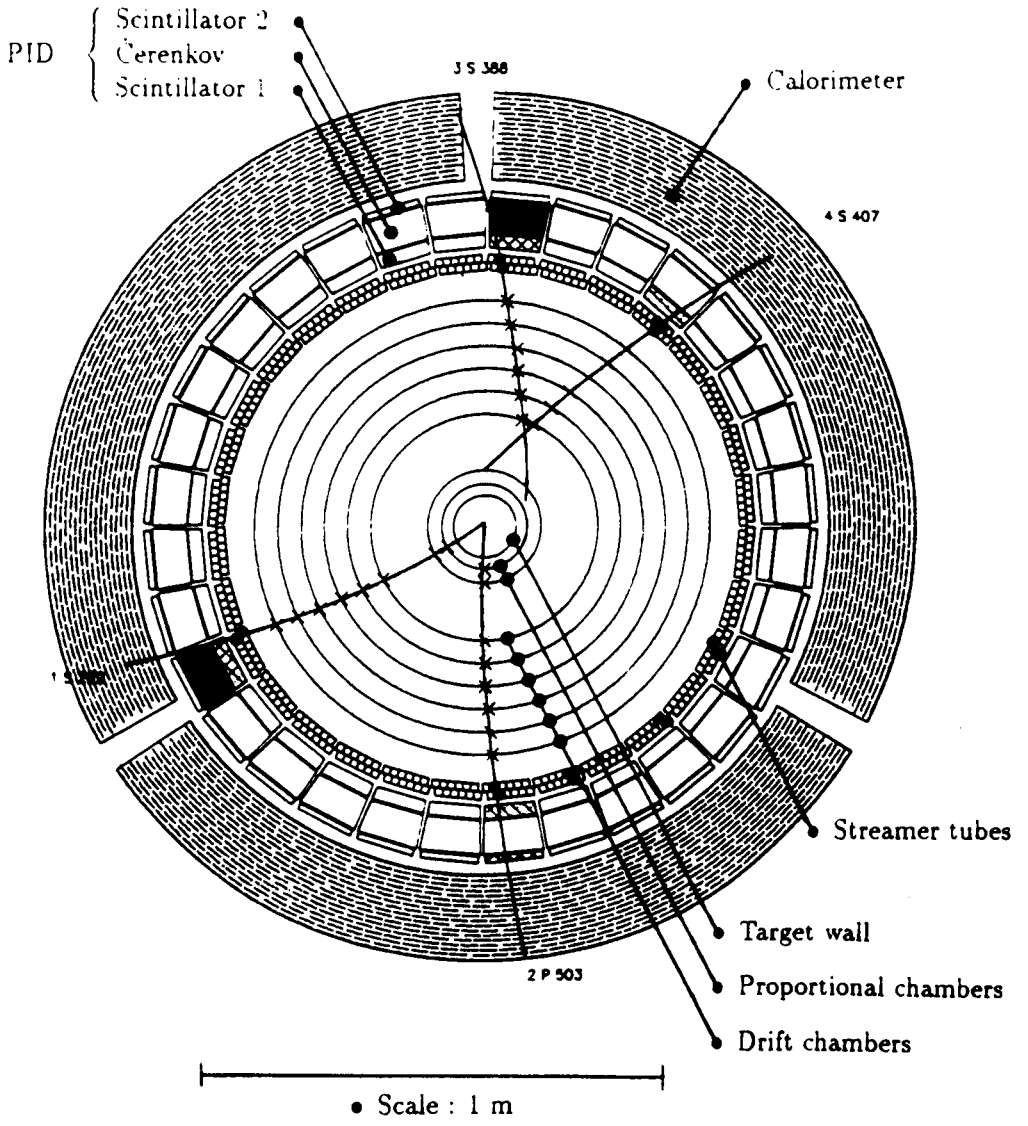

Figure 2.1: A transverse sectional view of the CPLEAR detector. The figure shows a $p\bar{p} \rightarrow K^-\pi^+K^0$ annihilation with the neutral kaon decaying just inside the first drift chamber, giving two charged secondary tracks.The track originating from the centre of the target and descending vertically is identified as a kaon as it has a momentum of 500 MeV/c and gives an $S\overline{C}S$ signal in the PID — see text following.

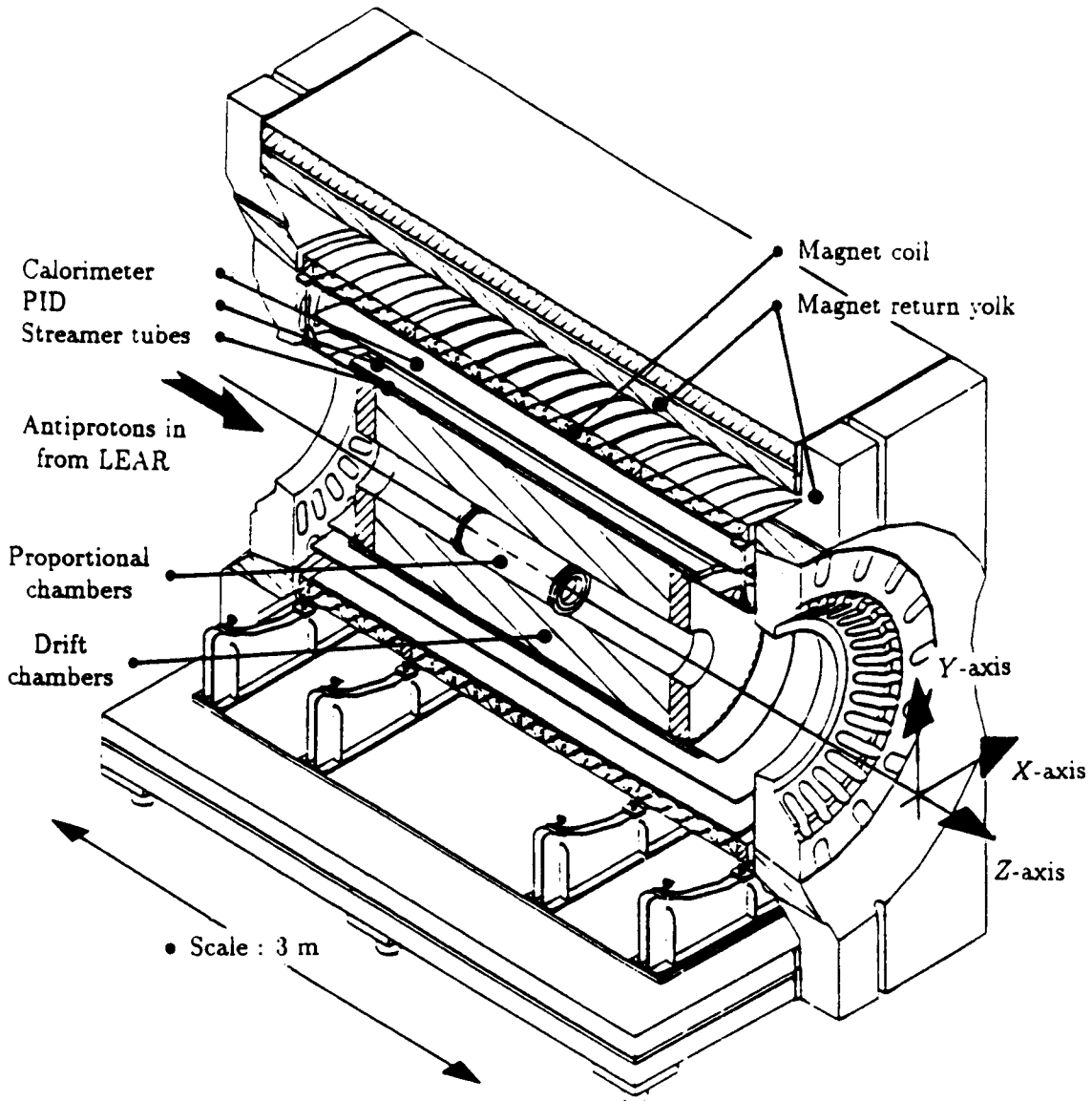

Figure 2.2: A cut-away longitudinal (RZ) view of the CPLEAR detector through $x = 0$.

  - Threshold Čerenkov (C)
  - Outer Scintillator (S2)

- Calorimeter

Each of the subdetectors is described in the following section.

The detector is designed to study events of the type

$$p\bar{p} \longrightarrow \begin{cases} K^-\pi^+K^0 \\ K^+\pi^-\bar{K}^0 \end{cases}$$

where the neutral kaon decays somewhere within the tracking chambers

$$K^0(\bar{K}^0) \longrightarrow X^+X^-X^0$$

This type of event is termed **golden.**

The point at which the proton-antiproton annihilation takes place is termed the **primary** or **annihilation vertex.** Tracks originating from this vertex are thus **primary tracks.** Tracks originating from the point of the neutral kaon decay (the **secondary** or **decay vertex**) are termed **secondary tracks**[†].

Full reconstruction of an event implies three things

- Tagging of the neutral kaon's initial strangeness.
- Identification of the final state.
- Determination of the time between the $p\bar{p}$ annihilation and the neutral kaon decay as measured in its rest frame, termed the **eigentime** or **decay time.**

The initial strangeness of the neutral kaon is determined from the charge of the primary charged kaon, while the decay mode can be determined from a combination

[†] *Primary* and *secondary* are used in an alternate sense from a triggering point of view: primary referring to tracks which start from within the second proportional chamber and secondary referring to all others. The context should make it clear which sense is implied.

of kinematics and particle identification. Using the position of the primary and secondary vertices ($\boldsymbol{x}_1$ and $\boldsymbol{x}_2$) and the transverse momentum of the neutral kaon ($\boldsymbol{p}_T$) the eigentime can be determined from

$$t = \frac{m_{K^0} |\boldsymbol{\Delta}_T|}{|\boldsymbol{p}_T| c} \tag{2.1}$$

where $\boldsymbol{\Delta}_T$ is the transverse component of $\boldsymbol{\Delta} \equiv \boldsymbol{x}_2 - \boldsymbol{x}_1$ and c is the speed of light.

Since in CPLEAR we are predominantly interested in the intrinsic matter-antimatter asymmetries of neutral kaons in vacuum it is essential to avoid any differences due to the nature of the particles' environment, i.e. the presence of the detector. Unfortunately since the detector is necessarily built of matter it is impossible to remove these effects altogether, for although the strong interactions are charge-conjugate symmetric the K^0-matter and $\bar{K}^0$-matter reactions are not related by a charge-conjugation transformation and hence have different cross sections.

The best that can be achieved is to minimise these differences as much as possible and to this end the detector has been built with as little matter in the central volume as possible. The amount of material present is characterized by the interaction length, X_0, defined as the mean distance travelled by a particle before it undergoes an inelastic nuclear interaction. It is given by

$$X_0 = \frac{1}{\sigma_{Inel}} \left(\frac{A}{N_A \rho} \right)$$

where N_A is Avogadro's number, A is the effective atomic mass of the material, ρ is its density, and σ_{Inel} is the inelastic cross section for neutral kaon-neucleon interactions.

2.2 The subdetectors

2.2.1 Beam counter and target

Antiprotons are supplied by LEAR with a momentum of 200 MeV/c. The stochastic cooling of the beam ensures that 98 % of the antiprotons have a momentum within ± 0.2 MeV/c of this value. The small spread in energy of the beam is needed to minimise the straggle in the antiproton stopping distribution. The transverse position of the beam is monitored by two multiwire chambers in the beam pipe just upstream

of the detector. The position of the beam can be adjusted so as to ensure a clean entrance into the target.

Before the antiprotons enter the target, they are slowed down by passage through a thin (approximately 2 mm thick) piece of beryllium. The beryllium may be tilted so as to adjust the thickness of material passed through by the beam and thus the amount of energy lost by the antiprotons.

The beam enters the target through a mylar window 0.12 mm thick and 11 mm in diameter. The entrance of an antiproton into the target is detected by the beam counter, a thin scintillator just in front of the entrance window. The signal from the beam counter starts the trigger sequence.

The target is a 14 cm diameter kevlar ball filled with hydrogen gas at 15 atmospheres pressure. To reduce the amount of matter close to the interaction point it has extremely thin (0.4 mm) walls. The gas and the kevlar wall together correspond to a total of 9×10^{-4} interaction lengths.

On entering the target the antiprotons have been slowed sufficiently to allow the formation of bound states with the proton nuclei of the hydrogen gas. Annihilation then occurs with a total energy just less than two proton masses available to the final state particles. The longitudinal straggle in the annihilation vertex is of the order of 5 cm, and its centroid can be positioned in the centre of the target by altering the thickness of beryllium that the beam passes through.

Details of the target and beam counter can be found in reference [13].

2.2.2 Tracking chambers

In the CPLEAR detector there are ten layers of tracking chambers provided by three tracking subdetectors. From the centre outwards, these are

- Two multiwire proportional chambers: PC1 (innermost) and PC2.
- Six drift chambers: DC1 (innermost) to DC6 (outermost)
- Two layers of streamer tubes: ST1 (innermost) and ST2.

Chamber	Radius [cm]	Number of Wires
PC1	9.5	576
PC2	12.7	768
DC1	25.5	2 x 160
DC2	30.6	2 x 192
DC3	35.7	2 x 224
DC4	40.7	2 x 256
DC5	45.8	2 x 288
DC6	50.9	2 x 320
ST1	58.0	192
ST2	60.0	192

The tracking chambers serve two purposes: they provide a series of space points from which charged particle trajectories can be reconstructed, and additionally all three of the subdetectors provide information for the trigger as described in section 2.3. The tracking subdetectors are described briefly below.

Proportional chambers

Each chamber consists of a layer of wires and two layers of stereoscopically aligned strips. The wires run parallel to the axis of the detector and are spaced 1mm apart. Since ionized charge may be collected on more than one wire, transverse points can be measured with a resolution of less than half a millimetre. To date the proportional chamber strips have not been instrumented for readout, and consequently provide no Z information.

Specifications

Gas mixture	Argon 79.5 %/Isobutane 20 %/ Freon 0.5 %
Operating voltage	2500 V
$R\phi$ resolution	350 μm
Efficiency per layer	97% (wires)

Both proportional chambers together are equivalent to 2.3×10^{-3} interaction lengths.

Drift chambers

As per the proportional chambers, each drift chamber has longitudinal wires and two layers of stereoscopic strips.

The sense wires are arranged in doublets alternating with HV wires. The wires in the doublet are one millimetre apart and each doublet is spaced 1 cm from the next. This arrangement solves the problem of left-right ambiguity but at the expense of a reduction in efficiency and resolution in the region between wires of the same doublet.

Of the six chambers DC1, DC2, DC4 and DC6 have instrumented strip readout, providing Z measurements. This arrangement means that all secondary tracks, which must begin inside DC4 in order to have at least three transverse points, can have at least two longitudinal measurements also.

Specifications

Gas mixture	Ethane 50 %/Argon 50 %
Operating voltage	2300 V
$R\phi$ resolution	250 μm
Z resolution	3 mm(before P10)/1 mm(since)
Efficiency per layer	97% (wires), 95% (strips)

To minimise the amount of material inside the detector, the drift chamber walls have been constructed of extremely light material and a slight gas over-pressure is used to maintain their shape. Each drift chamber (wires, strips, support skin and gas) corresponds to 7×10^{-4} interaction lengths.

For further details of the drift chambers see reference [14].

Streamer tubes

Each layer of streamer tubes consists of 192 1.65 x 1.65 cm^2 aluminium tubes, each with a central wire. The wires are held at a positive voltage to collect the electrons resulting from ionization. Current pulses travel to either end of a wire where they are fed into a TDC. The connections are arranged such that the pulse travelling to the downstream end of the detector always arrives before that traveling upstream. The downstream signal is thus used as a start signal, while the upstream one is used as a stop. The time difference between the stop and start signals is then translated into a Z coordinate. Since the drift time is not measured in the streamer tubes the transverse resolution is given by the half-size of the tubes, i.e. $\sim$ 8 mm.

The purpose of the streamer tubes is to provide fast online Z measurements which are used to calculate the kinematics of an event online.

Specifications	
Gas mixture	Argon 50 %/Isobutane 46 %/ methylal 4 %/Freon 0.008 %
Operating voltage	4200 V
$R\phi$ resolution	8 mm
Z resolution	1.4 cm
Efficiency	86 % (Per layer) 98 % (Combined)

2.2.3 Particle identification subdetector

The Particle Identification subDetector (PID) is constructed from 32 identical sectors, one of which is shown in figure 2.3. Each sector consists of two three metre long plastic

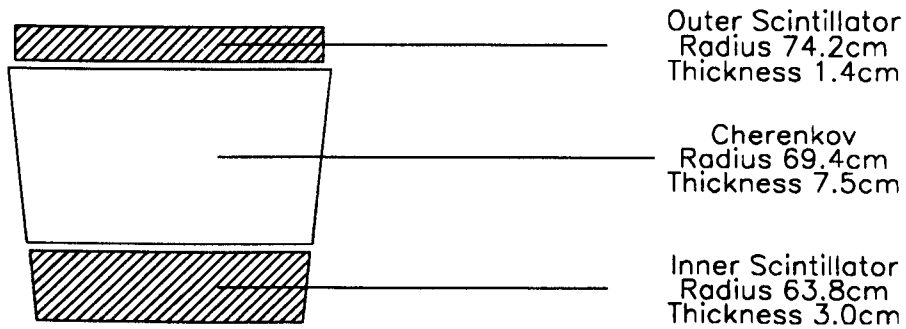

Figure 2.3: A PID sector. The radii refer to the centre of the elements. Both scintillators and the Čerenkov are 3.1 m long.

scintillators sandwiching a threshold Čerenkov element. Light emitted as particles pass through is transmitted along the length of the PID elements by total internal reflection. To collect the light, each scintillator has a photomultiplier tube (PM) attached at each end, while the Čerenkovs have two PMs at either end.

The Čerenkov elements consist of extruded plastic tubes filled with a liquid radiator, FC72 (C_6F_{14}), containing 20 mg/l diphenyl-oxazole (PPO). The refractive index of FC72 is 1.27 giving a threshold velocity of 0.8c. The PPO acts as a wavelength shifter, absorbing Čerenkov light between 270 nm and 320 nm and re-emitting it in

the region 300 – 450 nm where the photomultipliers are more efficient. The light is re-emitted isotropically, making light collection efficiency more even along the length of the tube. To aid further in this the central 80 cm of the outer wall are painted with white reflective paint to specularly reflect light that would otherwise be transmitted through the tube wall and lost.

The main purpose of the PID is to provide fast online kaon identification and a first estimate of charged track multiplicity for the early stages of the trigger. The signature for a kaon consists of light in both S1 and S2, indicating the passage of a particle through the Čerenkov, with no light in the Čerenkov itself, a so called $S\overline{C}S$ signal. The Čerenkov velocity threshold corresponds to a momentum threshold of $\sim$ 700 MeV/c for kaons and $\sim$ 180 MeV/c for pions. Thus the absence of a signal in the Čerenkov indicates either a kaon or a slow pion. The charged track multiplicity is given by the number of inner scintillators hit, N_{S1}.

Later in the trigger and offline the PID provides more general particle identification information: the scintillator signal pulse height provides a measure of ionization energy loss, dE/dx; and Time Of Flight (TOF) is measured by TDCs which take the Beam Counter signal as starts and S1 signals as stops.

See reference [15] for full details.

2.2.4 Calorimeter

The subdetector furthest from the target is a high granularity gas sampling calorimeter. It is built from layers of 4×4.5 mm^2 streamer tubes with planes of strips angled at thirty degrees to the wires on either side of the tubes. In between these layers are 1.5 mm thick lead converter plates.

Due to the restricted amount of space available for the calorimeter inside the solenoid (22 cm) it consists of only eighteen layers, giving 5.8 radiation lengths in total.

The strength of the calorimeter lies in the high spatial resolution with which the initial photon conversion point can be located. From Monte Carlo studies it was found that high spatial resolution is more important than energy resolution for the

reconstruction of the neutral kaon decay vertex in neutral decay modes.

Details of the calorimeter design and operation are presented in references [16] and [17].

Specifications	
Gas mixture	Carbon dioxide 55 %/Pentane 45 %
Operating voltage	3200 V
Spatial resolution	5 mm
Energy resolution	$\frac{\sigma(E)}{E} \sim \frac{15\%}{\sqrt{E(\mathrm{GeV})}}$
Efficiency	$\sim 95\%$ (for γs with $E > 75$ MeV)

The calorimeter was not operational when the work in this thesis was done and hence is used nowhere in the analysis. However an algorithm now exists to separate electron and pion tracks with momenta greater than 200 MeV/c.

2.3 Trigger

The branching ratio for $p\bar{p} \rightarrow \pi^+ K^- K^0$ and $\pi^- K^+ \bar{K}^0$ is 4×10^{-3}. The CPLEAR experiment is aiming to reconstruct 10^{10} golden events, and the main purpose of the trigger is to minimise the number of non-golden events that are written to tape. The CPLEAR trigger is, however, highly modular and can be programmed for different data taking requirements, e.g. cosmics and minimum bias data. I describe here only those aspects of the trigger which were operational during the periods in which the data in this thesis were taken.

The trigger sequence is started when an incoming antiproton gives a signal in the beam counter. This signal also starts the TDCs of the PCs, DCs and PID S1s. To avoid overlapping, the event is aborted if a second antiproton passes through the beam counter within 200 ns of the first.

The first stage of the trigger is the **Early Decision Logic** (EDL). Its sole inputs are the PID hitmaps. From these it makes a decision based on the number of sectors with hits in the inner scintillator (N_{S1} — track multiplicity) and the number of sectors with an $S\overline{C}S$ signature ($N_{S\overline{C}S}$ — kaon multiplicity). The two main programs are:

EDL 1 $N_{S1} > 0$

EDL 3 $(N_{S1} \geq 2)\text{AND}(N_{S\overline{C}S} \geq 1)$

EDL 1 is for the collection of minimum bias data while for the collection of golden events EDL 3 is used.

Two types of event may pass EDL 3: true kaonic events, and events where the $S\overline{C}S$ signal is due to a slow pion. A pion with a velocity less than the Čerenkov threshold gives no light and thus mimics a kaon. The next trigger stage is the **P_T cut processor** and its purpose is to reject the slow pion $S\overline{C}S$ events.

The processor uses the difference in hit wire numbers between DC1 and DC6. The track which caused these hits is assumed to have come from the origin, so this wire difference gives an estimate of the sagitta of the track and hence its transverse momentum. Note that at this early stage of the trigger no tracks have been reconstructed; everything is done on the basis of coincidences in zones centred on the PID sectors.

A sector in which the P_T measured is greater than a preprogrammed value, and in addition has an $S\overline{C}S$ signal in the PID is termed a kaon candidate. The P_T processor passes events which have at least one kaon candidate. Preprogrammed P_T values used are:

P_T **0** Passive: No minimum P_T (for minimum bias data)

P_T **2** Minimum P_T = 270 MeV/c

P_T **3** Minimum P_T = 400 MeV/c

The next stage of the trigger is the **Intermediate Decision Logic** (IDL). The IDL performs three tasks:

- Validation of a kaon candidate as primary.
- Counting of primary tracks.
- Counting of all tracks.

A **track** is defined to be a hit in S1 with an associated hit in DC5 or DC6. In addition if there are hits in DC1 or DC2 and hits in PC1 or PC2 within zones centred on the S1 sector then the track is a **primary track**.

Since the kaon candidate has passed the P_T cut it has hits in DC1 and DC6. To remain a kaon candidate there must also be a corresponding hit in either PC1 or PC2. The number of kaon candidates is N_K, the number of tracks is N_T and the number of primary tracks is N_P. The IDL passes events which satisfy preprogrammed criteria. The possible configurations are:

IDL 1 All events pass (minimum bias)

IDL 2 $N_T = 2$ or 4; $N_P = 2,3$ or 4; $N_K \geq 1$

IDL 3 $N_T = 4$; $N_P = 2$; $N_K \geq 1$

IDL 4 $N_T \geq 4$; $N_P = 2$; $N_K \geq 1$

During the time when the data in this thesis was collected, this was the extent of the active part of the trigger. Later more complex trigger processes were run only passively for testing. All events passing the IDL were written to tape.

The timings for the early trigger stages are shown below. Also shown are the reduction factors in the frequency that events pass each trigger stage. The reduction actors depend on the trigger configuration; these figures are for IDL 4, P_T 3 and EDL 3.

Trigger processor	Reduction factor	Decision time
EDL	5.4	60 ns
P_T cut	6.3	400 ns
IDL	1.9	800 ns

The time to readout an event and reset the trigger is 4 ms.

The trigger type denotes how the trigger has been programmed and is denoted by:

- (IDL code)(P_T code)(EDL code)

The main data taking trigger types are then 433 and 233, i.e. EDL 3, $P_T(min) = 400$ and either IDL 4 or 2. Later data, after P10, was taken with a reduced P_T cut, i.e. trigger types 423 and 223.

Throughout this thesis the following notation is used to denote the running period, magnetic field orientation and trigger type:

Pn	Running period n
Mn	Magnetic field orientation
	n=1—Normal,$B_Z > 0$
	n=2—Reverse,$B_Z < 0$
Txxx	Trigger configuration

For example P8M1T433 means: Running period 8; Normal magnetic field orientation; and trigger configuration 433.

2.3.1 Future of the trigger and DAQ

The philosophy of the CPLEAR trigger is to reconstruct events online. The early stages, described above, are extremely fast and hence fairly crude in order to avoid deadtime. The later stages of the trigger will be set in motion much less frequently and can therefore be correspondingly more complex. The later stages of the trigger are outlined below.

At all stages of the trigger up to and including the IDL decision, no tracks are reconstructed; a "track" is actually a set of hit wire groups (not single wire hits) within some predefined zone azimuthally centred on an S1 sector. In order to make the later, more elaborate, trigger decisions it is necessary to reconstruct tracks online. Wire hits in the DCs and PCs are grouped into tracks by online pattern recognition processors. The digitized information from the tracking chambers is used (1 mm accuracy on the space points is possible using look-up tables) and track parameters, such as transverse momentum, are calculated.

The streamer tubes provide a Z measurement of tracks with 1.4 cm resolution, and for primary tracks this is used to calculate the dip angle and hence the longitudinal momentum assuming that the track comes from the origin.

The kaon track can be paired with one or two oppositely charged primaries (depending on the number present) and the primary missing mass calculated. This can be compared with the mass of the neutral kaon and a decision made. The invariant mass of the secondaries can also be calculated online and this may be used to reject $\pi^+\pi^-$ decays at small eigentimes.

The digitized PID information is used to put tighter constraints on the kaon candidate track and also on the primary track with which is paired in order to reduce the

background from K^+K^- annihilations which are a problem at small eigentime. Pulse height information from the Čerenkov and dE/dx from S1 are used for this, as well as measurement of the time-of-flight difference between the kaon candidate and the other primary track.

Neutral decay modes give showers in the calorimeter which can be counted and used to either select or reject events.

The full trigger will be a very powerful programmable system but even so there is still a problem with the sheer number of decays that the experiment needs to reconstruct. Most of these decays are two pion decays within a few τ_S and are of no interest for measuring time dependent asymmetries. These events are used only for the measurement of ϵ'/ϵ by the time integrated asymmetries. The current plan is to write out only a fraction of these two pion decays, 1% say, and send the rest through an alternative data stream.

Chapter 3

Data processing

3.1 Introduction

The purpose of offline processing is to take raw data and perform the first stages of event reconstruction, i.e. to group chamber hits into tracks, to fit the tracks and determine momenta. Each of these tasks is performed by an offline software processor, specifically written for the CPLEAR experiment. The processors are outlined very briefly in the next section.

Since event reconstruction is CPU intensive, it is inefficient to reconstruct events more than once. However, CPLEAR is a high statistics experiment and the storage of all fully reconstructed events is undesirable if not impossible. Therefore during the processing stage, the events are passed through a number of software filters. These are designed to identify and discard those events least likely to be useful in later analyses. The filters are described in section 3.3.

The processing is done in two stages. Raw events are passed through the DECODING, TRANSLATION, and PATTERN RECOGNITION processors, and then through the first level filters: FILTER 6 and FILTER 7. Those events which pass the filters are passed onto the TRACK FIT and VERTEX RECONSTRUCTION processors, and then the second level filters: FILTER 10, KAON4T and KAON2T.

For those events which pass the second level filters there are two output streams:

- Data Summary Tapes (DSTs) — these contain all the event information, i.e. all

of the raw information as well as the output from the processors

- MiniDSTs — these contain only a subset of this information. The miniDSTs contain only that information which can be associated with a particular reconstructed track. Thus any tracking chamber hits or PID information not linked to a specific track is lost. In addition miniDSTs contain mainly processed output.

miniDSTs are most convenient for large scale analysis as one IBM cassette can contain around 10^5 events. (The inclusion of calorimeter information approximately halves this.)

3.2 Offline processors

Below is a brief description of the offline processors in the order in which they are applied to events.

DECODING and TRANSLATION

These convert digital raw data into more physically meaningful quantities such as spatial positions, time differences, photomultiplier pulse heights, etc.. Calibration and alignment is done for each running period individually to allow for any shifts or drifts.

PATTERN RECOGNITION

The aim of this processor is to group together tracking chamber space points to form tracks. Tracks are searched for first in the transverse plane. Once a track is found in the $R\phi$ plane, hits in the longitudinal plane, if any, are matched with those in the transverse to construct helices. It is possible to find tracks in the transverse plane only.

TRACK FITTING

The purpose of the track fit is to define the track parameters, i.e. momentum vectors and spatial position, more accurately, allowing for multiple scattering. Fitting is done

separately in the transverse and longitudinal planes, as it is too CPU intensive to do full three dimensional space fits.

VERTEX RECONSTRUCTION

A simple geometrical algorithm searches pairwise for intersections in the transverse projections of tracks. If two tracks have a double intersection the point where the tracks are closest in Z is defined as the vertex point. The processor provides all possible vertices since a given track can intersect more than one other track. The determination of which are true vertices must be done later.

3.3 Software filters

Since data taken with IDL 2 and IDL 4 trigger configurations are different, there are different filters for each. Data taken with IDL 4 trigger configurations should all have the basic two primary track, two secondary track topology. These events are passed through FILTER 6 and then FILTER 10. Events taken with IDL 2 triggers can have either two or four track topologies. All this data is passed through FILTER 7 but then four track events are passed through the KAON4T filter, while two tracks events are passed through KAON2T. Events passing the second stage filters are written to the DSTs and the miniDSTs. This is summarised in figure 3.1. Monte Carlo data are first passed through a software trigger simulation so as to mimic as nearly as possible the real data.

Recall that a track is a primary track if it has at least one hit in the PCs otherwise it is a secondary track. For the first stage filters (6 and 7) a kaon candidate is defined as a primary track which has:

1. S1 and S2 hits in the same PID sector and no Čerenkov hit.

2. A momentum of at least 300 MeV/c.

Two primary tracks form a good primary vertex if they intersect in the transverse plane at a point for which:

1. The radial position is within 2 cm of the axis of the detector.

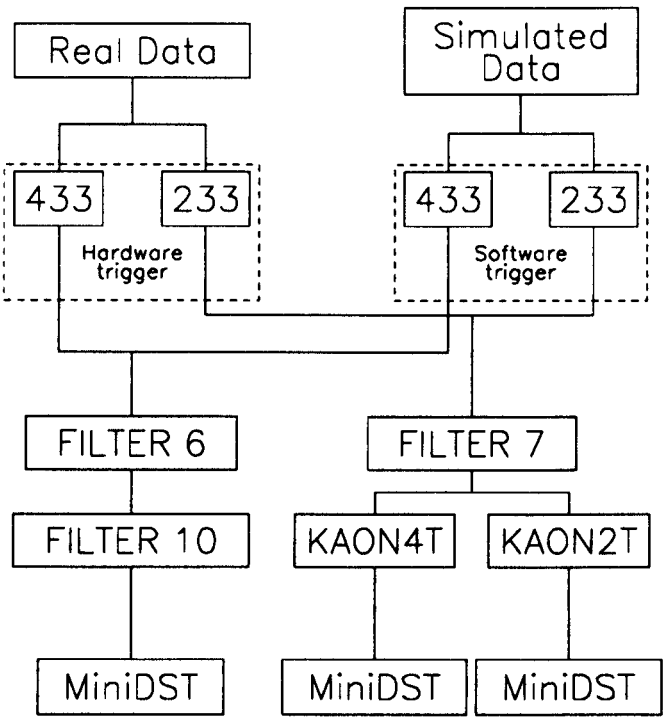

Figure 3.1: Data path for real and simulated data. IDL 4 data is represented by 433 and IDL 2 data by 233, the most common early trigger types.

2. The longitudinal (Z) position is within 10 cm of the centre of the target.

3. The distance from each track to the vertex is less than 10 cm.

Filter 6

To pass filter 6 the event must satisfy the following criteria:

- There must be exactly two primary and two secondary tracks found by the PATTERN RECOGNITION.

- The two primary tracks must have opposite charge.

Filter 7

To pass filter 7 the event must satisfy the following:

- The PATTERN RECOGNITION finds two or four tracks.
- There must be at least two primary tracks.
- The sum of the charges of the tracks is zero. If there are two primaries then their total charge must sum to zero.
- All primary tracks have at least five transverse hits.
- All tracks must have at least one longitudinal hit and p_Z must not be exactly zero.
- At least one of the primaries must be a kaon candidate.

Filter 10

This is the second stage trigger for 433 data. To pass, an event must satisfy the following:

- There must be a minimum amount of drift chamber strip (Z) information. For each track
  1. there must be at least one Z point in DC6 or in one of the streamer tubes.
  2. $|P_Z|$ must not be exactly zero.
- Either one or both of the primary tracks must be a Kaon candidate and in addition it must have a value of dE/dx in S1 which is compatible with a kaon track
- All tracks must be fitted by the TRACK FIT processor.
- The primary tracks must form a good vertex as defined above.
- The secondary tracks must form a vertex and have an opening angle whose cosine is greater than -0.98. This is to avoid backscatters and cosmics.

After the first stage filter 233 events can have two or four tracks. The second stage filtering therefore consists of two separate filters, KAON2T for two track events and KAON4T for four track events.

Filter KAON2T

To pass this filter the event must satisfy the following:

- There must be exactly two tracks
- The kaon candidate track must have a value of dE/dx in S1 which is compatible with a kaon track
- The TRACK FIT must fit all the tracks found by the PATTERN RECOGNITION.
- There must be a good primary vertex as defined above.

Filter KAON4T

This is exactly as per the KAON2T filter, except the event must have four tracks and in addition: but in addition:

- The two tracks which do not form the primary vertex must intercept in the transverse plane. Note one or both of these may be primary tracks.

Chapter 4

Electron selection

4.1 Introduction

This chapter details the selection criteria developed to separate electron tracks from pion tracks[†]. using information from the PID. This information consists of dE/dx measurements from the scintillators and measurements of the number of photoelectrons in the Čerenkov elements. The aim is to select electron tracks with as high an efficiency as possible, while keeping the probability to wrongly identify a pion as an electron low. I have taken (fairly arbitrarily) one percent as an acceptable pion contamination level.

The calorimeter is also used to separate the two types of particle, but only in the momentum region above 200 MeV/c. The work described here applies to the momentum region below 250 MeV/c, providing an increased momentum range for electron identification and an increased efficiency for the selection of semileptonic decays. Figure 4.1 shows the momentum spectrum of electrons from the process $p\bar{p} \rightarrow K^{\pm}\pi^{\mp}K^0$ followed by $K^0 \rightarrow e^{\pm}\pi^{\mp}\nu$, i.e. semileptonic golden events. It shows clearly the importance of the low momentum region.

As described in chapter 5, clean samples of pions and electrons are available in IDL 3 data sets; pions from the primary vertex and electrons from gamma conversions.

[†]Unless explicitly stated otherwise, for *electron* read *electron and positron* and for *pion* read *positively and negatively charged pions.*

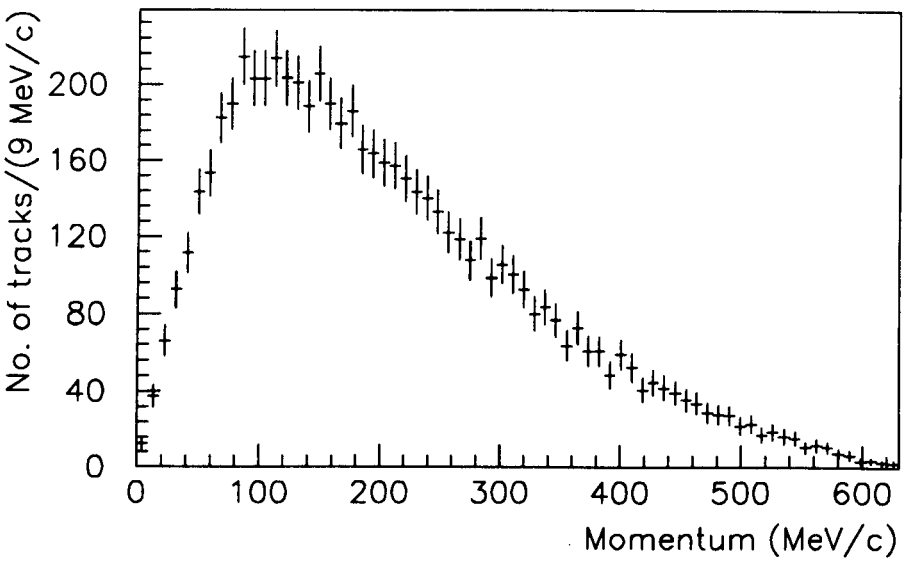

Figure 4.1: The electron momentum spectrum from semileptonic golden events. Approximately one third of the tracks have a momentum below 180 MeV/c.

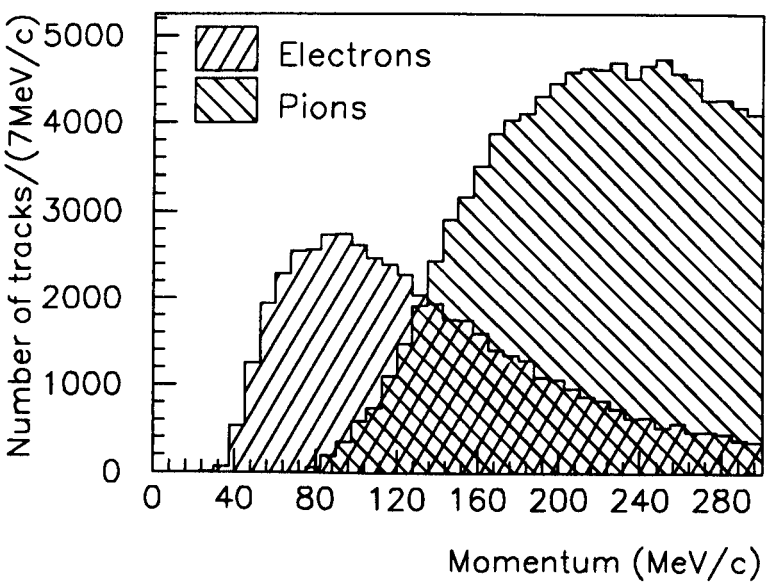

Figure 4.2: The momentum spectra of the pion and electron track samples peak in different regions but overlap over most of the important region.

Thus I have taken an almost purely empirical approach to developing the selection criteria. The differences in the PID signals of pions and electrons are outlined in section 4.3 and section 4.4 details how these differences are exploited to give a set of selection criteria. The results, i.e electron selection efficiency and pion contamination probability, are presented in section 4.5.

One drawback to this empirical approach arises because of a difference in the momentum spectra of the pion and electron samples (shown in figure 4.2). This necessitates some extrapolation of the results as there are very few primary pions with momenta below 100 MeV/c (70 MeV/c is the lowest momentum possible for a primary track to reach S1) and most of the electrons have momenta less than 200 MeV/c. The main assumption in this work is that the background of pions selected as electrons in the momentum region below 100 MeV/c does not increase markedly above what it is between 100 MeV/c and 250 MeV/c, i.e. ~ 1 %.

4.2 Čerenkov Z correction

In order to relate the amount of light detected by the photomultipliers to the amount of light actually emitted by a particle during its passage through the Čerenkov it is necessary to correct for the attenuation of the light between its emission and its incidence on the PMs; this is dependent on the Z coordinate at which the particle's trajectory passes through the Čerenkov.

Consider a particle which passes through the Čerenkov at a point Z along its length. It emits a total amount of light Λ_0 which is internally reflected to both ends of the Čerenkov where it enters the PMs, of which there are two at either end. The amount of light incident on the i^{th} PM is Λ_i and this causes the ejection of $n_i = \alpha\Lambda_i$ photoelectrons[†]. Ignoring the directional nature of Čerenkov radiation, the amounts of light incident on the PMs at the upstream (u) and downstream (d) ends of the

[†]The factor α is simply a conversion factor between an amount of light and a number (of photoelectrons). It is the same for all particles and all Čerenkov elements — the relative yields of different PMs have already been corrected for in n_i.

Čerenkov are given by

$$\Lambda_u = \Lambda_1 + \Lambda_3 = \frac{1}{2}\Lambda_0 e^{-(Z_u - Z)/\lambda}$$
$$\Lambda_d = \Lambda_2 + \Lambda_4 = \frac{1}{2}\Lambda_0 e^{-(Z - Z_d)/\lambda}$$

where λ is the characteristic attenuation length in the Čerenkov and $Z_u = -Z_d = 155$ cm are the Z coordinates of the PM photocathodes. I have verified with a ray-tracing simulation that if losses are due only to transmission of light through the Čerenkov wall then the functional form of the intensity attenuation is very close to exponential.

The total number of photoelectrons measured is $N = \sum_{i=1}^{4} n_i$ and is given by

$$N = \frac{1}{2}\alpha\Lambda_0 \left(e^{-(Z_u - Z)/\lambda} + e^{-(Z - Z_d)/\lambda}\right)$$

which can be rearranged to give

$$N = \alpha e^{-(Z_u - Z_d)/2\lambda}\Lambda_0 \cosh(Z/\lambda)$$

If there was no light attenuation then the total number of photoelectrons ejected would be $N_0 = \alpha\Lambda_0$. Since α is the same for electrons and pions N_0 gives a measure of the amount of Čerenkov radiation emitted by the particle. To correct for attenuation then I simply replace N by

$$\frac{N}{\cosh(Z/\lambda)}$$

and use this quantity as a measure of the light emitted by a particle on its passage through the Čerenkov.

In the rest of this thesis whenever I refer to the number of photoelectrons it is to this corrected quantity that I am referring. I denote the number of photoelectrons per unit path length by dN/dx and determine it from N/L where L is the path length traversed by the particle in the Čerenkov.

The value of λ is determined from the measured raw total number of photoelectrons as a function of Z. A hyperbolic cosine curve is then fitted to this and λ determined. Figure 4.3 is an example of one such fit. Similar fits have been done for each PID sector but to within the accuracy of the fit the variation of λ from sector to sector is not important. All of the tracks used for the determination of λ are tracks from

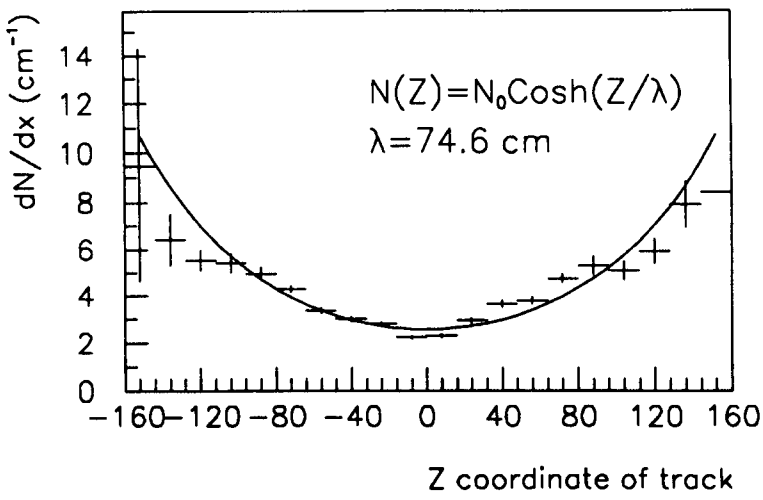

Figure 4.3: Determination of the attenuation length parameter in the Čerenkov subdetector. The fit is a two parameter fit; one parameter for the attenuation length (λ) and the other for the (arbitrary) signal size at $Z = 0$ (N_0).

the electron sample (thus all with $\beta = 1$) with hits in S1 and S2 in the same sector. This ensures that the path length through the Čerenkov and hence dN/dx is correctly determined. The discrepancy between the data points and the fitted function is typical of all the Čerenkov sectors — see below.

The above correction is necessarily an approximation. The Čerenkov radiation is not emitted isotropically but in a cone with apex angle $\cos\theta = 1/\beta n$. This means that a full correction for attenuation must take into account not only the Z-coordinate of the track where it passes through the Čerenkov, but also the angle of the track to the Z-axis — the incidence angle. A full correction will be more complex than just the simple $\cosh(Z/\lambda)$ dependence, thus giving the discrepancy between the data and the fit in figure 4.3.

The track samples used to develop the electron selection criteria all point towards the centre of the target in the longitudinal projection: pions because they are primary tracks, and electrons because the photons from which they originate come from π^0 decays at the origin. For all of these tracks the angle of incidence and the Z coordinate

are correlated.

This is a problem because electrons from real semileptonic decays are not subject to this correlation. For these tracks the correction will be in error. In section 4.5 numbers for the electron selection efficiency and pion contamination probability are presented. Since these are determined from track samples with Z and the incidence angle correlated, they will differ from the values for real secondary tracks. The size of the difference is difficult to estimate, but I do not expect it to be large for two reasons. Most of the secondary tracks pass through the central 100 cm of the Čerenkov just from solid angle considerations. This is where the difference is least. Secondly, the results of chapters 5 and 6 imply that the estimates of the background levels, which depend on the electron efficiency and pion contamination probabilities, are quite accurate.

It is planned to take a spare Čerenkov element to a test beam facility and do a full study of the necessary Z and incidence angle corrections.

4.3 Electron and pion PID signatures

4.3.1 dE/dx in the scintillators

Figure 4.4 shows the variation of dE/dx (measured in S1) with momentum for the two samples of particle tracks: pions and electrons. The horizontal band is due to the electron tracks and the pions give the curved band. This behaviour is as expected from the Bethe-Bloch formula [18, chapter 2]. The Bethe-Bloch formula gives the mean value of the energy lost by a particle per unit path length due to ionization† and is given approximately by

$$\frac{dE}{dx} \propto \frac{1}{\beta^2}$$

Electrons are always ultrarelativistic in the momentum range of CPLEAR, i.e. $\beta \sim 1$ always, and dE/dx is almost constant (actually varying with $\ln\gamma$). Pions however begin to slow down appreciably as the momentum decreases towards $m_\pi c$ and this is reflected in the sharp increase in dE/dx below $\sim$ 170 MeV/c. Below this momentum,

†More correctly, in plastic scintillators the energy loss is due to the excitation of the molecules rather than ionization of electrons.

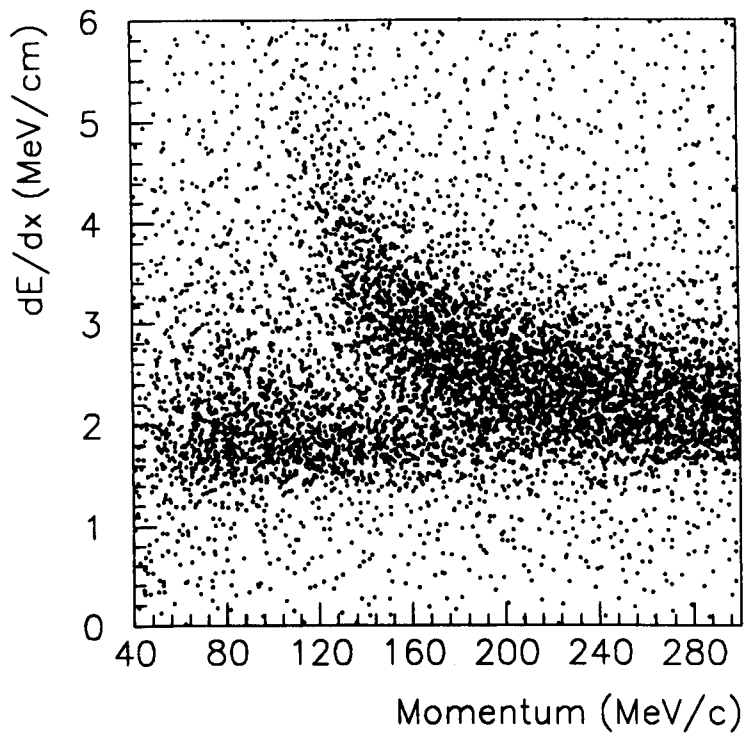

Figure 4.4: dE/dx for pions and electrons as a function of momentum.

electrons and pions are separable using dE/dx but above this the two bands overlap.

The outer scintillator is also instrumented to give dE/dx measurements but as it is only half the thickness of S1 the statistical variation in the energy lost is greater. No benefit has been found in using S2 for dE/dx measurements. It is only used digitally to test whether or not a particle exited the Čerenkov along its extrapolated path.

4.3.2 Čerenkov radiation

For particles passing through the Čerenkov with a velocity, β, greater than the threshold velocity β_t, the amount of light emitted (and hence the number of photoelectrons ejected in the PMs) per unit path length is given by [18, chapter 8]

$$\frac{dN}{dx} \propto \frac{d\Lambda}{dx} \propto 1 - \left(\frac{\beta_t}{\beta}\right)^2 \tag{4.1}$$

The FC72 has $\beta_t = 0.8$ and this corresponds to a momentum threshold of approximately 180 MeV/c for pions, whereas $\beta \sim 1$ for electrons which always give Čerenkov radiation. Figure 4.5 shows the variation with track momentum of the total number

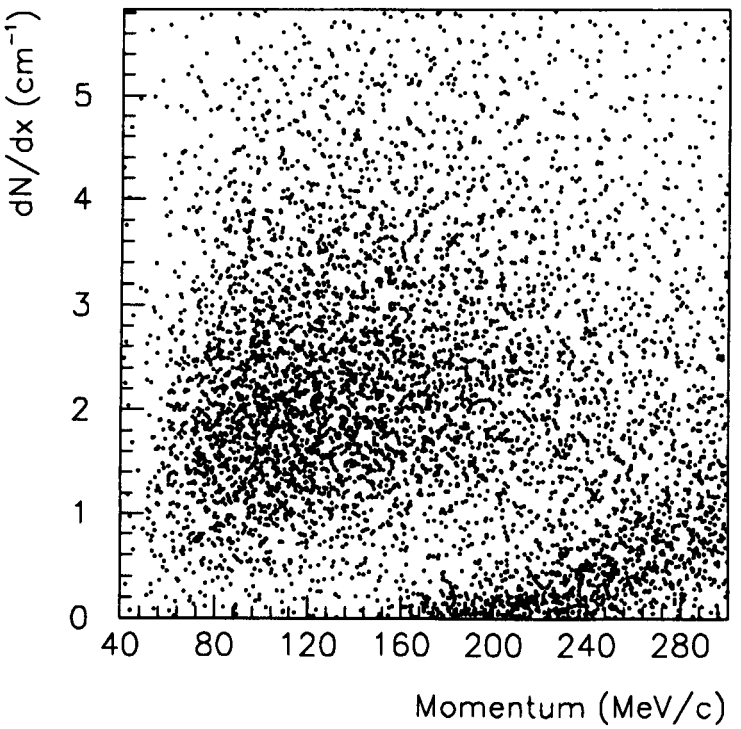

Figure 4.5: dN/dx for pions and electrons as a function of momentum.

of photoelectrons per unit path length: dN/dx.

The electron tracks would form a band of constant dN/dx, but since the sample of electrons has momenta mainly below 160 MeV/c the distribution looks more like a mound. The pion tracks give a better defined band which starts with $dN/dx \sim 0$ between 160 – 240 MeV/c and then increases with momentum. The pion band does not start to rise until after 200 MeV/c because of the energy lost by the pions in traversing the PID elements. A track which is determined to be just above the Čerenkov threshold in the tracking chambers is slowed down as it passes through the PID and may be below threshold for part of its passage through the Čerenkov, thus

giving less light than expected. Note that particles still lose as much energy through atomic and molecular excitation in the Čerenkov as they do in S1 but the Čerenkov material does not respond by emitting scintillation light.

At these low momenta a significant number of tracks ($\sim$ 13% of tracks with a momentum below 200 MeV/c) curve sufficiently to exit the PID through the S2 of the sector next to the S1 sector through which they entered. This implies that the particle has passed through two Čerenkov elements and the signals measured in both must be combined. Since all energy loss in matter is of a statistical nature, longer path lengths imply more accurate measurements of dN/dx. I thus combine the two measurements of the number of photoelectrons per unit path length with a weighting equal to the square of the path length

$$\frac{dN}{dx} = \frac{1}{L_1^2 + L_2^2}\left(L_1^2\left(\frac{dN}{dx}\right)_1 + L_2^2\left(\frac{dN}{dx}\right)_2\right) \tag{4.2}$$

Tracks which bend more than this are extremely ($< 1\%$) rare and are ignored.

4.4 Selection criteria

Just as an $S\overline{C}S$ signature is used to identify kaons, so an SCS signature, i.e. signals in S1, S2 and the Čerenkov, for a track with a momentum below 180 MeV/c, the pion momentum threshold, implies that the track is an electron. This is an unnecessarily restrictive criterion for electron identification. The set of criteria developed extend the scope of electron-pion separation to deal with tracks which have no S2 hit or a momentum above 180 MeV/c.

In this section I first describe the criteria for electron identification and then explain some of the reasoning behind them. Figure 4.6 shows a schematic of how the selection criteria are applied to a candidate electron track.

The first criterion is that the PID signals, i.e. the amount of scintillation and Čerenkov light, of the electron candidate track are free from contamination from other tracks.

To avoid overlapping signals, I define two types of zones: **deposition zones** and **usage zones**. The zones are collections of Čerenkov elements. Each track has its

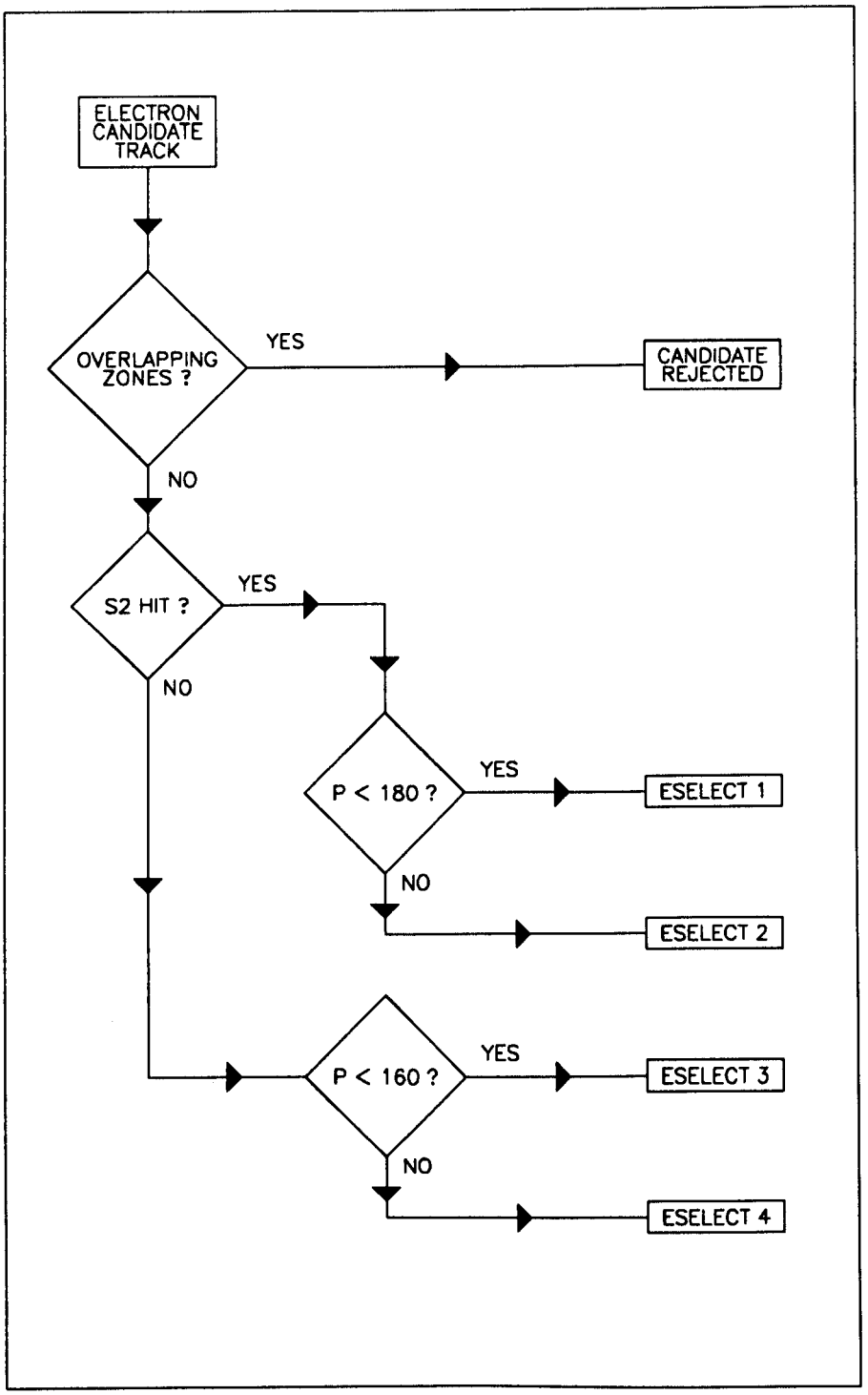

Figure 4.6: A schematic of how the electron selection criteria are applied to an electron candidate track.

own associated usage and deposition zone. The set of Čerenkov elements in which the track could possibly produce light is called the deposition zone. The usage zone is the set of elements which are used in the electron selection criteria proper. The extent of the two types of zone, i.e. definitions of the sets of elements, are given later in this section.

If a candidate electron track has a usage zone which is overlapped by the deposition zone of a different track, it is rejected, i.e. it is assumed to not be an electron. If a track is free from overlapping zones it is then classified by whether or not it has an associated S2 hit, and by the value of its momentum (see figure 4.6). According to this classification the track is subjected to one of four selection criteria, termed ESELECT1 to ESELECT4.

The selection criteria are graphical and are shown in figures 4.7 to 4.10, applied to the electron and pion track samples. Depending on its classification, the track is represented by a point in one of the four selection planes. The coordinate axes for each of the planes is shown below

Selection criterion	$Y - X$ axes
ESELECT1	$dE/dx - dN/dx$
ESELECT2	$dN/dx - p$
ESELECT3	$dE/dx - N$
ESELECT4	$N - p$

Each selection criterion consists of a bounded region in the plane (see figures 4.7 to 4.10). If the point representing the track is within the bounded region, then the track is accepted as an electron.

For example, a track with an S2 hit and a momentum of 220 MeV/c must satisfy the selection criterion ESELECT2, i.e. the point defined by $(dN/dx, p)$ must fall within the bounded region of figure 4.8, in order to be accepted as an electron.

For tracks with an S2 hit, the selection criteria (ESELECT1 and ESELECT2) are reasonably self-explanatory. For tracks below 180 MeV/c, both dN/dx and dE/dx differ for pion and electron tracks. Thus ESELECT1 is a bounded region in the plane dE/dx vs. dN/dx, see figure 4.7. Above $\sim$ 180 MeV/c dE/dx loses its usefulness and pions start to give light in the Čerenkov as given by equation 4.1. The selection criteria ESELECT2 is a momentum dependent cut on the number of photoelectrons

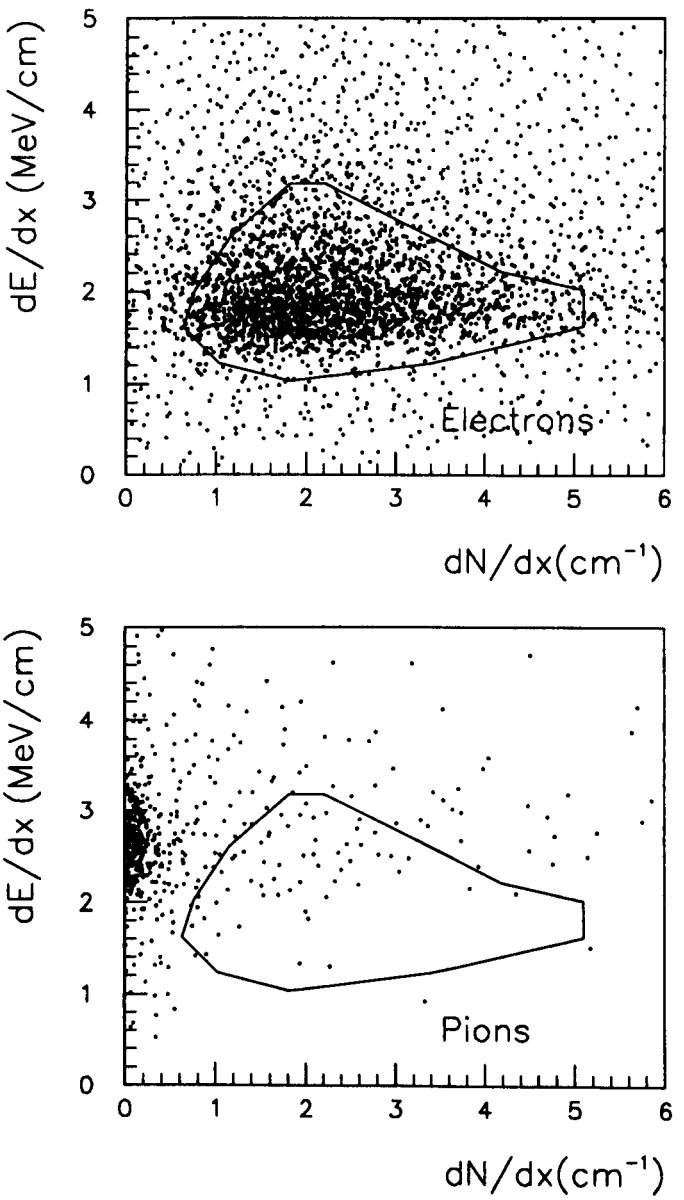

Figure 4.7: Selection criterion ESELECT1.

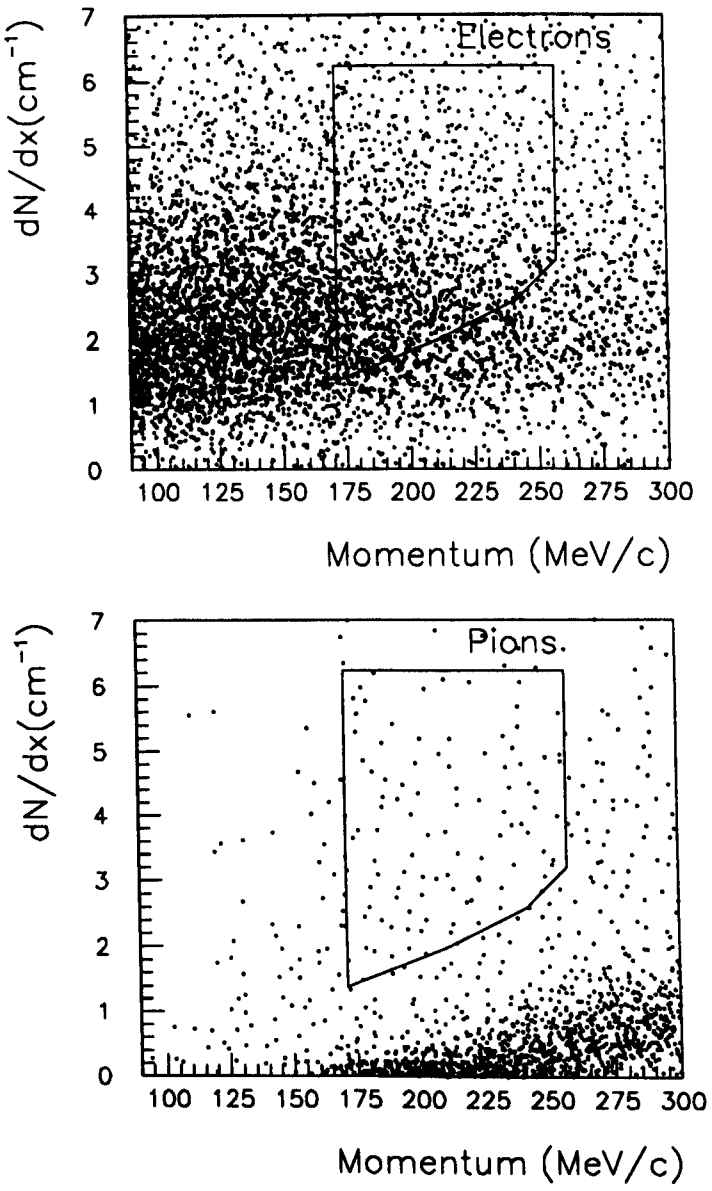

Figure 4.8: Selection criterion ESELECT2.

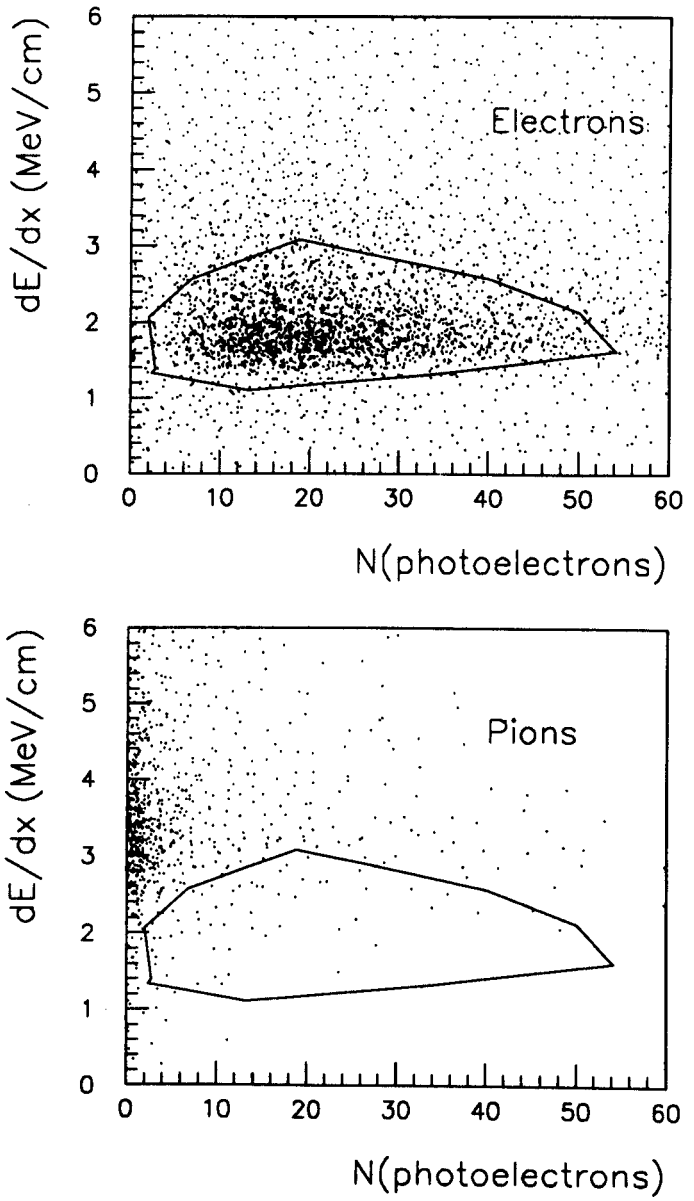

Figure 4.9: Selection criterion ESELECT3.

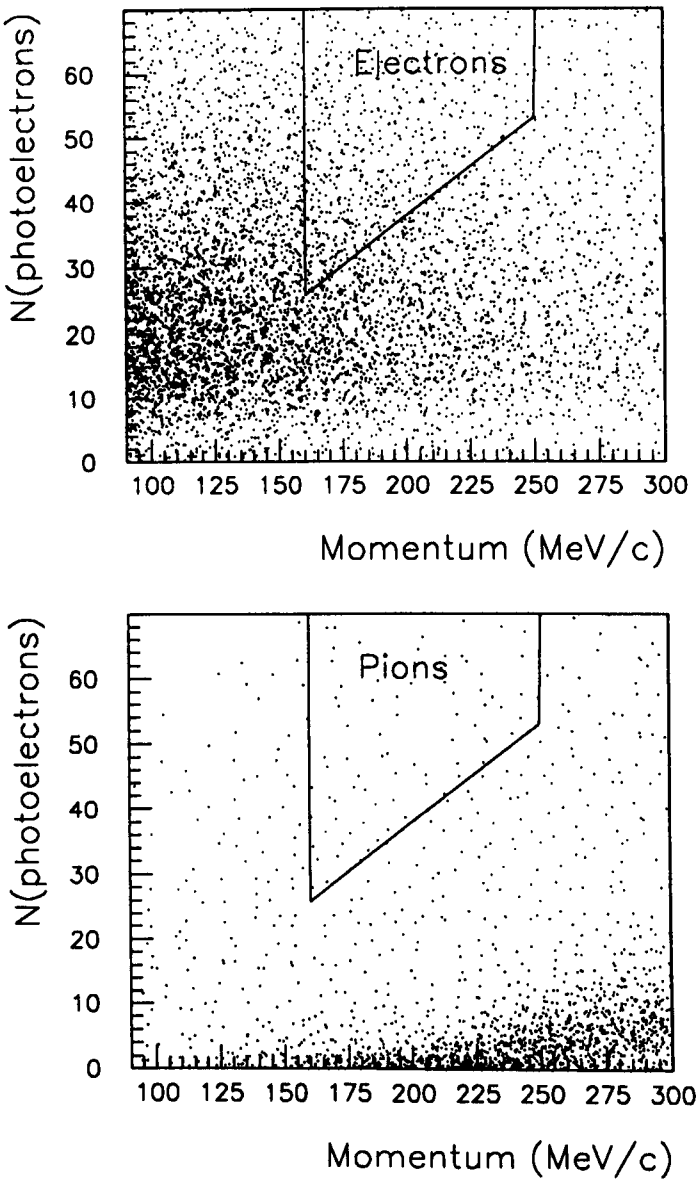

Figure 4.10: Selection criterion ESELECT4.

per unit path length.

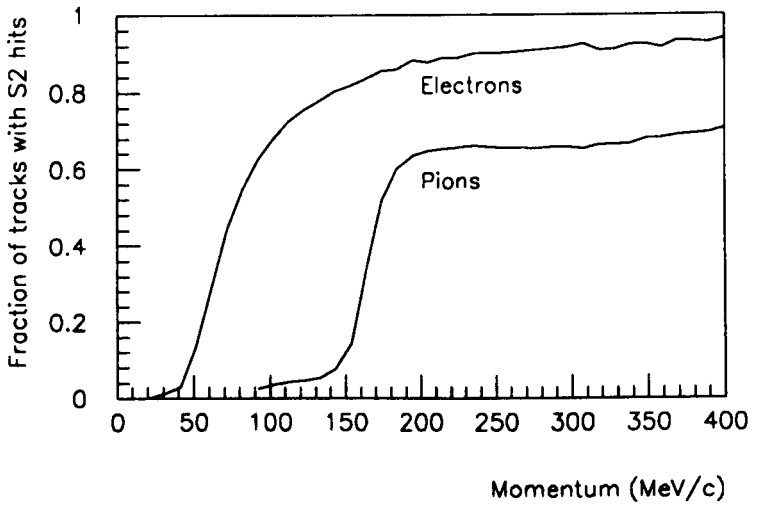

Figure 4.11: Fraction of pion and electron tracks giving a signal in the outer scintillator.

Tracks with no S2 hit are a result of either the particle stopping in the Čerenkov, or else being scattered into a neighbouring sector. In either case the path length in the Čerenkov, calculated by extrapolation, may not be accurate. Figure 4.11 shows the fraction of pion and electron tracks with S2 hits as a function of momentum. The sudden decrease in the fraction of pions reaching S2 is a result of the sharp increase in dE/dx for pions as the momentum falls below $\sim$ 180 MeV/c. At 150 MeV/c, pions have a range in the PID of about 10 cm [4, page III.20]

For tracks with no S2 hit the total number of photoelectrons, N, is used in the selection criteria as opposed to dN/dx. In addition, whereas for tracks with an S2 hit, the number of photoelectrons includes only those in the Čerenkov element through which the track is extrapolated; for tracks with no S2 hit the number of photoelectrons is the sum of those plus the number in the neighbouring Čerenkov elements. For example, if a track is extrapolated through sector i and the number of photoelectrons

detected in sector j is $N(C_j)$, then

$$N = N(C_{i-1}) + N(C_i) + N(C_{i+1}) \tag{4.3}$$

There are two reasons for this. Tracks which have been scattered into a neighbouring Čerenkov element may give rise to a signal there and not in the element through which the track is extrapolated. Secondly there is some evidence that an electron track passing through a given sector gives rise to some light in the two neighbouring sectors. Figure 4.12 shows the distribution of the fraction, f, of the total number of photoelectrons in all three Čerenkov elements which are deposited in the element through which the track actually passed, i.e.

$$f = \frac{N(C_i)}{N(C_{i-1}) + N(C_i) + N(C_{i+1})}$$

This may be a result of Bremsstrahlung which, for electrons, is the dominant mech-

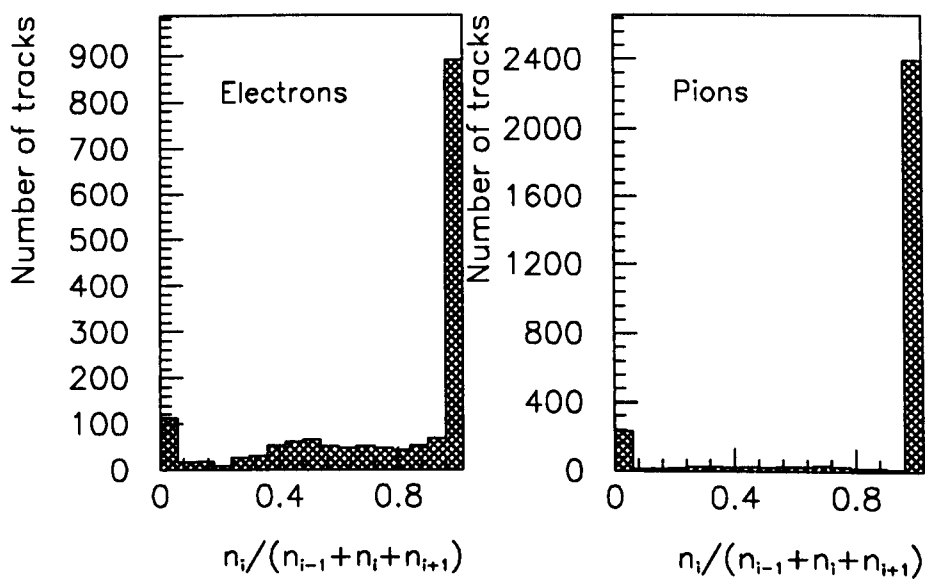

Figure 4.12: The fraction of the total number of photoelectrons associated with a track which are deposited in the central Čerenkov element, i.e. the element through which the track is extrapolated.

anism for energy loss above $\sim$ 90 MeV/c.

With regard to dE/dx in S1, there is no evidence of signals in the scintillators adjacent to those through which tracks are extrapolated.

The two selection criteria applied to tracks with no S2 hit (ESELECT3 and ESELECT4) are similar to those applied to tracks with S2 hits, except that N (defined by 4.3) is used instead of dN/dx.

The usage zones are dictated by the above considerations. They are defined in figure 4.13. For a track passing through the PID and giving both S1 and S2 hits in sector i (figure 4.13 (a)) dN/dx is just given by $N(C_i)$ divided by the extrapolated path length. Tracks with an S2 hit in an adjacent sector have dN/dx defined by equation 4.2. For tracks without an S2 hit N as given by equation 4.3 is used as opposed to dN/dx.

For tracks with S1 and S2 hits, no use is made of the Čerenkov signals in the neighbouring sectors. This is to keep the usage zone narrow and to reduce the probability of an overlap with the deposition zone of another track.

The deposition zones are defined in figure 4.14. They are different for primary and secondary tracks. Figure 4.12 shows that pions only infrequently give rise to light in neighbouring Čerenkov elements. Kaons give no light in the Čerenkov as they are below the momentum threshold up until $\sim$ 700 MeV/c. Above this they behave like the pions and give light only in the Čerenkov element through which they pass. Since primary tracks are either pions or kaons the primary deposition zones are given by just those sectors through which the tracks pass. Since a secondary track may be an electron, the deposition zone must in addition include the neighbouring Čerenkov elements, see figure 4.14.

4.5 Efficiency and contamination

Using the samples of electron and pion tracks I can determine the probability for a track of a given momentum to be identified as an electron given that I know that it is a pion or an electron. These are denoted $P(e|\pi)$ (pion contamination) and $P(e|e)$ (electron efficiency). These probabilities are determined for each running period. They are used in the Monte Carlo to calculate background levels as described in

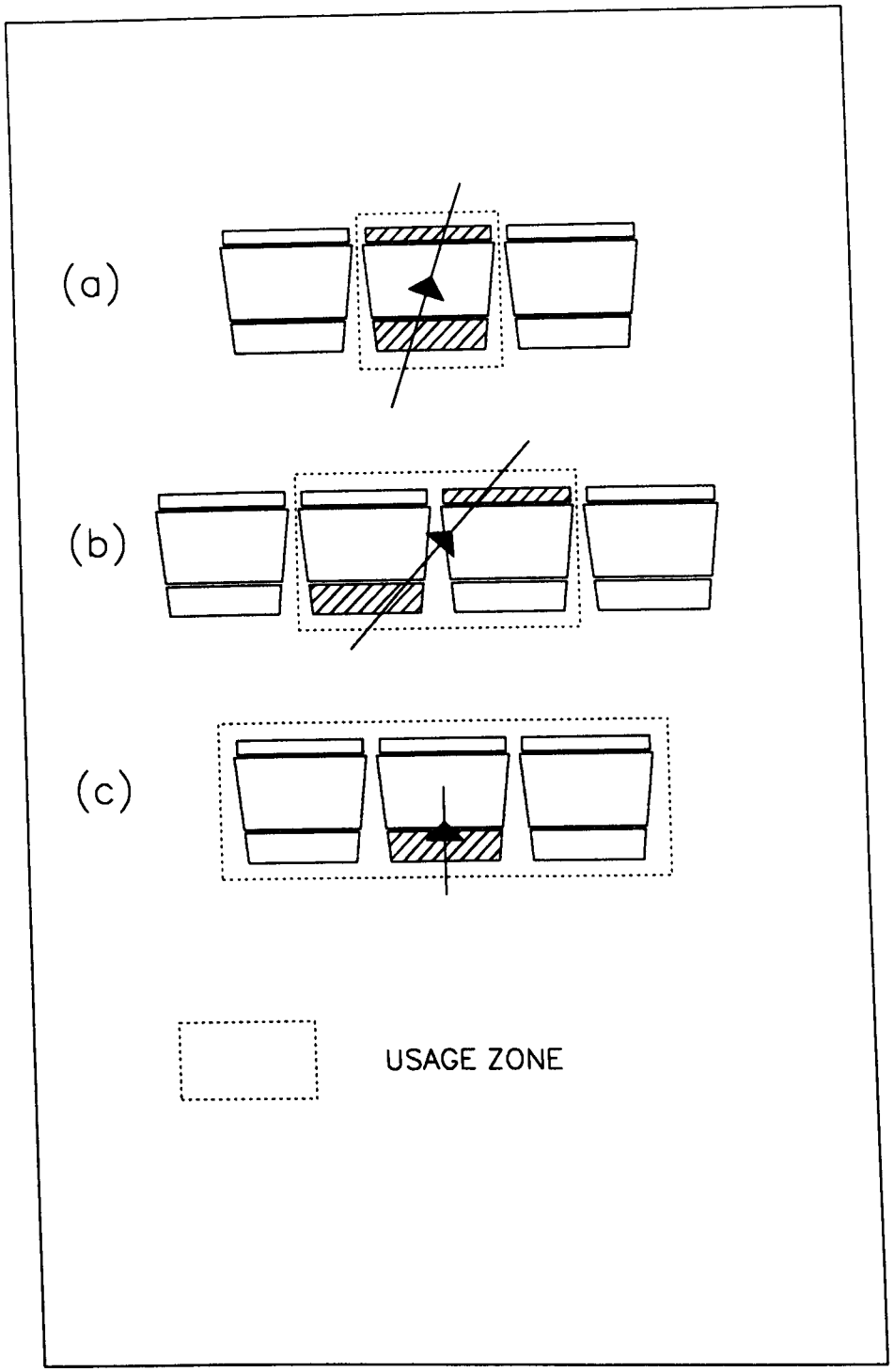

Figure 4.13: Usage zones for candidate electron tracks. Those scintillators in which the track gives a signal are shown shaded.

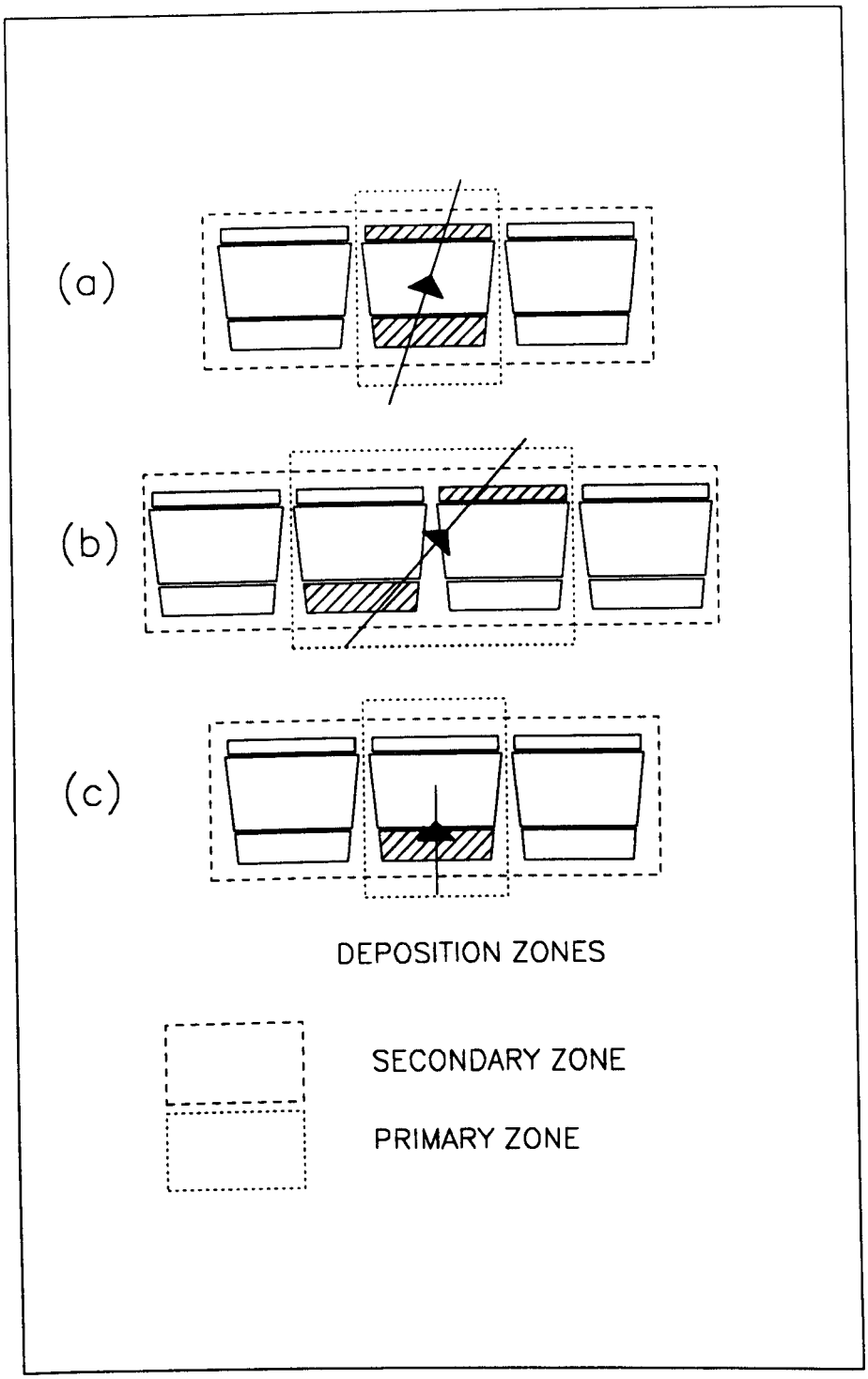

Figure 4.14: Deposition zones as defined for primary tracks (primary zones) and secondary tracks (secondary zones). Tracks which give hits in the inner and outer scintillators (hit scintillators are shown as shaded) in the same sector have zones as shown in (a). Tracks with inner and outer scintillator hits in neighbouring sectors have zones as in (b) and tracks with no outer scintillator hit have zones as shown in (c).

section 5.5.2.

Figures 4.15 and 4.16 show the probabilities $P(e|e)$ and $P(e|\pi)$ as functions of momentum. These two plots are produced from period 8 data. There are similar distributions for all of the other data sets used in the analysis. These are necessary as the probabilities varied from period to period (see sections 5.5.1 and 5.5.2).

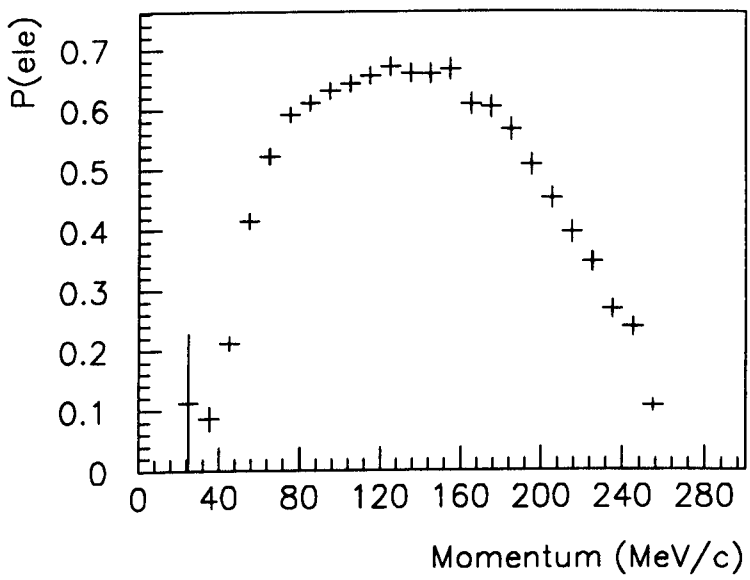

Figure 4.15: The electron selection efficiency $P(e|e) = \frac{1}{2}(P(e^+|e^+) + P(e^-|e^-))$, i.e. the probability to identify an electron correctly, as a function of momentum.

At low momenta there is a problem determining $P(e|\pi)$ since the pion sample consists of primary pions and these all have momenta in excess of 70 MeV/c if they reach the outer scintillator. There is no reason to suppose that $P(e|\pi)$ in this region increases above its average value in the measured region, i.e. $\sim$ 1%. To check this using secondary pion tracks a clean sample of $\pi^+\pi^-\pi^0$ decays would be needed as $\pi^+\pi^-$ decays also tend to give high momentum (i.e. $>$ 100 MeV/c) pions. The separation of three pion and semileptonic decays at a level much greater than 1 % would be need in order to measure $P(e|\pi)$ and (if it is possible) would need a lot of work.

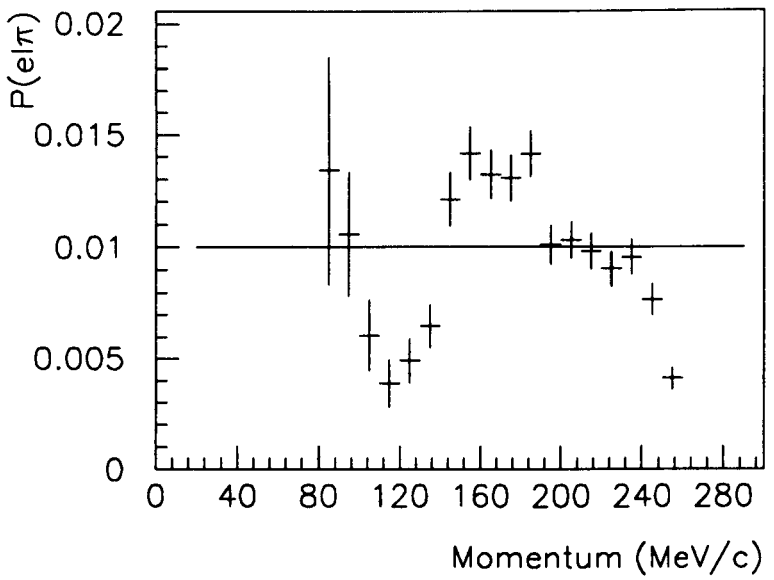

Figure 4.16: $P(e|\pi) = \frac{1}{2}(P(e^+|\pi^+) + P(e^-|\pi^-))$, the probability to identify a pion as an electron as a function of momentum. The line corresponds to 0.01, i.e a 1% chance for a pion to pass the selection criteria.

An interesting point is the charge symmetry of the electron identification, i.e. the difference between $P(e^+|e^+)$ and $P(e^-|e^-)$ and between $P(e^+|\pi^+)$ and $P(e^-|\pi^-)$. The ratio of electron selection efficiency to positron selection efficiency is shown in figure 4.17 along with the corresponding pion contamination probability ratio $P(e^+|\pi^+)$: $P(e^-|\pi^-)$. For the leptons

$$\frac{P(e^+|e^+)}{P(e^-|e^-)} = 0.995 \pm 0.005$$

i.e. consistent with one to better than one percent. For the pion contamination probability, however,

$$\frac{P(e^+|\pi^+)}{P(e^-|\pi^-)} = 1.05 \pm 0.02$$

which is a two standard deviation from one. This effect of a charge asymmetry in the pion contamination is considered in sections 6.2 and 6.6.

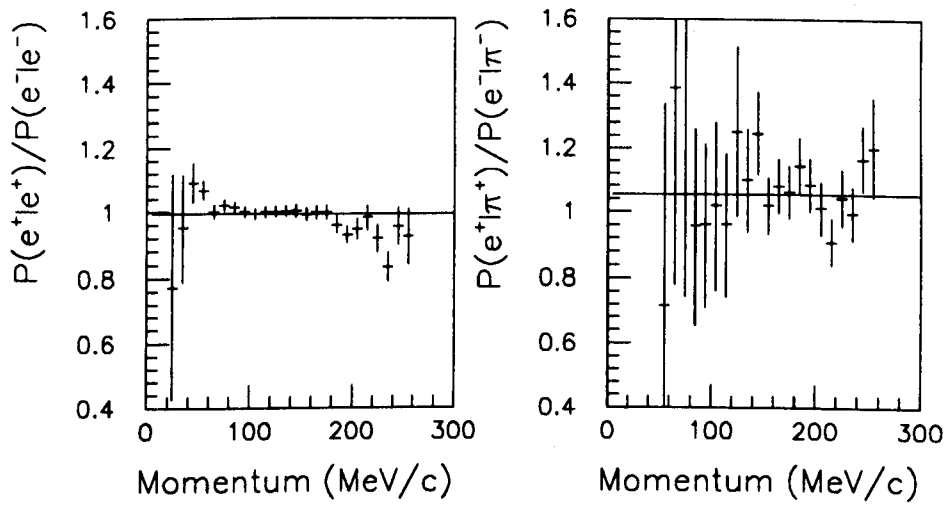

Figure 4.17: Ratios of the selection probabilities for positive and negative pions and electrons. The lines are the fitted mean values.

4.6 Acceptance of muon tracks

So far in this chapter I have completely ignored muon tracks. For the purpose of making a mass difference measurement, it is not important whether a semileptonic decay has a muon or an electron in the final state; the time distributions of the decays are the same. Only a small percentage of muon tracks are expected to be accepted as electrons because muons have a momentum threshold in the Čerenkov of $\sim$ 140 MeV/c. However, in calculating the amount of background (from $\pi^+\pi^-$ and $\pi^+\pi^-\pi^0$ decays) in chapter 6 the fraction of muon type semileptonic decays accepted into the final event sample forms a small correction. To estimate the size of this correction from Monte Carlo, it is necessary to estimate $P(e|\mu)$ — the probability to accept a muon track as an electron.

The efficiency of electron selection and the pion contamination probability can be determined empirically from the particle samples. Unfortunately there is no clean muon sample available. I have thus attempted to determine $P(e|\mu)$ from the sample of pion tracks making use of the universal velocity dependence of dE/dx and dN/dx

A muon of momentum p_μ has the same velocity as a pion of momentum, p_{equiv}, where $p_{equiv} = p_\mu(m_\pi/m_\mu)$. Thus a muon of this momentum should have the same mean energy loss and number of photoelectrons per unit path length as a pion of momentum p_{equiv}. It should also have the same distributions about these mean.

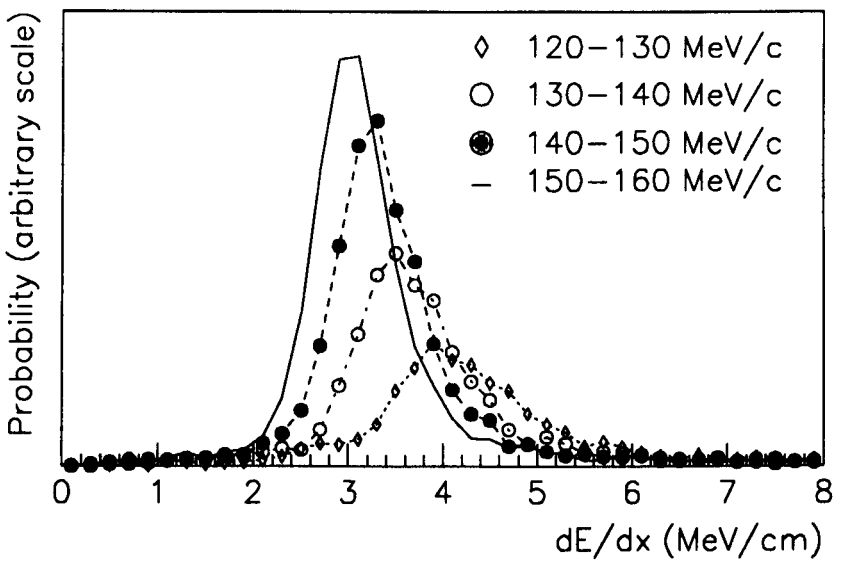

Figure 4.18: Probability curves for dE/dx corresponding to four adjacent momentum slices. Specific values of dE/dx are generated randomly according to these distributions.

The estimation of $P(e|\mu)$ is a two stage process. The distributions of dE/dx vs. momentum and dN/dx vs. momentum for pion tracks are sliced into strips 10 MeV/c wide. For any given momentum this gives a distribution of dE/dx and dN/dx. Normalizing these gives probability distributions for a track of a given momentum to have a certain value of dE/dx and dN/dx. As an example four dE/dx probability distributions for four different momentum ranges are shown in figure 4.18.

The second stage is to generate a set of random muon track momentum values $\{p_\mu\}$. For each generated value of p_μ, values of dE/dx and dN/dx are generated. They are generated according to the probability curves corresponding to the equivalent

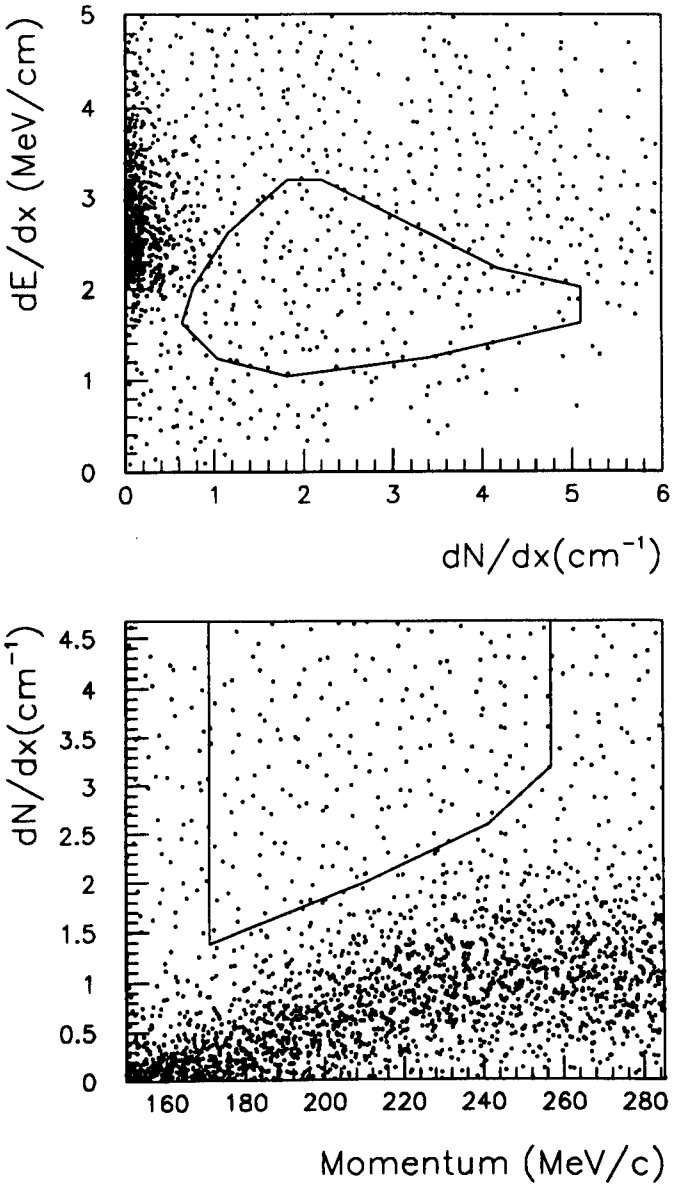

Figure 4.19: Simulated distributions of dE/dx vs. dN/dx and dN/dx vs. momentum for muon tracks. The bounded regions of the ESELECT1 and ESELECT2 selection criteria are superposed.

momentum p_{equiv}. This gives a set of vectors $\{(p_\mu, dE/dx, dN/dx)\}$ which are passed through the electron selection criteria.

Figure 4.19 shows the distributions obtained with the ESELECT1 and ESELECT2 selection regions superposed. (Muons are assumed to always pass through the outer scintillator).

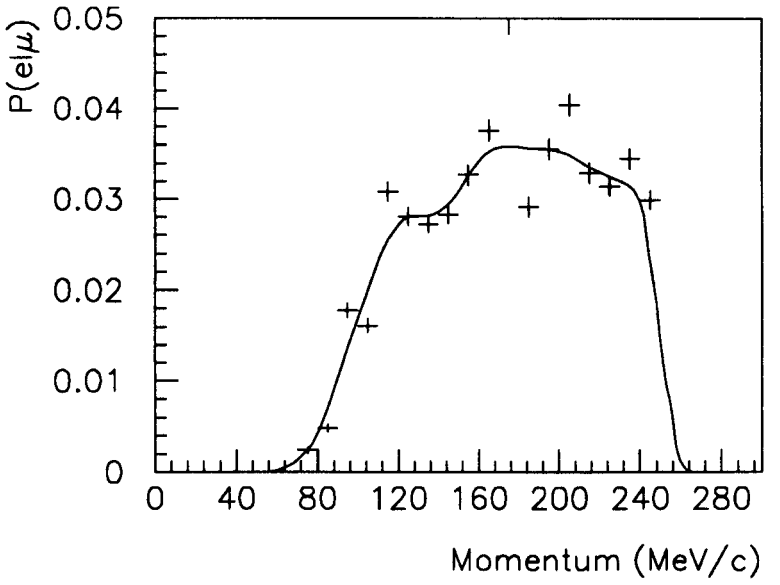

Figure 4.20: The probability to identify a muon as an electron, $P(e|\mu)$, as a function of momentum.

The resulting probability of identifying a muon as an electron is shown in figure 4.20 In the figure, the small errors on the points reflect the large number of muon tracks generated. The scatter on the points is dominated by the statistics of the pion distributions used, and hence the apparent discrepancy between the scatter of the points and the size of the error bars. The smoothed probability distribution, represented by the curve, is used in the Monte Carlo simulation (see section 5.2).

Chapter 5

Event selection

5.1 Introduction

In this chapter I describe the selection of a sample of semileptonic decays of neutral kaons. The chapter is divided into three sections. In the first section I describe the selection of events from data taken with IDL 4 trigger configurations. This data covers the eigentime region above $3\tau_S$, and I refer to it as large eigentime data. The second section deals with event selection from small eigentime data, i.e. data taken with IDL 2 trigger configurations. In general these events have four tracks originating from within the PCs, and have eigentimes from $0\tau_S$ upwards. The third section details acceptance measurements for semileptonic decays, and for two and three pion decays which form the main background. These are determined from Monte Carlo simulation.

The selection of semileptonic decays relies on electron identification, but to develop an electron identification procedure I have used other types of events, from which pure samples of pions and electrons could be isolated. In large eigentime data samples, in addition to identifying golden events, I also looked for events with secondary tracks due to gamma conversions. Gamma conversions are identified from the opening angle of the secondary tracks, which is very close to zero. These events provide a very clean sample of electron and positron tracks. A clean sample of pions is obtained as a consequence of the golden event selection, as the primary track that is not a kaon is necessarily a pion. The only problem with this pion sample is that the momenta of

the tracks tend to be a little high, i.e. the momentum range of interest is $\sim 50 - 250$ MeV/c, whereas primary pion momenta are mostly in excess of 100 MeV/c.

Most of the selected events come from the large eigentime data, because small eigentime data is dominated by $\pi^+\pi^-$ decays. The relative abundances of the decay states can be estimated from

$$N(K_{L,S} \to f) = \int dt A(t) \frac{dN}{dt}_{L,S} BR(K_{L,S} \to f)$$

where $A(t)$ is the trigger acceptance as a function of eigentime and $BR(K_{L,S} \to f)$ is the branching ratio of K_L and K_S decays to the final state f. IDL 2 trigger configurations accept events with eigentimes right down to zero and approximately 90% of the data is below $4\tau_S$. Using the branching ratios for neutral kaon decays we can deduce the approximate amounts of each decay mode present in the small eigentime data as a fraction of the number of $\pi^+\pi^-$ events.

Decay Mode	Number of decays per 1000 $\pi^+\pi^-$ decays
$\pi^+\pi^-\pi^0$	1.3
$\pi^\pm\mu^\mp\nu$	2.8
$\pi^\pm e^\mp\nu$	4.1

Only about half a percent of the small eigentime data consists of semileptonic events. If the semileptonic event selection accepts one percent of $\pi^+\pi^-$ decays then a small eigentime sample of selected semileptonic decays would actually be two thirds background. This can be contrasted with the eigentime region between $5\tau_S$ and $12\tau_S$ where about half of the neutral kaon decays are to semileptonic final states.

5.2 Monte Carlo simulation

The CPLEAR Monte Carlo simulation is built around the standard CERN GEANT package. Event generation is performed by a routine specifically written for the experiment to contain all of the known annihilation resonances. The tracking of the particles through the detector is performed by GEANT. Detector resolutions and responses are determined from real data and then input into the Monte Carlo to ensure a faithful simulation.

I have used the simulation for two main purposes: to test event selection criteria and to estimate background levels in the final event sample. The Monte Carlo data is written in the same format as the real data so that it can be read by the same analysis programs. In addition it has extra information on the true nature of the event.

To determine the level of background accepted by the analysis, sets of Monte Carlo data of a specific decay type, say $\pi^+\pi^-$ decays, are passed through the program.

My analysis is centred around electron identification and is dependent on the Čerenkov response. In order to limit the dependence of the analysis on the Monte Carlo simulation, I use the empirically measured values of $P(e|e)$ and $P(e|\pi)$ as functions of momentum to do electron identification. When the program loops over the electron candidate tracks I treat simulated data differently to real data. This is the only place where simulated data and real data are treated differently.

For real data the program takes the PID information for the track (dE/dx and dN/dx) and passes it to the electron selection procedure for testing. For Monte Carlo data the program looks at the tracks's true particle type, X, and its true momentum, p, from the extra information which the Monte Carlo data contains. This information gives a probability, $P(e|X)$, for the particle to be identified as an electron. The program then returns to treating simulated and real data identically again.

There are two major differences between the Monte Carlo simulation and real data.

- The strong interaction package GEISHA is not tuned to low energy interactions. Thus the CPLEAR Monte Carlo is run with an option that suppresses particle creation in hadronic interactions, i.e. if a particle interacts strongly with the material of the detector it just disappears! Thus the Monte Carlo produces no backscatters.

- The neutral kaon decays are produced with flat eigentime distributions, giving the same statistical accuracy for all eigentimes.

5.3 Large eigentime selection

5.3.1 Outline of selection criteria

The selection of semileptonic decays from large eigentime data is a two stage process. The first stage is to identify golden events with a final state containing two charged tracks plus perhaps neutrals. The second stage is to separate out those golden events where the final state is semileptonic.

In order to be selected as golden, an event must satisfy a number of conditions. The primary tracks must be consistent with $p\bar{p} \longrightarrow \pi K K^0$; $p\bar{p} \longrightarrow \pi K K^0 n\pi^0$ annihilations are rejected. The secondary tracks must be consistent with being neutral kaon decay products; they must not be due to a gamma conversion or a backscattered track. Events where the secondary tracks are due to gamma conversions are used to measure the electron identification efficiency, and then rejected. Every golden event provides a definite pion track, the primary pion, which is used to determine $P(e|\pi)$.

To select semileptonic decays from the golden events I look for events where one of the secondaries is identified as an electron. Since $K^0 \rightarrow e^+e^-$ or $\mu^+\mu^-$ decays require flavour changing neutral currents, which are forbidden in the Standard Model, a secondary electron implies a semileptonic decay. However since $P(e|\pi) \neq 0$ there will always be background decays where the electron is in fact a wrongly identified pion. These are identified from the decay kinematics.

My event selection begins at the miniDST level, and consists of passing events through a series of selection criteria. Events which do not satisfy a criterion are discarded immediately and the analysis restarts with the next event.

The cuts, in order of application, are listed below, and then explained more fully afterwards along with the results of their application, i.e. the percentage of events passing. The percentage of events passing a cut is defined by

$$\% \text{ Passing} = \frac{\text{Number of events passing cut}}{\text{Number of events passing previous cut}} \times 100\%$$

Unless stated otherwise, the figures presented are for a typical set of period 8 data as most of the event selection work was done initially with this data.

- All tracks must have at least:

1. four transverse hits in the DCs,
2. two Z points in the DCs, in addition to any streamer tube hits.

- $-0.9 < \cos\theta_O < 0.95$, where θ_O is the opening angle, in the lab frame, of the secondary tracks.
- The secondary tracks must have no transverse hits inside the radial position of the secondary vertex.
- There must be exactly one primary kaon.
- The primary tracks must form a good vertex.
- The probability from the 1C fit to the primary vertex must be greater than 0.1
- $\cos\theta_C > 0.95$, where θ_C is the angle between the neutral kaon momentum vector and the vertex separation vector.
- The secondary vertex must lie between PC2(PC1) and DC3.

EVENT IS GOLDEN

- Exactly one of the secondary tracks must be identified as an electron.
- $\cos\theta_R > -0.97$, where θ_R is the opening angle of the secondary tracks in the rest frame of the neutral kaon.
- The probability returned by the 2C fit to the whole event must be greater than 0.1.

EVENT IS A SEMILEPTONIC DECAY

5.3.2 Space point information

- All tracks must have at least:
  1. four transverse hits in the DCs,
  2. two hits in the Longitudinal plane in addition to any streamer tube hits.

The purpose of these cuts is to make sure that all of the tracks in the event have sufficient information to enable accurate reconstruction. In the transverse projection tracks are arcs of circles. Three points define a circle, but at least four points are required to test the validity of a track fit via a χ^2 test. A measurement of the longitudinal momentum needs at least two Z points. Two Z points are also needed in the event of a double intersection of two tracks to determine the correct vertex position.

The figures from data, below, are determined by the strip and wire efficiencies in the DCs. The cut on the number of $R\phi$ hits for the secondary tracks is a requirement that the secondary tracks originate from within DC3.

Selection criterion	% passing
≥ 4 $R\phi$ hits for primaries	99.8
≥ 2 Z hits for primaries	95.9
≥ 4 $R\phi$ hits for secondaries	83.4
≥ 2 Z hits for secondaries	87.6

5.3.3 Secondary vertex

- $-0.9 < \cos\theta_O < 0.95$
- The secondary tracks must have no transverse hits inside the radial position of the secondary vertex.

The purpose of the first cut is to eliminate those events where the secondary tracks are not due to neutral kaon decay, i.e. backscatters, cosmics and gamma conversions.

Figure 5.1 shows a backscattered particle which has been fitted as two secondary tracks. A cosmic ray in coincidence with the event would give rise to a similar pair of secondary tracks, characterized by an opening angle $\theta_O \sim 180°$, $\cos\theta_O \sim -1$. Many of these tracks are filtered out during data processing and not written to miniDST however the opening angle distribution still shows a slight upturn around $\cos\theta_O \sim -1$ so I apply a wider cut.

A gamma conversion is the interaction of a photon with matter to form an electron-positron pair. The signature of this type of event is the almost colinear production of the secondaries, i.e. $\cos\theta_O \sim 1$. Typically 6-7% of the events in IDL 4 data samples

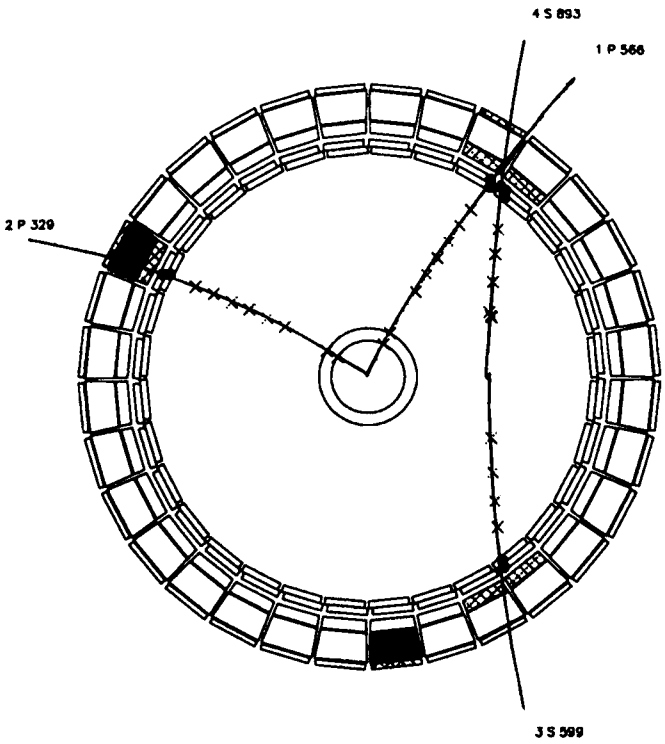

Figure 5.1: A backscattered track interpreted as two secondary tracks.

have secondaries due to gamma conversions and they produce the large peak in figure 5.2.

Events with opening angles in the range $0.95 < \cos\theta_O < 0.99$ are discarded as possible gamma conversions whereas those for which $\cos\theta_O > 0.99$ are almost certainly due to gamma conversions. Though not selected as golden events, these gamma conversions form a very clean sample of electrons and positrons. It is these tracks that I used to develop the electron selection criteria discussed in the previous chapter. They also allow $P(e|e)$ to be determined constantly during all of the running periods.

Three body decays with a zero opening angle between the two (charged) secondary tracks will be accepted as gamma conversions. The amount of background in my gamma conversion sample can be estimated by extrapolating the flat distribution under the peak and amounts to less than 5% of the selected gamma conversions.

The second cut is a test on the quality of the secondary vertex. The secondaries

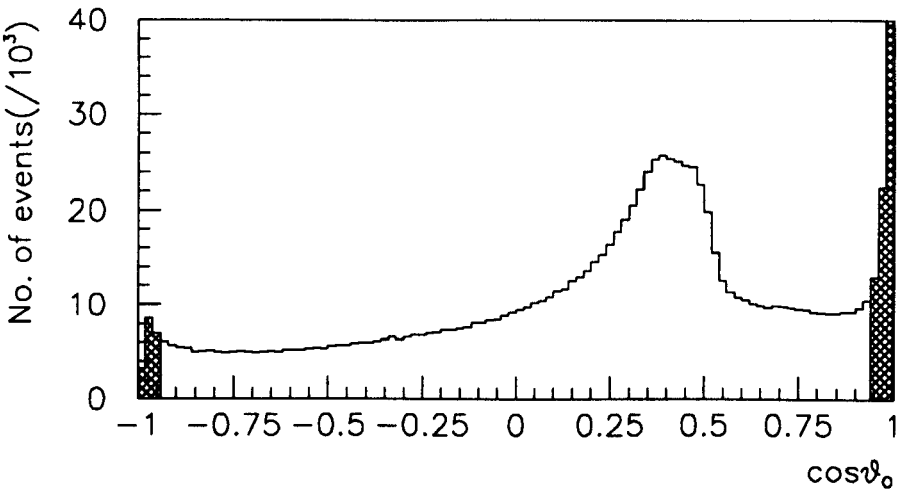

Figure 5.2: Distribution of $\cos\theta_O$ for all events. The gamma conversion peak at $\cos\theta_O \sim 1$ extends above the top of the plot, the last bin containing around 130K events. As $\cos\theta_O \rightarrow -1$ a slight rise due to backscatters can be seen before the drop towards zero due to filter 10. The peak around 0.3 to 0.5 is due to $\pi^+\pi^-$ decays. Events with θ_O lying in the shaded regions are rejected.

are travelling outwards from the secondary vertex and should not give any hits in the drift chambers inside the secondary vertex position. Such hits indicate either a kink in a track or a misinterpretation of the hits. In either case the vertex is incorrect and I discard the event.

Selection criterion	% passing
$-0.9 < \cos\theta_O < 0.95$	83.6
Good secondary vertex	93.0

5.3.4 Primary vertex and vertex connection

- There is exactly one primary kaon.
- Both primary tracks pass within 2.5cm of the primary vertex position.
- The probability from the 1C fit to the primary vertex must be greater than 0.1.
- $\cos\theta_C > 0.95$.

The first cut rejects events where both primary tracks are consistent with being kaons. Those events with no primary kaon are rejected at the data processing stage. The probability to identify a pion as a kaon (offline) varies from 4×10^{-6} at 350 MeV/c (with 60 % kaon efficiency) to 2×10^{-4} at 650 MeV/c (with 40 % kaon efficiency) [15]. This is because as the momentum increases, kaons begin to give signals in the Čerenkov thus reducing the distinction between pions and kaons.

The second criterion tests the quality of the primary vertex. If the tracks are far apart when they should be intersecting, the position of the vertex is in doubt.

The purpose of the third and fourth criteria, above, is to test the hypothesis that the two primary tracks are due to $p\bar{p} \rightarrow \pi K K^0$, as opposed to $p\bar{p} \rightarrow \pi K K^0 n\pi^0$. Prior to P11 no calorimeter information was available and thus the presence of neutral pions at the primary vertex could only be determined from consideration of the charged primary track kinematics. There are two independent tests of this primary vertex hypothesis: four momentum conservation and, the colinearity between the vertex separation vector and the inferred direction of the neutral kaon momentum.

Four momentum conservation

I take the process $p\bar{p} \rightarrow \pi K K^0$ as an event hypothesis for the primary vertex. The momenta of the charged kaon and the primary pion are measured by the tracking chambers, and since their particle types are known, their energies are determined through $E^2 = \boldsymbol{p}.\boldsymbol{p}c^2 + (mc^2)^2$. The neutral kaon is not directly observed and thus the three components of its momentum are unknown. Its energy is determined by its momentum as for the charged primaries. The initial total momentum at the primary vertex is zero and the initial total energy is $2m_pc^2$. Using four momentum conservation gives four equations in three unknowns, i.e. an over-constrained set of equations. This means that the hypothesis can be tested for consistency.

A set of constrained (or kinematic) fit programs has been written within the collaboration to perform this hypothesis testing. A brief outline of constrained fits is given in appendix A and more details can be found in the references given therein.

The 1C fit is used to test the primary vertex hypothesis using the measured momenta of the two charged primary tracks. The output from the fit program consists

of fitted momenta for the two charged primaries and the neutral kaon, and a measure of the probability that the hypothesis is correct. The fit works by varying the fitted momenta of the two charged tracks around the measured momenta in an attempt to minimise a χ^2 function. However the fitted momenta are constrained by four momentum conservation and thus not all of the six components are independent. In fact for the primary vertex there is one dependent momentum component and hence the term 1C fit. When the best fit is found the χ^2 is converted into a probability which can be used as a selection criterion.

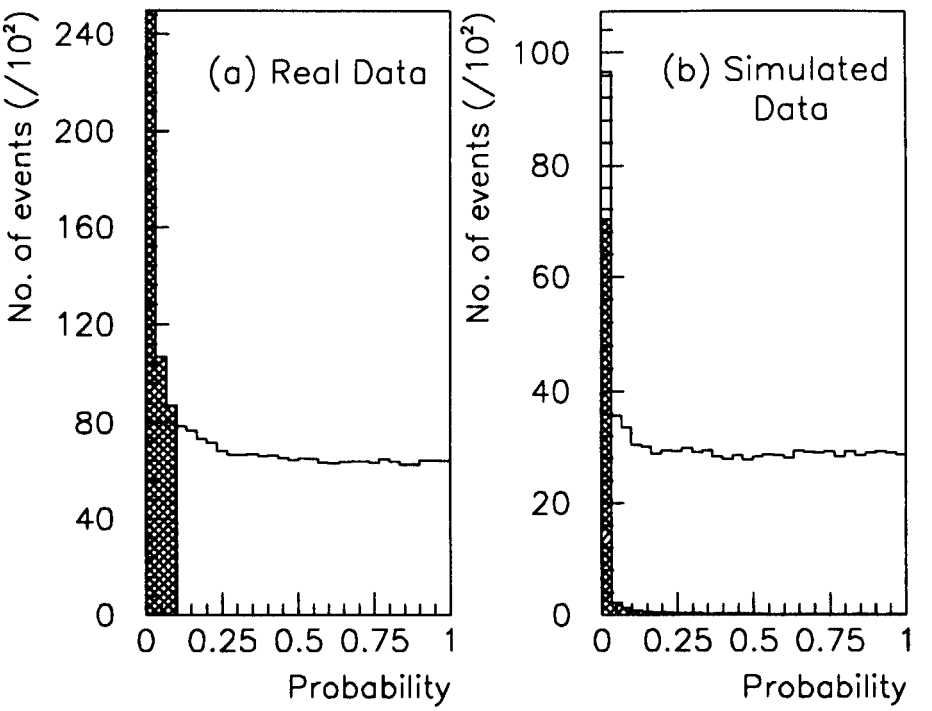

Figure 5.3: 1C probability distributions for real data (a), and simulated data (b).

Figure 5.3 (a) shows the probability distribution from the 1C fit for primary vertices in a large eigentime data sample. The peak at zero extends above the top of the plot. Figure 5.3 (b) shows the results of applying the 1C fit ($p\overline{p} \rightarrow \pi K K^0$ hypothesis) to Monte Carlo generated event samples of $p\overline{p} \rightarrow \pi K K^0$ (unhatched plot) and

$p\bar{p} \rightarrow \pi K K^0 n\pi^0$ (hatched plot).

For the sample where the golden hypothesis is false the probability is clearly peaked around zero. The golden event sample, however, is spread evenly across the probability range from zero to one apart from an excess of about six percent of the events which are also peaked around zero. A flat distribution is expected from applying the fit to a sample of data for which the hypothesis is true.

I cut all events for which the probability is less than 0.1 (the hatched region in figure 5.3(a)). This eliminates 93% of the golden plus π^0, four-body, annihilations, while cutting only 10% of the genuine golden events.

Using the 1C fit probability as a selection criterion is almost the same as selecting on the missing mass of the primary vertex, defined by

$$(m_{miss}c^2)^2 = E_{miss}^2 - c^2 \boldsymbol{p}_{miss}.\boldsymbol{p}_{miss}$$

and determined by the measured charged primary momenta through

$$\begin{aligned} \boldsymbol{p}_{miss} &= -(\boldsymbol{p}_\pi + \boldsymbol{p}_K) \\ E_{miss} &= 2m_p c^2 - (E_\pi + E_K) \end{aligned}$$

If the hypothesis that the primary vertex is a golden annihilation is correct, then the missing momentum and energy will be equal to the momentum and energy of the neutral kaon, and the missing mass will be equal to m_{K^0}.

The presence of neutral pions at the primary vertex will give $m_{miss} > m_{K^0}$ as can be seen from considering the case of one neutral pion at the primary vertex:

$$\begin{aligned} (m_{miss}c^2)^2 &= (E_{\pi^0} + E_{K^0})^2 - |\boldsymbol{p}_{\pi^0} + \boldsymbol{p}_{K^0}|^2 c^2 \\ &= E_{K^0}^2 + E_{\pi^0}^2 + 2E_{K^0}E_{\pi^0} - |\boldsymbol{p}_{K^0}|^2 c^2 - |\boldsymbol{p}_{\pi^0}|^2 c^2 - 2\boldsymbol{p}_{K^0}.\boldsymbol{p}_{\pi^0} c^2 \\ &= (m_{K^0}c^2)^2 + (m_{\pi^0}c^2)^2 + 2(E_{K^0}E_{\pi^0} - \boldsymbol{p}_{K^0}.\boldsymbol{p}_{\pi^0} c^2) \\ m_{miss}^2 &> m_{K^0}^2 + m_{\pi^0}^2 \end{aligned}$$

Figure 5.4 shows missing mass distributions for Monte Carlo simulations of three body (a) and four body (b) annihilations. Figure 5.4 (c) shows the missing mass

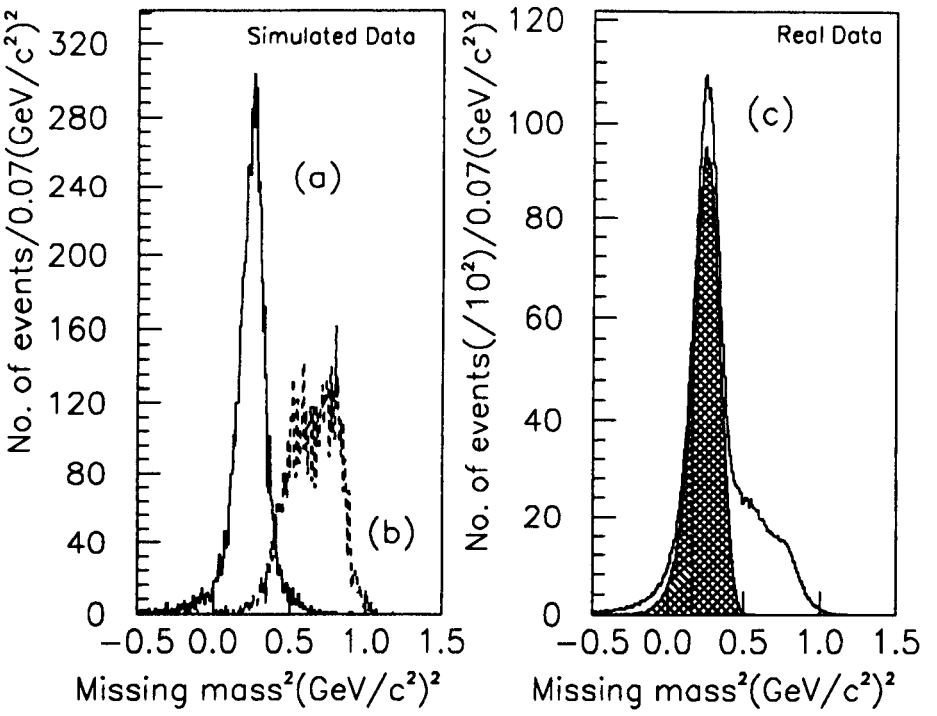

Figure 5.4: Distributions of m^2_{miss} from Monte Carlo simulation, (a) and (b), and from data, (c).

distribution of large eigentime data. Before any primary vertex cuts are applied, the distribution consists of the large three body peak and a shoulder due to events with extra neutral pions. The hatched plot in (c) shows the distribution for all those events that are passed by the 1C fit as golden. This shows the strong correlation between selecting on missing mass and selecting on the 1C fit probability. The advantage of using the fit program is that, as well as providing a selection criterion, it also gives an improved measure of the neutral kaon momentum over simply putting $\boldsymbol{p}_{K^0} = \boldsymbol{p}_{miss}$.

Colinearity

The second test of the three body annihilation hypothesis is the colinearity of the vertex separation vector, $\boldsymbol{\Delta}$, as defined in section 2.1, with the inferred direction of

the neutral kaon momentum, determined by the 1C fit.

Any difference in the direction of these two vectors, larger than that is expected from a finite resolution, implies that the inferred neutral kaon momentum is wrong or that one of the vertices is badly reconstructed. In either case the event is rejected.

A measure of the colinearity between the two vectors is given by θ_C, defined by

$$\cos\theta_C = \frac{\boldsymbol{\Delta}.\boldsymbol{p}_{K^\circ}}{|\boldsymbol{\Delta}|\,|\boldsymbol{p}_{K^\circ}|}$$

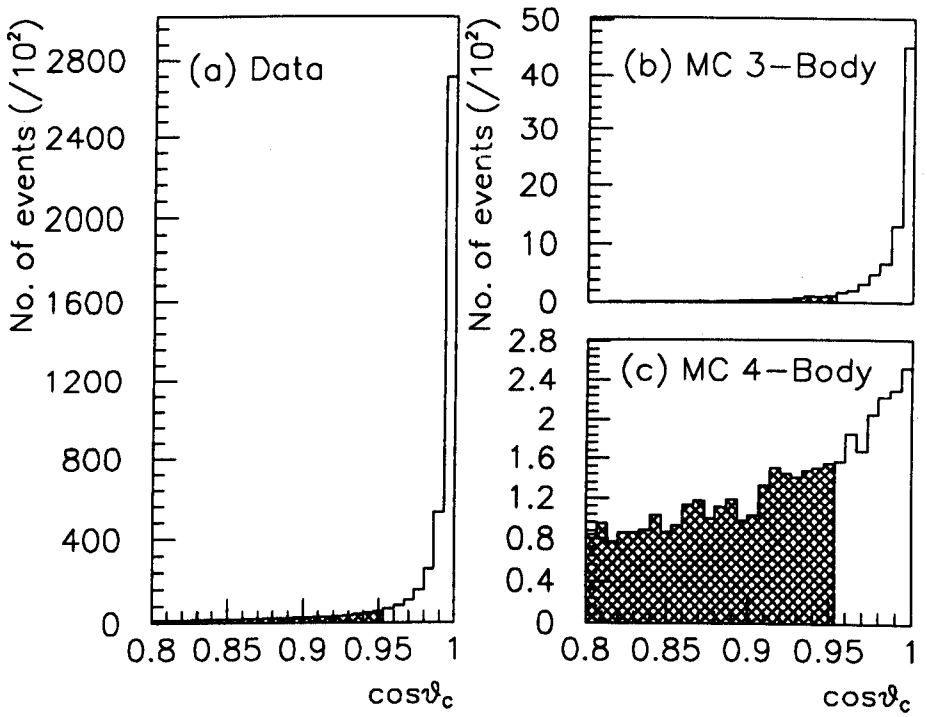

Figure 5.5: Distributions of $\cos\theta_C$ from data (a) and from Monte Carlo simulated events without a primary neutral pion (b), and with a primary neutral pion (c). The hatched regions in (a), (b) and (c) show the rejected events.

Figure 5.5 shows the distributions of $\cos\theta_C$ for real data, (a), and Monte Carlo simulated data, (b) and (c). Plot (a) is for those events which pass the 1C primary vertex fit. The distribution is heavily peaked around $\cos\theta_C \sim 1$ showing the predominance of three body annihilations after the 1C cut. The simulated data, (b),

also shows the peak around one for the three body annihilations and the almost flat distribution, (c), is from four body annihilations. I cut events with $\cos\theta_C < 0.95$.

Results of primary vertex cuts

Selection criterion	% passing
Exactly one kaon	98.7
Good primary vertex	91.8

Selection criterion	% of events passing		
	Real data	MC 4 body	MC 3 body
1C fit probability cut	61.7	7.4	82.5
Acolinearity cut	82.4	21.4	84.4

Using the figures in the table above and the missing mass distributions of figure 5.4, I can estimate the fraction of events accepted as golden which are in fact due to golden plus π^0 annihilations. I have fitted the missing mass distribution measured from the data (before the primary vertex cuts) with α_1 times the distribution from the three body annihilation Monte Carlo data plus α_2 times the distribution from the four body annihilation Monte Carlo data and determined the ratio α_1/α_2. This gives the fraction of the large eigentime data that is due to golden plus π^0 annihilations, which I find to be about 25 % with an error of a few percent. The fraction of the golden event sample that is due to golden plus π^0 annihilations is then

$$\frac{0.25 \times (0.07 \times 0.21)}{0.75 \times (0.83 \times 0.84) + 0.25 \times (0.07 \times 0.21)} \sim 0.007$$

i.e., less than one percent.

5.3.5 Secondary vertex position

- The secondary vertex must lie between PC2 and DC3.

Since it has been established already that neither secondary track has a hit in the PCs and that both have at least four transverse hits in the DCs the secondary vertex must lie between PC2 and DC3. This cut is to remove badly reconstructed vertices.

After P10, PC2 was not operational and for data taken during and after this period the cut was extended to

- The secondary vertex must lie between PC1 and DC3.

Selection criterion	% passing
Secondary vertex between PC2 and DC3 (P8)	98.0
Secondary vertex between PC1 and DC3 (P13)	99.0

5.3.6 Electron Identification

- Exactly one of the secondary tracks must be identified as an electron.

The identification of electrons was discussed in the previous chapter. While PC2 was operational the fraction of the IDL 4 data due to $\pi^+\pi^-$ decays was approximately 60% of what it was after PC2 was turned off. This difference is reflected in the number of events with identified secondary electrons before and after PC2 was switched off, and is discussed further in section 5.5.1.

Selection criterion	% passing
Exactly one secondary electron (P8)	8.3
Exactly one secondary electron (P13)	4.4

5.3.7 Rejection of background decays

- $\cos\theta_R > -0.97$, where θ_R is the opening angle of the secondary tracks in the rest frame of the neutral kaon.

- The probability returned from the 2C fit must be greater than 0.1.

As stated before, the presence of an electron as one of the decay products of a neutral kaon implies a semileptonic decay. In practice, however, there is a background of events where a pion has been wrongly identified as an electron. The background is due to $\pi^+\pi^-$ and $\pi^+\pi^-\pi^0$ decays, and I reduce this background by using the decay kinematics.

Muons which are identified as electrons are not a problem, since, for measuring Δm and $Re(\epsilon)$ the flavour of the lepton in the final state is unimportant. Muonic semileptonic decays are thus an addition to the signal.

Removal of $\pi^+\pi^-$ decays

Using the momentum of the neutral kaon from the 1C fit to the primary vertex we can boost the momenta of the secondary tracks into the neutral kaon rest frame. The secondary opening angle in that frame is denoted by θ_R. Two pion decays should have back-to-back secondaries in this frame, whereas the three body, semileptonic and $\pi^+\pi^-\pi^0$, decays can have any angle. Thus θ_R provides a way of distinguishing between three-body semileptonic decays and two-body $\pi^+\pi^-$ decays.

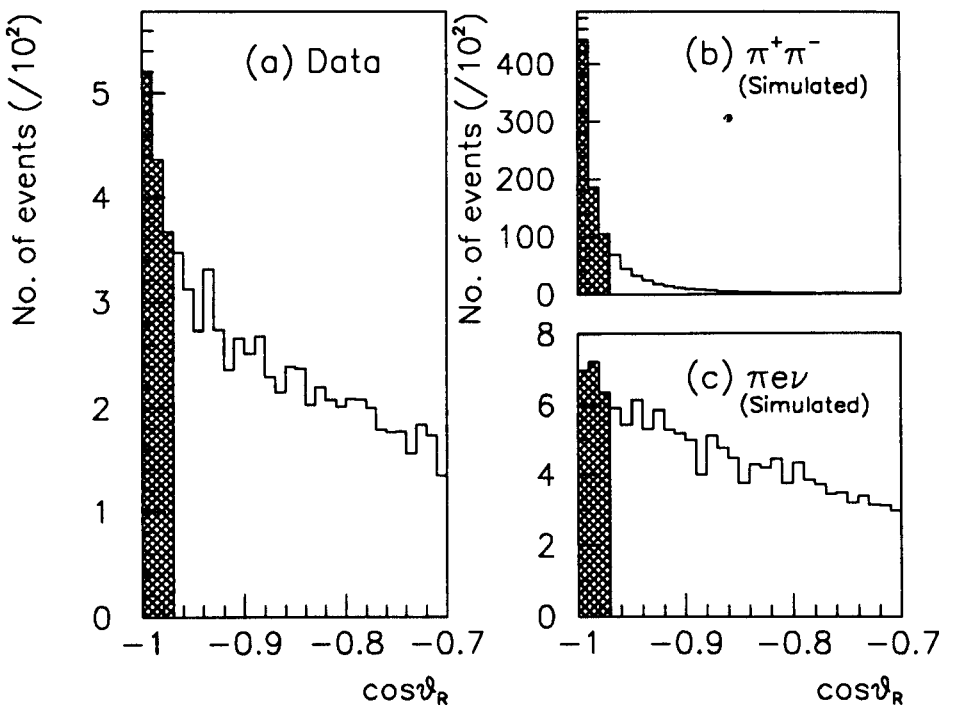

Figure 5.6: Distributions of the secondary opening angle in the neutral kaon rest frame.

Figures 5.6 (b) and (c) show the distributions of $\cos\theta_R$ for Monte Carlo data samples. The two body decays peak around 180° whereas the three body decays are distributed over the full range of $\cos\theta_R$. Figure 5.6 (a) shows the distribution of opening angles for those events which have an identified electron as one of the

secondaries. The small peak at -1 indicates the small number of two pion decays passing the electron identification criterion. Those events with $\cos\theta_R < -0.97$ are rejected. They are shown as the hatched regions.

Removal of $\pi^+\pi^-\pi^0$ decays

Three pion decays have a similar opening angle distribution to semileptonic decays and thus are not removed by the cut on $\cos\theta_R$. They differ from semileptonic decays in that all of the final state particles are massive. Consequently very little of the neutral kaon's mass energy becomes kinetic energy in the final state. The final state kinematics of three pion and semileptonic decays are thus different and the two decays can be separated by use of a constrained fit.

Taking as an event hypothesis $p\bar{p} \rightarrow \pi K K^0$ followed by $K^0 \rightarrow \pi e \nu$ there are six unknowns in the event: the three momenta of the neutral kaon and the neutrino. The constraint of four momentum conservation can be applied at each vertex thus giving eight constraints. Eight equations in six unknowns gives two dependent momentum vector components and thus the fit is a 2C fit.

The 2C probability distributions for three pion decays and $\pi e \nu$ decays are shown in figure 5.7. Histogram (a) shows the distribution for the events which have survived all previous cuts. There is a peak around zero probability. Histograms (b) and (c) show the distribution for three pion events and $\pi e \nu$ events as determined from Monte Carlo. The distribution for the semileptonic events is not flat but rises as the probability increases. This is partly a result of the cut on the 1C fit probability. It is also due to an over-estimate of the magnitude of the momentum errors for the short secondary tracks. However, the three pion background decays are heavily peaked around zero and can be reduced by a cut at 0.1 as shown. Note that very few two pion decays are removed by this cut. Semileptonic decays where the lepton is a muon also satisfy the 2C fit and it does not seem likely that the two different types of semileptonic decay will be separable by kinematics alone.

The 2C fit also gives an improved measure of the event eigentime as is shown in section 5.5.3

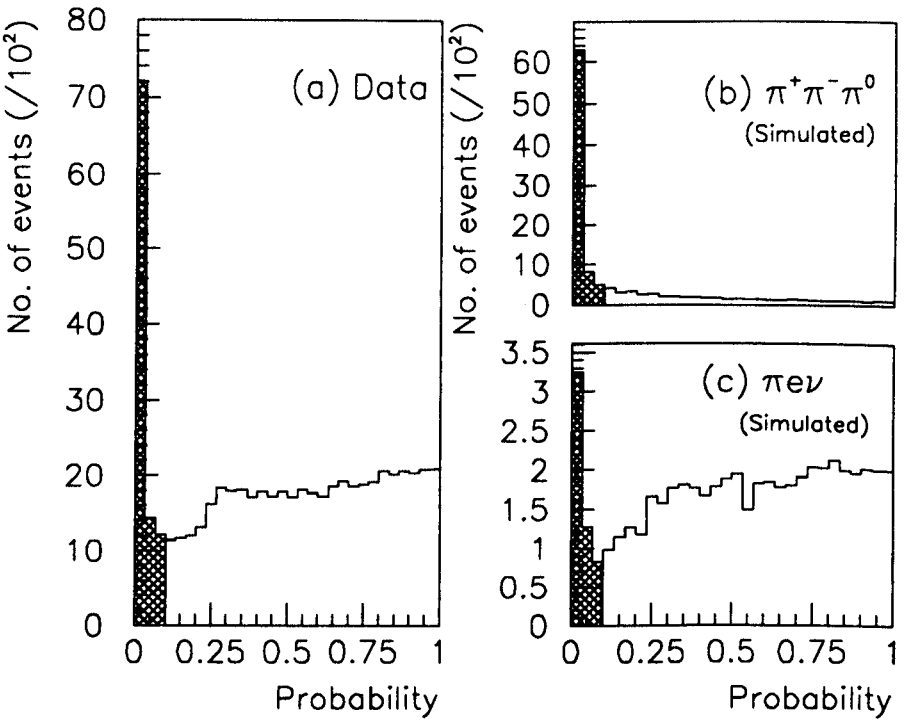

Figure 5.7: Probability distributions from the 2C fit to the whole event, assuming a $\pi e\nu$ hypothesis.

Results of background removal

The fractions of the different decay states passing these two cuts are shown below. The high percentage of real events passing indicates the low level of background present at this stage.

Selection criterion	% of real data passing	% of Monte Carlo decays passing			
		$\pi^+\pi^-$	$\pi^+\pi^-\pi^0$	$\pi e\nu$	$\pi\mu\nu$
$\cos\theta_R > -0.97$	91.7	33.1	93.8	96.0	91.4
2C fit probability cut	85.5	89.1	39.0	90.2	82.2
Combined cut	78.4	29.5	36.6	86.6	75.1

5.4 Small eigentime selection

5.4.1 Outline of selection criteria

The selection criteria used for small eigentime event selection are almost exactly the same as those for the large eigentime selection except for one main difference. There are in general four tracks originating from within the PCs and it is not a trivial matter to pair these off into primaries and secondaries. To do this I first identify a track which is a kaon, this track must be a primary. Secondly I take each of the other three tracks as electron candidates and count how many pass the electron selection criteria. I discard any event which does not have exactly one identified electron. The track which is identified as an electron is then taken as the first secondary track. Then there remain two tracks, one of which is a primary, the other a secondary. The only new feature of the small eigentime selection is how to decide which is which. After assigning roles to all tracks I check that the event is consistent with being golden, as opposed to golden plus π^0, and finally that it is consistent with being a semileptonic decay. As there are so few semileptonic decays in these data sets, their effect on the measurement of Δm is almost negligible. However they are in an interesting eigentime region and I include them for completeness. The selection criteria are outlined below:

- All tracks have at least four transverse hits in the PCs and DCs and at least two longitudinal hits.
- There is exactly one primary kaon.
- Exactly one track is identified as an electron.
- There is only one possible pairing of the remaining two tracks. An acceptable pairing must satisfy a number of criteria, described hereafter.
- $-0.9 < \cos\theta_O < 0.95$ for the secondary tracks
- The probability from the 1C fit is greater than 0.1.
- $\cos\theta_C > 0.53$.

EVENT IS GOLDEN

- $\cos\theta_R > -0.97$.
- The probability returned by the 2C fit to the event must be greater than 0.1.

EVENT IS A SEMILEPTONIC DECAY

The main problem with small eigentime data is the dominance of the two pion decays. As stated above if one percent of the two pion decays are identified as semileptonic then since they are two hundred times more common than the semileptonic decays in the first few τ_S the final event sample will be two thirds $\pi^+\pi^-$ decays. The level of background decays accepted in the final event sample is discussed in section 5.5.

Despite the problems associated with small eigentime selection these events are important in searching for non-Standard Model decays.

5.4.2 Space point information and vertex quality

This cut consists of exactly the same criteria as for large eigentime selection.

Selection criterion	% passing
All tracks have sufficient XY and Z hits	99.3

5.4.3 Particle identification

- There is exactly one primary kaon.
- Exactly one track is identified as an electron.

Note here that the fraction of events failing the first cut is higher than for the large eigentime data. This is because of annihilations such as $p\bar{p} \rightarrow K^+K^-X^0$, i.e. multiple kaons. These are suppressed in the large eigentime data by the trigger demand for two secondary tracks (IDL 4).

The value of 1.4% for the number of events containing an electron track is due mainly to pion contamination which occurs at around the 1% level.

Selection criterion	% passing
There is exactly one kaon	89.7
Exactly one track is an electron	1.4

5.4.4 Primary and secondary track pairing

- There is only one possible pairing of the remaining two (unidentified) tracks.

Given that the track identified as a kaon is a primary track, and assuming that the electron track is a secondary, it remains to determine which of the remaining two tracks belongs to the primary vertex and which belongs to the secondary vertex.

If the charges of the kaon and the electron tracks are opposite then there is only one possible combination of tracks which conserves charge at both vertices. However if the kaon and the electron charges are the same then there are two possible pairings. This results in a different selection efficiency for events with like sign kaon and electron tracks, and events with unlike sign kaon and electron tracks.

Selecting events for which there is only one possible pairing thus leads to a reduced efficiency for like sign events. It does not however lead to zero acceptance for like sign events, as a number of criteria other than charge conservation must be met for a track pairing to be considered acceptable. These criteria are

- The two primary tracks must intersect and form a vertex, as must the two secondaries.
- The total charge at both the primary and secondary vertices must be zero.
- The primary vertex must be radially within 1 cm of the centre of the target.
- The secondary vertex must be at least 3 cm radially from the target centre.

From Monte Carlo the fractions of semileptonic events passing this cut are

Charge pairing	% passing
K^+e^- and K^-e^+	47 ± 1
K^+e^+ and K^-e^-	45 ± 1

Though this is not a large difference and its exact value depends on the cuts, it cannot be removed altogether and must be corrected for. The figure for the real data is as below.

Selection criterion	% passing
Only one pairing is possible	46.1

There exists the possibilty in the later stages of the trigger, to cut online on the eigentime of the event. Cutting out events with eigentimes less than $1\tau_S$, i.e. on a vertex separation of around 2 cm, should improve the fraction of events passing this type of cut.

5.4.5 Identification of event as golden

- $-0.9 < \cos\theta_O < 0.95$ for the secondary tracks
- Probability from the 1C fit is greater than 0.1.
- $\cos\theta_C > 0.53$

Selection criterion	% passing
$-0.9 < \cos\theta_O < 0.95$	75.1
1C fit probability > 0.1	22.2
$\cos\theta_C > 0.53$	34.8

The small fraction of events passing the 1C fit shows that there is a large background from annihilations to K^+K^- states. The cut on the angle between the neutral kaon momentum vector and the vertex separation vector has been opened right out. The small separation of the two vertices means that a small error in the position of one or both of the vertices leads to a big error in the colinearity angle. This is particularly true for vertices with large opening angles, where the uncertainty on the position of the vertex is larger.

5.4.6 Rejection of non-semileptonic decays

- The opening angle of the secondary tracks in the rest frame of the neutral kaon must exceed -0.97.
- The probability returned by the 2C fit to the event must be greater than 0.1.

Selection criterion	% passing
$\cos\theta_R > -0.97$	75.1
2C fit probability > 0.1	22.2

5.5 Semileptonic acceptance and backgrounds

5.5.1 Selection statistics

The aim of these selection criteria was to select a sample of semileptonic decays with as small a background from pionic neutral kaon decays as possible. The statistics of the large eigentime selection for the different running periods are shown below. The first column shows the number of events read from the miniDST cassettes. The second column is the number of events that are identified as golden events. The fourth column is the number of events which pass all the cuts and are thus accepted as semileptonic decays.

Data sample	No. of raw events/10^3	Golden events		Semileptonic events	
		Number	% of raw	Number	% of golden
P8M1T433	284	70548	24.8	4488	6.4
P8M2T433	244	61360	25.1	3832	6.2
P9M1T433	442	94851	21.4	6042	6.4
P9M2T433	369	72356	19.6	4626	6.3
P10T433	143	35796	25.0	1327	3.7
P11M1T423	283	78648	27.8	2927	3.7
P11M2T423	274	77844	28.4	2843	3.6
P12M1T423	340	88725	26.1	3339	3.8
P12M2T423	334	87062	26.1	3341	3.8
P13M1T423	857	189630	22.1	5939	3.1
P13M2T423	736	161922	22.0	4782	3.0

The most obvious trend in these figures is the fall off in later periods of the percentage of golden events which are selected as semileptonic decays. Before P10 the figure is around 6.3% whereas afterwards it is substantially less. There are two factors contributing to this. The outer proportional chamber was non-operational from P10 onwards leading to increased acceptance at low eigentimes. This resulted in an increased fraction of the golden events being $\pi^+\pi^-$ decays. With PC2 operational 54.2% of the golden events should be semileptonic decays. With PC2 turned off this falls to 31.1%, i.e. if 6.3% of golden data is accepted as semileptonic before P10 around $6.3 \times 31/54 \sim 3.6\%$ should be accepted during and after P10. This is in agreement with the P10 statistics. The second point is that the fraction of golden events identified as semileptonic after P10 decreases in the later running periods. This is due to a fall off in electron identification efficiency, as shown below

Running period	Fraction of golden events with an $e^{\pm}$
P11	6.1 %
P12	5.3 %
P13	4.1 %

This is the result of some of the Čerenkov elements being damaged by heat and subsequently leaking during and after P12. The slow leakage of the liquid radiator left air spaces in the tubes thus giving decreased light output and reduced efficiency.

The fraction of events on the miniDSTs which are accepted as golden events varies from period to period. The early periods, P8 and P9, were particularly subject to beam alignment problems. Period 9 in particular has a low percentage of golden events, with the reverse field configuration (M2) being worse than the normal field configuration. This field dependence is symptomatic of beam misalignment, as a non-paraxial beam will be deflected differently according to the magnetic field orientation.

The low fraction of events which pass as golden in P13 can be attributed to the inefficient Čerenkov elements. Since a kaon is identified online by an $S\overline{C}S$ signal, i.e. low light output in the Čerenkov , a reduced Čerenkov efficiency leads to an increase in the number of pions faking the kaon signal. However the presence of a kaon is not sufficient for an event to pass the trigger. There must also be a pair of secondary tracks originating outside the PCs. In events where the kaon signal is faked by a pion these tracks can be due to a gamma conversion. The increased presence of gamma conversions in the later periods can be seen from the figures below.

Selection criteria	% passing cut			
	P8 & P9	P11	P12	P13
Secondaries $\neq \gamma-$conversion	85.9	85.6	81.3	73.2
1C Probability > 0.1	61.7	57.0	57.4	54.5

These events also fail the primary vertex kinematic fit.

The small eigentime selection yields very few semileptonic decays because of the predominance of $\pi^+\pi^-$ decays. The results for the different running periods are shown below.

Data sample	Number of raw events	Events with an $e^{\pm}$		Semileptonic events	
		Number	% of raw	Number	% of $e^{\pm}$ events
P8M1T433	105 579	1 247	1.18	12	0.96
P9M1T233	310 776	5 961	1.92	42	0.70
P9M2T233	286 146	5 528	1.93	51	0.92
P11M1T223	274 718	5 176	1.88	24	0.46
P11M2T223	73 170	1 508	2.06	9	0.60
P12M1T223	399 696	5 912	1.48	33	0.56
P12M2T223	306 389	5 088	1.66	27	0.53
P13M1T223	395 078	5 502	1.39	34	0.62

The small eigentime selection results in the grand total of 232 selected semileptonic events, most of which are below $3\tau_S$ and a large fraction of which are in reality $\pi^+\pi^-$ decays. This should be compared to the 44K events accepted from the large eigentime data. The background levels are discussed further in the next section.

5.5.2 Monte Carlo determination of relative acceptances

The presence of background decays in the semileptonic sample is unavoidable at some level, especially at small eigentimes where it is a substantial fraction of the selected events. To correct for the presence of background decays the relative number of semileptonic decays and background pionic decays must be determined.

To do this it is necessary to determine the relative acceptance of the analysis to background and semileptonic decays. I do this by passing simulated events of different decay final states through my analysis program. The simulated events are treated exactly the same as real events apart from at the electron selection stage as already outlined.

Acceptance, here, is defined as the number of events passing the semileptonic selection criteria divided by the number of events input to the program. Thus it does not include trigger acceptance and data filtering acceptance. Only the relative acceptance of pionic decays to semileptonic decays is needed and since the trigger and data filtering acceptances are independent of the final decay state (so long as there are two charged tracks) these acceptances cancel out. The measured acceptances are shown in figure 5.8. The values are in the table below.

Large eigentime acceptance	
Decay channel	Acceptance
$\pi e \nu$	$(6.8 \pm 0.1) \times 10^{-2}$
$\pi \mu \nu$	$(4.41 \pm 0.24) \times 10^{-3}$
$\pi^+\pi^-$	$(4.10 \pm 0.50) \times 10^{-4}$
$\pi^+\pi^-\pi^0$	$(7.43 \pm 1.47) \times 10^{-4}$

To accurately simulate the different states of the detector, i.e. the decreasing efficiency of the Čerenkov elements, I have taken a weighted average of $P(e|e)$ and $P(e|\pi)$, weighted proportional to the number of events accepted from each running period. This is only possible because these quantities were effectively constantly measured during the data taking. The weights used are:

Running Period	P8	P9	P10	P11	P12	P13
Weight	0.13	0.164	0.035	0.154	0.173	0.345

To determine an upper limit to the amount of background accepted by my analysis I set $P(e|\pi) = 0.015$, i.e. 1.5% chance of identifying a pion as an electron, for all momenta below 260 MeV/c. This almost doubled the number of pionic decays passing the selection.

At the time of writing there is insufficient Monte Carlo data available to determine accurately the eigentime dependence of the acceptances. However in the region below $20\tau_S$, the important region for determining Δm,the acceptances are consistent with being flat as can be seen in figure 5.8. The actual contamination from pionic decays is determined by the product of their acceptance and the actual rate of decays, thus the actual level of contamination is a function of the eigentime. This is discussed in the next chapter.

Earlier in this chapter I estimated that around 0.7 % of the events passing as golden events were actually golden plus π^0 events. Those golden plus π^0 events which pass the event selection have neutral pions with very low momenta. The error in the eigentime for these events is biased low, but is less than the magnitude of the eigentime resolution (see next section). Their effect on the analysis is negligible.

The small eigentime data in the region below $3\tau_S$ is effectively independent of the large eigentime data. The large eigentime data contains no decays below $3\tau_S$, and the decays above $3\tau_S$ from the small eigentime data are insignificant compared to

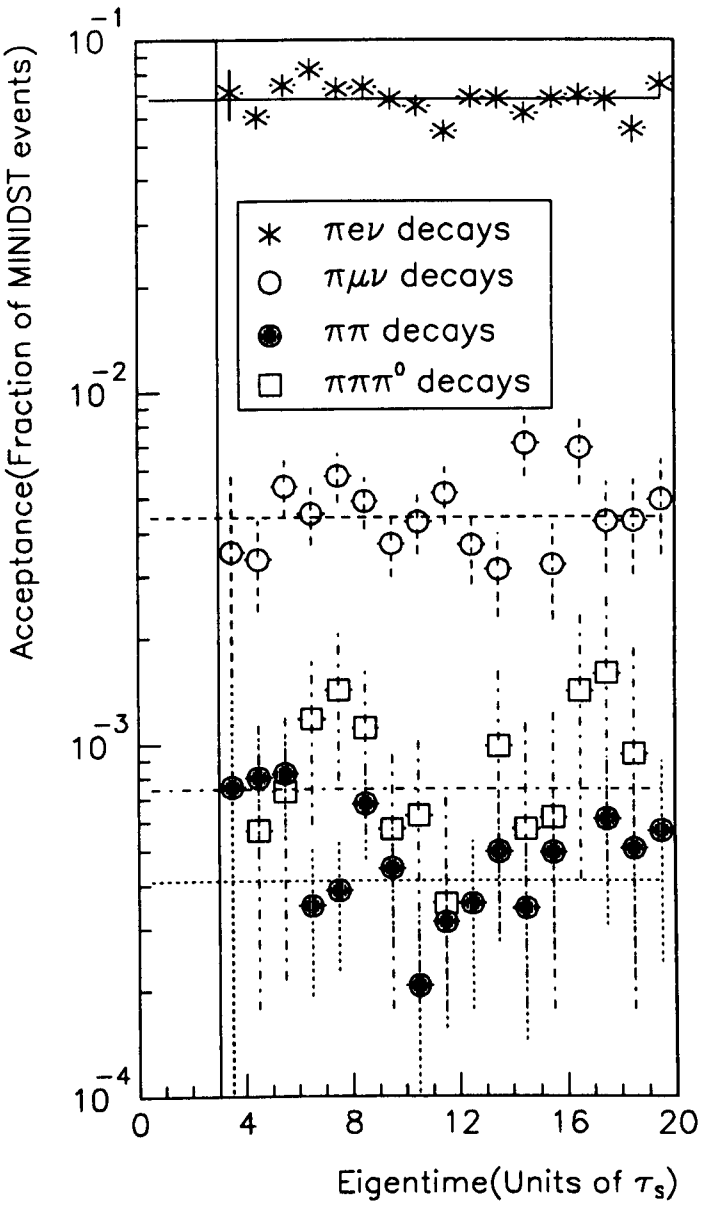

Figure 5.8: Acceptance of semileptonic and pionic decays for large eigentime data.

the much larger numbers of decays from the large eigentime data. Bearing this in mind it is possible to determine the acceptances in the region below $3\tau_S$ in a similar manner. Simulated events are passed through the small eigentime analysis program and the number passing determine the acceptance. The small amount of simulated data available limits the precision of this determination.

Small eigentime acceptance	
Decay channel	Acceptance
$\pi e \nu$	$(2.05 \pm 0.14) \times 10^{-2}$
$\pi \mu \nu$	$(1.1 \pm 0.3) \times 10^{-3}$
$\pi^+\pi^-$	$(2.9 \pm 1.3) \times 10^{-4}$
$\pi^+\pi^-\pi^0$	$(1 \pm 1) \times 10^{-4}$

NOTE: In the following chapter I refer to the acceptance measurements for the final state f by Acceptance(f). For example, for the small eigentime data

$$\text{Acceptance}(\pi^{\pm}e^{\mp}\nu) = (2.05 \pm 0.14) \times 10^{-2}$$

The small eigentime acceptance is averaged over the decay region $0 \rightarrow 3\tau_S$, except for the three pion data. This channel had only one event passing in the first six τ_S and is thus averaged over that region. These figures imply that of the events selected as semileptonic in the region $0 \rightarrow 3\tau_S$ around 80% are actually $\pi^+\pi^-$ decays.

5.5.3 Eigentime resolution

I have measured the eigentime resolution as a function of eigentime from the Monte Carlo. It is shown in figure 5.9. Each eigentime bin has been fitted with a gaussian, and the resolution at a particular eigentime is given by the standard deviation of the fitted curve. The plot also shows the eigentime resolution that would be obtained without the use of the constrained fit programs. This is clearly much worse.

Below $3\tau_S$ the resolution is constant, and above this I have fitted the points with a second order polynomial. Thus the resolution as a function of eigentime is parametrized by

$$\sigma(t) = \left\{ \begin{array}{ll} 0.15 & t < 3\tau_S \\ 0.254 - 0.0385\,t + 0.00518\,t^2 & t \geq 3\tau_S \end{array} \right\} \text{(Units of } \tau_S\text{)}$$

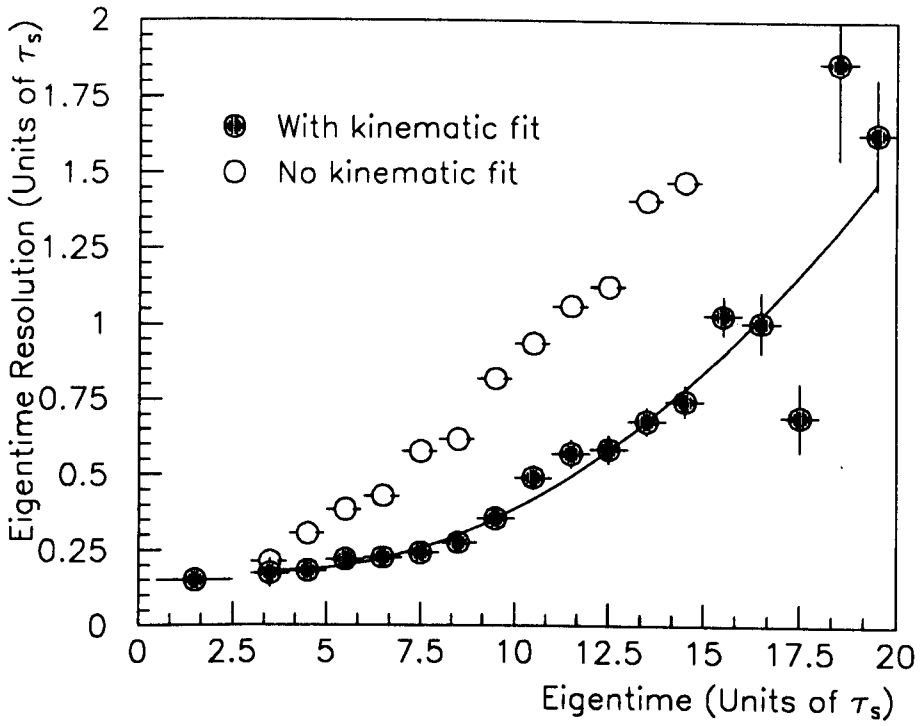

Figure 5.9: Eigentime resolution as a function of eigentime.

At small eigentimes, i.e. less than 10 τ_S, the most important region for the measurement of semileptonic asymmetries, the resolution is less than $0.3\tau_S$. At eigentimes past $12\tau_S$ the resolution ceases to be important as the decay distributions are practically flat. The effect of eigentime resolution on the determination of Δm is discussed in the next chapter.

5.6 Summary

A total of 4.3×10^6 events were read from the large eigentime miniDSTs of which 43 486 events were accepted into the final event samples. From the small eigentime data: 2.1×10^6 events were read from miniDST and 232 were accepted as semileptonic decays.

The figures for the percentages of events passing each of the selection criteria are collected together below.

Large eigentime acceptance	
Selection criterion	% passing
≥ 4 $R\phi$ hits for primaries	99.8
≥ 2 Z hits for primaries	95.9
≥ 4 $R\phi$ hits for secondaries	83.4
≥ 2 Z hits for secondaries	87.6
$-0.9 < \cos\theta_O < 0.95$	83.6
Good secondary vertex	93.0
Exactly one Kaon	98.7
Good primary vertex	91.8
1C fit probability cut	61.7
Acolinearity cut	82.4
Secondary vertex between PC2 and DC3 †	98.0
Exactly one secondary electron ‡	8.3
$\cos\theta_R > -0.97$	91.7
2C fit probability cut	85.5

† For data taken after P10 the cut was extended to include the region between PC1 and PC2. The percentage of events passing rose to 99 %.

‡ This figure is for Period 8. See section 5.5.1 for the variation of this figure with period number.

Small eigentime acceptance	
Selection criterion	% passing
All tracks have sufficient XY and Z hits	99.3
There is exactly one kaon	89.7
Exactly one track is an electron	1.4
Only one pairing is possible	46.1
$-0.9 < \cos\theta_O < 0.95$	75.1
1C fit probability > 0.1	22.2
$\cos\theta_C > 0.53$	34.8
$\cos\theta_R > -0.97$	75.1
2C fit probability > 0.1	22.2

The total number of events in the four subsets of the final data sample are

Event sample	No. of events
K^+e^+	11 933
K^+e^-	11 520
K^-e^+	9621
K^-e^-	10 690

Chapter 6

Analysis

6.1 Introduction

The aim of this analysis is to determine a value of the K_L-K_S mass difference using the sample of semileptonic events whose selection has been described previously. This final data sample consists of the four data sets K^+e^+, K^+e^-, K^-e^+ and K^-e^-. As was discussed in section 1.2 the events can be further grouped into two sets; those where the neutral kaon has the same strangeness at both primary and secondary vertices, $\Delta S = 0$ events, and those where the strangeness has changed, $\Delta S = \pm 2$ events.

$$\begin{aligned} N(\Delta S = 0) &= N(K^-e^+) + N(K^+e^-) \\ N(\Delta S = \pm 2) &= N(K^+e^+) + N(K^-e^-) \end{aligned}$$

These can be combined to give an eigentime dependent asymmetry in terms of the quantities γ_S, γ_L and Δm only[†]

$$A_0 = \frac{N(\Delta S = 0) - N(\Delta S = \pm 2)}{N(\Delta S = 0) + N(\Delta S = \pm 2)}$$

which (using the expressions for the rates from Appendix B) gives

$$A_0(t) = 2\frac{e^{-\frac{1}{2}(\gamma_S - \gamma_L)t}\cos \Delta m t}{1 + e^{-(\gamma_S - \gamma_L)t}}$$

[†]Since I measure time in units of τ_S, when I refer to the mass difference I mean $\Delta m/\gamma_S$.

Using an asymmetry of this type alleviates the need to know the eigentime dependence of the detector acceptance. However the detection efficiencies turn out to depend on the event sample, e.g. the K^+e^+ and K^-e^+ detection efficiencies are different: $\epsilon(K^+e^+) \neq \epsilon(K^-e^+)$. Thus an asymmetry formed from the measured decay distributions will not look like A_0 unless a correction is made for these differences. The sizes of these corrections, or normalisations, are determined from the data. They are discussed in the next section and again in section 6.3.

The presence of background (non-semileptonic) decays in the final event sample must also be allowed for, as this will change the shape of the measured asymmetry. Background decays consist of $\pi^+\pi^-$ and $\pi^+\pi^-\pi^0$ final states. The level of background present in the final event sample, i.e. the fraction of events in the final sample that are background decays is determined from the acceptances presented in the last chapter and the decay rates of appendix B.

To emphasise that an asymmetry formed from the data is different from an idealized asymmetry such as $A_0(t)$, I define, in section 6.2, a new asymmetry $A_{\Delta m}(t)$.The relationship of this asymmetry to A_0 is discussed in that section and again in section 6.3 where background decays are considered. The determination of the mass difference from the shape of this asymmetry is discussed in section 6.5 and a value of $\Delta m/\gamma_S$ presented. Systematic uncertainties in the measurement are discussed in section 6.6.

6.2 Normalisation

If, initially I Ignore the presence of background, the measured decay distributions, $N(E)_M$, are related to the real distributions, $N(E)$, by

$$N(E)_M = \epsilon(E)N(E) \tag{6.1}$$

Here, $N(E)$ represents all of the events of type E that occur in the detector, irrespective of whether they are triggered upon or not, whereas $N(E)_M$ represents those events in the final event sample. Thus the efficiency, $\epsilon(E)$, is a combination of detector and trigger efficiency, and also of the efficiency of offline event selection. As pointed out in the introduction to this chapter, a complication arises in that $\epsilon(E)$ depends

upon the event sample. This can be clearly seen in figure 6.1, as the K^+e^- and K^-e^+ rates should be the same, and the rates of K^+e^+ and K^-e^- should differ by less than one percent. The main reason for this is the difference in the cross sections for

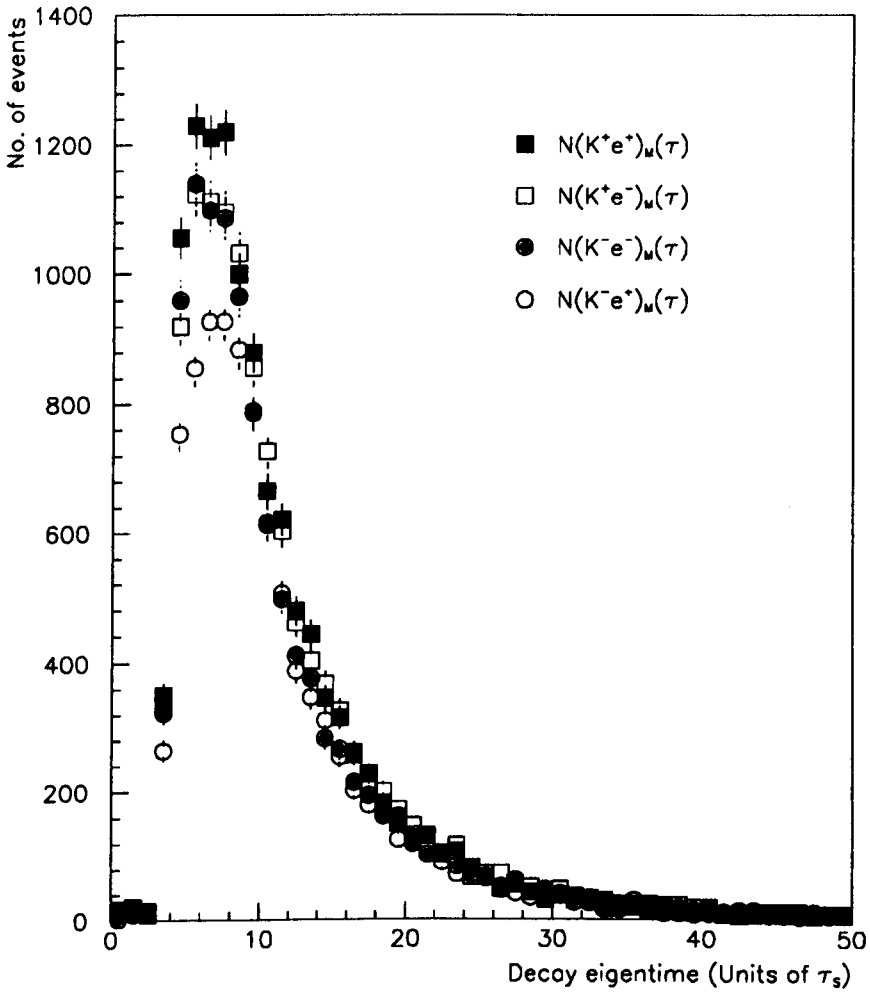

Figure 6.1: Eigentime distributions of the four sets of semileptonic decays in the final selected event sample.

K^+ and K^- interactions with the matter of the detector. Below 1 GeV, negatively charged kaons have a higher inelastic cross section and are thus less likely to pass through the PID giving a trigger. I assume hereafter that the difference in detection efficiency for the different event samples can be factored into two independent parts.

The first factor for the charged kaon detection and the second factor for the final state detection, e.g.

$$\epsilon(K^+e^+) \rightarrow \epsilon(K^+)\epsilon(e^+)$$

where $\epsilon(e^+)$ means $\epsilon(\pi^-e^+\nu)$.

Factoring the detection efficiency in this way it also turns out that $\epsilon(e^+) \neq \epsilon(e^-)$. According to section 4.5 $P(e^+|e^+)$ and $P(e^-|e^-)$ differ by less than one percent, so this difference is not directly due to the electron selection efficiency. However the selection of a semileptonic decay requires the detection of a pion as well as a lepton and this may be the origin of the difference. The important point is that the magnitude of these differences can be determined from the data and correction factors calculated.

For the four sets of semileptonic events, we have

$$\begin{aligned} N(K^+e^+)_M &= \epsilon(K^+)\epsilon(e^+)N(K^+e^+) \\ N(K^+e^-)_M &= \epsilon(K^+)\epsilon(e^-)N(K^+e^-) \\ N(K^-e^+)_M &= \epsilon(K^-)\epsilon(e^+)N(K^-e^+) \\ N(K^-e^-)_M &= \epsilon(K^-)\epsilon(e^-)N(K^-e^-) \end{aligned}$$

Since the mass difference will be determined from an asymmetry, the absolute magnitudes of the efficiencies are unimportant and it is necessary to determine only the ratios $\epsilon(K^+)/\epsilon(K^-)$ and $\epsilon(e^+)/\epsilon(e^-)$.

As a consequence of CPT invariance the rates $N(K^-e^+)$ and $N(K^+e^-)$ are identical. Thus taking the ratio of $N(K^-e^+)_M$ and $N(K^+e^-)_M$ should give a value equal to

$$\frac{N(K^-e^+)_M}{N(K^+e^-)_M} \equiv \frac{\epsilon(K^-)\epsilon(e^+)}{\epsilon(K^+)\epsilon(e^-)}$$

The rates $N(K^-e^-)$ and $N(K^+e^+)$ are not similarly constrained by CPT invariance, and in fact differ by a factor of the order of $Re(\epsilon)$. The ratio of the measured rates gives

$$\frac{N(K^-e^-)_M}{N(K^+e^+)_M} \equiv \frac{\epsilon(K^-)\epsilon(e^-)(1-4Re(\epsilon))}{\epsilon(K^+)\epsilon(e^+)(1+4Re(\epsilon))}$$

Combining these two ratios and using the fact that $Re(\epsilon)$ is small we have

$$\eta = \frac{\epsilon(K^+)}{\epsilon(K^-)} = \left(\frac{N(K^+e^+)_M N(K^+e^-)_M}{N(K^-e^+)_M N(K^-e^-)_M}\right)^{\frac{1}{2}} (1-4Re(\epsilon))$$

$$\zeta = \frac{\epsilon(e^+)}{\epsilon(e^-)} = \left(\frac{N(K^{*+}e^+)_M N(K^{*-}e^+)_M}{N(K^{*+}e^-)_M N(K^{*-}e^-)_M} \right)^{\frac{1}{2}} (1 - 4Re(\epsilon)) \qquad (6.2)$$

i.e. a determination of the ratios of the selection efficiencies from the data. The ratios are plotted in figure 6.2, where I have fitted them both with constant functions, giving

$$\eta = 1.139 \pm 0.011 \quad (\chi^2_{df} = 1.33)$$
$$\zeta = 0.951 \pm 0.009 \quad (\chi^2_{df} = 1.14)$$

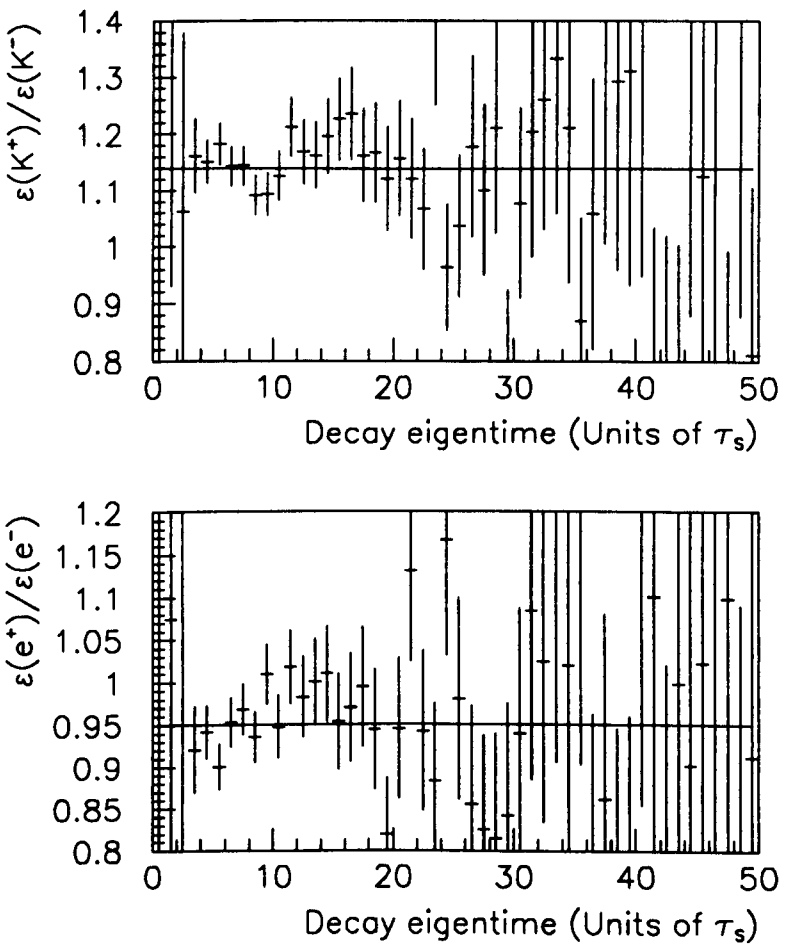

Figure 6.2: Normalisation factors η and ζ plotted versus eigentime.

Since I am interested in an eigentime dependent asymmetry I have plotted the normalisation factors versus eigentime to see if there is any systematic dependence. The

kaon normalisation, η, shows no systematic trend over any of the range. However the case is not quite so clear for the final state normalisation. Here there is a hint of a trend from $3\tau_S$ to $15\tau_S$ for ζ to increase, though the difference of the data from the fitted value is nowhere more than 5% and the statistics are too low to make a definite statement. Hereafter I take both normalisations to be independent of eigentime. The effect of making time dependent normalisations is considered in section 6.6.

Using the values of η and ζ determined above, I correct all of the data relative to the K^+e^+ sample. For example, since $N(K^+e^-)_M = \epsilon(K^+)\epsilon(e^-)N(K^+e^-)$ then

$$\frac{\epsilon(e^+)}{\epsilon(e^-)}N(K^+e^-)_M = \epsilon(K^+)\epsilon(e^+)N(K^+e^-) = N(K^+e^-)_C$$

where corrected quantities are represented by a subscript C. The other three rates are corrected similarly

$$\begin{aligned} N(K^+e^+)_C &= N(K^+e^+)_M \\ N(K^+e^-)_C &= \zeta N(K^+e^-)_M \\ N(K^-e^+)_C &= \eta N(K^-e^+)_M \\ N(K^-e^-)_C &= \eta\zeta N(K^-e^-)_M \end{aligned}$$

so that $N(E)_C = \epsilon(K^+)\epsilon(e^+)N(E)$ for all four data sets. With these corrected quantities I form the asymmetry

$$A_{\Delta m} = \frac{N(\Delta S = 0)_C - N(\Delta S = \pm 2)_C}{N(\Delta S = 0)_C + N(\Delta S = \pm 2)_C} \tag{6.3}$$

so that the factor $\epsilon(K^+)\epsilon(e^+)$ cancels out. Note that this asymmetry is denoted $A_{\Delta m}$ to emphasise that it is not the same as A_0. $A_{\Delta m}$ is formed from the measured distributions which contain background events, whereas A_0 is an idealised asymmetry. Only in the absence of background and with the normalisation parameters exactly determined will A_0 and $A_{\Delta m}$ be the same.

Since the precision of the determination of η and ζ is limited at least by finite statistics, it is important to consider the effect of small errors in the normalisation parameters. If the normalisation factor for the data subset E is α, then an error $\delta\alpha$ gives an error $\delta N(E)_C$ equal to

$$\delta N(E)_C = \frac{\delta\alpha}{\alpha}N(E)_C$$

and thus

$$N(\Delta S = 0)_C = \left(1 + \frac{\delta\eta}{\eta}\right) N(K^-e^+) + \left(1 + \frac{\delta\zeta}{\zeta}\right) N(K^+e^-)$$
$$N(\Delta S = 2)_C = N(K^+e^+) + \left(1 + \frac{\delta\eta}{\eta}\right)\left(1 + \frac{\delta\zeta}{\zeta}\right) N(K^-e^-)$$

where I am still assuming the absence of background and have dropped the factor $\epsilon(K^+)\epsilon(e^+)$. With a little bit of algebra and substituting in explicit functions for the decay rates, the asymmetry can be rearranged to give

$$A_{\Delta M}(t) = A_0(t) + \delta_N(1 - A_0(t)^2)$$

where the error term, δ_N, is given by

$$\delta_N = \frac{1}{2}\frac{\delta\eta}{\eta}\frac{\delta\zeta}{\zeta} + \frac{5}{4}\left(\frac{\delta\zeta}{\zeta} + \frac{\delta\eta}{\eta}\right)^2 + \frac{1}{4}\frac{\delta\eta}{\eta}\frac{\delta\zeta}{\zeta}\left(\frac{\delta\eta}{\eta} + \frac{\delta\zeta}{\zeta}\right) - Re(\epsilon)\left(\frac{\delta\eta}{\eta} + \frac{\delta\zeta}{\zeta} + \frac{\delta\eta}{\eta}\frac{\delta\zeta}{\zeta}\right)$$

Using the statistical errors on η and ζ gives $\delta_N = 5 \times 10^{-4}$, corresponding to a tiny constant offset to the asymmetry (apart from close to $t = 0$ where $A_0 \sim 1$ and the offset goes to zero) and showing that the asymmetry is insensitive to errors in the normalisation parameters at this level of precision.

A further correction must be made to the data below $3\tau_S$, due to the difference in the selection efficiency for like sign and unlike sign small eigentime events. In section 5.4 I found

$$\frac{\epsilon(\text{Like sign})}{\epsilon(\text{Unlike sign})} = \frac{\epsilon(\Delta S = \pm 2)}{\epsilon(\Delta S = 0)} = 0.96 \pm 0.04$$

and thus $N(\Delta S = \pm 2)_C$ is further corrected by

$$N(\Delta S = \pm 2)_C \rightarrow (0.96)^{-1} N(\Delta S = \pm 2)_C \text{ for } t < 3\tau_S$$

For the present data sets, with very little small eigentime data, this has no observable effect.

6.3 Effect of background

So far I have ignored the presence of background decays in the semileptonic event samples. The presence of background means that equation 6.1 is no longer valid and

instead must be replaced by a more general summation over signal and background

$$N(E)_M = \epsilon(E)N(E) + \sum_{BG} \epsilon(E|BG)N(BG)$$

where $\epsilon(E|BG)$ represents the probability for a non-semileptonic decay of type BG to be accepted as an event of type E, and as before $\epsilon(E)$ (shorthand for $\epsilon(E|E)$) is the semileptonic selection efficiency. The background decays consist of two and three pion final states where one of the pions has been mistaken for an electron. Thus, for example, considering the K^+e^- data set

$$N(K^-e^+)_M = \epsilon(K^-)\left(\overbrace{\epsilon(e^+|e^+)N(K^-e^+) + \epsilon(e^+|\mu^+)N(K^-\mu^+)}^{\text{SIGNAL}}\right.$$
$$\left. + \underbrace{\epsilon(e^+|\pi^+\pi^-)N(K^-\pi^+\pi^-) + \epsilon(e^+|\pi^+\pi^-\pi^0)N(K^-\pi^+\pi^-\pi^0)}_{\text{BACKGROUND}}\right) \qquad (6.4)$$

where $\epsilon(K^-e^+|K^-\pi^+\pi^-)$ represents the probability for an event with a primary K^- and a $\pi^+\pi^-$ final state to be accepted as a K^-e^+ event, and is factored into $\epsilon(K^-)\epsilon(e^+|\pi^+\pi^-)$. I have also introduced the small contribution to the signal expected from semileptonic decays to muons. Appealing to lepton universality, i.e. that $N(K^\pm e^\pm) \propto N(K^\pm\mu^\pm)$, the signal part of this expression can be further factored by defining

$$\epsilon(l^+|l^+) = \epsilon(e^+|e^+)\left(1 + \frac{\epsilon(e^+|\mu^+)}{\epsilon(e^+|e^+)}\frac{BR(K_L \to \pi e\nu)}{BR(K_L \to \pi\mu\nu)}\right)$$

and $\epsilon(l^-|l^-)$ similarly. The above expression for $N(K^-e^+)_M$ can now be written

$$N(K^-e^+)_M = \epsilon(K^-)\epsilon(e^+)\left(\frac{\epsilon(l^+|l^+)}{\epsilon(e^+|e^+)}N(K^-e^+)\right.$$
$$\left. + \frac{\epsilon(e^+|\pi^+\pi^-)}{\epsilon(e^+)}N(K^-\pi^+\pi^-) + \frac{\epsilon(e^+|\pi^+\pi^-\pi^0)}{\epsilon(e^+)}N(K^-\pi^+\pi^-\pi^0)\right) \qquad (6.5)$$

Since the purpose of the normalisations is to remove the factors $\epsilon(K^-)\epsilon(^+)$ etc., I work hereafter with the ratios $\frac{\epsilon(e^+|f)}{\epsilon(e^+)}$ and $\frac{\epsilon(e^-|f)}{\epsilon(e^-)}$, denoted[†] by ϵ_f^+ and ϵ_f^-. These parameters are determined from the acceptances presented in the previous chapter

[†]In order to avoid a forest of indices I drop the $\pm$ signs in the subscripts, e.g. $\epsilon^+_{\pi^+\pi^-} \to \epsilon^+_{\pi\pi}$.

but since these acceptance are averages over all semileptonic final states, I cannot derive ϵ_f^+ and ϵ_f^- separately. Instead I assume $\epsilon_f^+ = \epsilon_f^-$ and then allow for possible differences between ϵ_f^+ and ϵ_f^- in the systematic uncertainty of the mass measurement.

I take nominal values for ϵ_f^+ and ϵ_f^- from

$$\epsilon_f^+ = \epsilon_f^- = \frac{\epsilon(e^+|f) + \epsilon(e^-|f)}{\epsilon(e^+) + \epsilon(e^-)}$$

Now, from the definition of acceptance given in section 5.5.1

$$\begin{aligned} \text{Acceptance}(\pi^+\pi^-) &= \frac{\epsilon(e^+|\pi^+\pi^-)N(\pi^+\pi^-) + \epsilon(e^-|\pi^+\pi^-)N(\pi^+\pi^-)}{N(\pi^+\pi^-)} \\ &= \epsilon(e^+|\pi^+\pi^-) + \epsilon(e^-|\pi^+\pi^-) \end{aligned}$$

whereas

$$\begin{aligned} \text{Acceptance}(\pi^\pm e^\mp \nu) &= \frac{\epsilon(e^+|e^+)N(\pi^- e^+\nu) + \epsilon(e^-|e^-)N(\pi^+ e^-\bar{\nu})}{N(\pi^- e^+\nu) + N(\pi^+ e^-\bar{\nu})} \\ &= \frac{1}{2}\left(\epsilon(e^+|e^+) + \epsilon(e^-|e^-)\right) \end{aligned}$$

thus

$$\epsilon_{\pi\pi}^+ = \epsilon_{\pi\pi}^- = \frac{1}{2}\frac{\text{Acceptance}(\pi^+\pi^-)}{\text{Acceptance}(\pi^\pm e^\mp \nu)}$$

and also

$$\epsilon_{\pi\pi\pi^0}^+ = \epsilon_{\pi\pi\pi^0}^- = \frac{1}{2}\frac{\text{Acceptance}(\pi^+\pi^-\pi^0)}{\text{Acceptance}(\pi^\pm e^\mp \nu)}$$

However, the acceptance for semileptonic decays to muons is given by a similar expression to the one above for electrons and thus

$$\epsilon_{\pi\mu\nu}^+ = \epsilon_{\pi\mu\nu}^- = \frac{\text{Acceptance}(\pi^\pm \mu^\mp \nu)}{\text{Acceptance}(\pi^\pm e^\mp \nu)}$$

The nominal values for these parameters are presented below. Their variation and its effect on the determination of the mass difference is discussed in section 6.6.

Parameters	Small eigentime	Large eigentime
$\epsilon_{\pi\mu\nu}^+ = \epsilon_{\pi\mu\nu}^-$	$(2.67 \pm 0.76) \times 10^{-2}$	$(3.25 \pm 0.19) \times 10^{-2}$
$\epsilon_{\pi\pi}^+ = \epsilon_{\pi\pi}^-$	$(0.71 \pm 0.32) \times 10^{-2}$	$(0.30 \pm 0.04) \times 10^{-2}$
$\epsilon_{\pi\pi\pi^0}^+ = \epsilon_{\pi\pi\pi^0}^-$	$(0.25 \pm 0.25) \times 10^{-2}$	$(0.05 \pm 0.01) \times 10^{-2}$

Effect on normalisations

In the previous section the normalisation factors η and ζ were determined assuming no background was present. It is now necessary to investigate whether these results are biased in any way by the presence of background. To do this I form simulated distributions, $N(E)_M$, by inserting the known decays rates $N(E)$ and $N(BG)$ and the parameters $\epsilon_{\pi\pi}$ etc. into equation 6.5 and the other three corresponding equations. When calculating these rates I use $\epsilon(e^-) = \epsilon(K^-) = 1$ and $\epsilon(K^+) = 1.139$ and $\epsilon(e^+) = 0.951$, i.e. the previously determined values. Using these simulated rates I calculate the ratios of equation 6.2 to get simulated normalisation parameters η_S and ζ_S. These can then be compared with the actual values of $\epsilon(K^+)/\epsilon(K^-)$ and $\epsilon(e^+)/\epsilon(e^-)$ used in the simulation.

Figures 6.3 and 6.4 show the simulated normalisations as a function of eigentime. In the figures the horizontal solid lines correspond to the input values of the normalisations. These are the results of the fits done in the previous chapter and the dashed horizontal lines are the $\pm 1\sigma$ values of the fits. The data points are also shown. The curves are the ratios calculated from the simulated rates i.e. if there were infinite statistics and if η and ζ were really constants then these curves are how the measured normalisations would look as functions of eigentime.

Above $10\tau_S$ (not shown in the figures) there is effectively no change in the normalisations, i.e., the measured values η_M and ζ_M are equal to the input values η and ζ and in particular are independent of eigentime. The differences arise at small eigentimes and are due to the two pion background. The shift in the kaon normalisation is very small, exceeding one standard deviation only below $3\tau_S$. It is also insensitive to a difference between $\epsilon^+_{\pi\pi}$ and $\epsilon^-_{\pi\pi}$

The final state normalisation ζ is however sensitive to a difference between $\epsilon^+_{\pi\pi}$ and $\epsilon^-_{\pi\pi}$, as shown in figure 6.4. Here varying $\epsilon^+_{\pi\pi}$ from 5% more to 5% less than $\epsilon^-_{\pi\pi}$ has a marked effect on the measured normalisation.

The data from which the normalisations were determined are almost exclusively above $3\tau_S$, where the background has little effect. Thus the values of η and ζ obtained in section 6.2 are unbiased by the background and accurate. For future work, however,

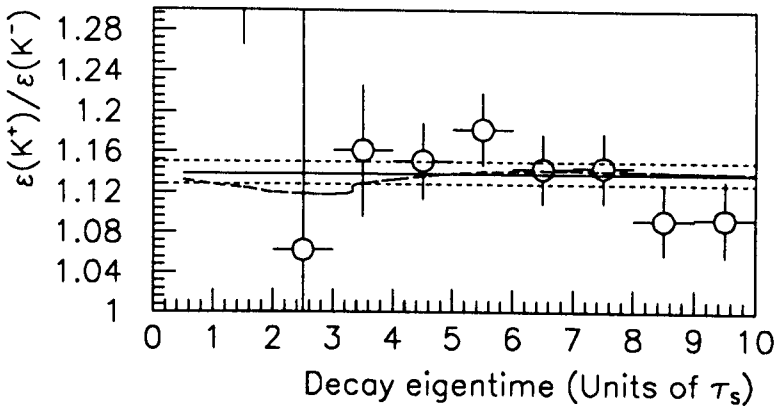

Figure 6.3: The effect of background on η.

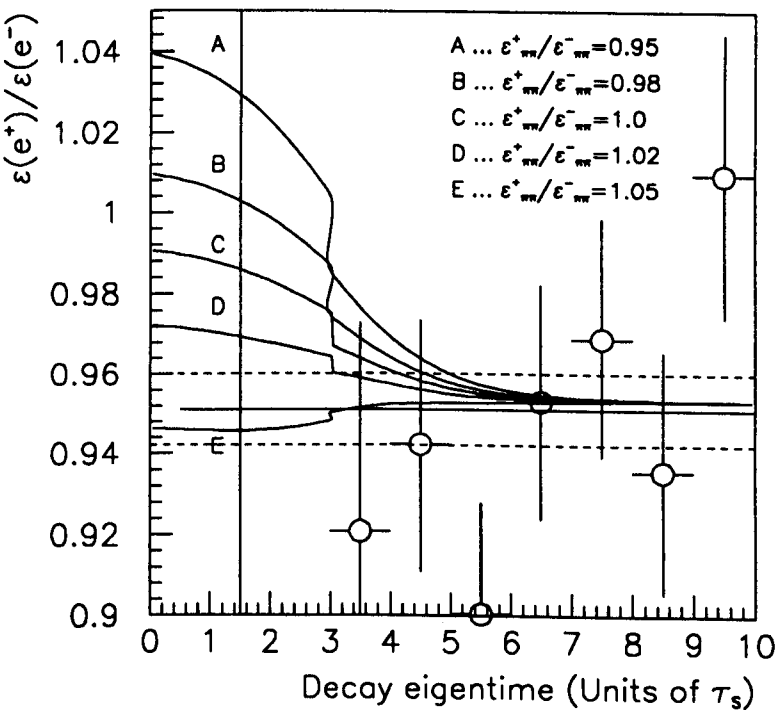

Figure 6.4: The effect of background on ζ.

which will require small eigentime asymmetries, this biasing effect must be taken into account. Either the normalisations must be determined from large eigentime data, or else (preferably) the effect of background must be considered explicitly by fitting for time dependent normalisation factors. It may therefore in the future be necessary to know both $\epsilon^+_{\pi\pi}$ and $\epsilon^-_{\pi\pi}$ separately.

Effect on the asymmetry

From the construction of $A_{\Delta m}$ it seems likely that the background in the numerator will cancel, whereas in the denominator it will not, hence reducing the size of the asymmetry. Taking equation 6.3 for $A_{\Delta m}$ and using equation 6.5 and the other three corresponding expressions, the background rates in the numerator factor to give

$$(N(K^+\pi^+\pi^-) - N(K^-\pi^+\pi^-))\left(\frac{\epsilon(e^+|\pi^+\pi^-)}{\epsilon(l^+|l^+)} - \frac{\epsilon(e^-|\pi^+\pi^-)}{\epsilon(l^-|l^-)}\right)$$

Below $5\tau_S$, where the effect of $\pi^+\pi^-$ background is greatest, the K^+ and K^- rates differ only at the level of CP violation, i.e. $\sim 10^{-3}$ of the total $K_S \to \pi^+\pi^-$ rate, whereas the ratios of the efficiencies differ only by a few percent and are in any case of the order of one percent. Thus this rate is less than 10^{-6} of the $K_S \to \pi^+\pi^-$ decay rate and is negligible.

In the denominator the background rates are all additive and $A_{\Delta m}$ becomes

$$A_{\Delta m} = \frac{N(\Delta S = 0) - N(\Delta S = 2)}{N(\Delta S = 0) + N(\Delta S = 2) + N(BG)}$$

where all of the efficiencies have been factored into $N(BG)$ which is given by

$$\begin{aligned} N(BG) &= 2\frac{\epsilon(e^+|\pi^+\pi^-)}{\epsilon(l^+|l^+)}\left(N(K^+\pi^+\pi^-) + N(K^-\pi^+\pi^-)\right) \\ &+ 2\frac{\epsilon(e^+|\pi^+\pi^-\pi^0)}{\epsilon(l^+|l^+)}\left(N(K^+\pi^+\pi^-\pi^0) + N(K^-\pi^+\pi^-\pi^0)\right) \end{aligned}$$

Thus $A_{\Delta m}$ can be related to A_0 by

$$A_{\Delta m}(t) = A_0(t)\frac{1}{1 + BG(t)} \tag{6.6}$$

where

$$BG(t) = N(BG)/(N(\Delta S = 0) + N(\Delta S = \pm 2))$$

i.e., the ratio of the number of background decays to the number of semileptonic decays.

6.4 Eigentime resolution

To consider the effect of finite eigentime resolution, I constructed smeared decay rates. The smeared rates, $N_S(E)$), are defined by

$$N_S(E)(t) = \int_0^\infty dT P(t|T) N(E)(T)$$

where $P(t|T)$ is the probability to measure the eigentime as t when the actual eigentime is T. Explicitly it is given by

$$P(t|T)dT = \frac{1}{\sqrt{\pi}} \frac{dT}{\sigma(T)} e^{-(t-T)^2/\sigma^2(T)}$$

where $\sigma(T)$ is the eigentime resolution as a function of eigentime. This is shown in figure 5.9 of section 5.5.3 and parametrized in the same section.

Taking the smeared rates I formed the asymmetry, $A_{\Delta m}$, and compared it with the asymmetry constructed from the unsmeared rates. The difference was less than 10^{-3} everywhere but in the first few τ_S. To give an idea of the scale of this change: on a plot of the asymmetry of the same scale as figure 6.5 there is no observable change in the shape of the asymmetry. I conclude that the eigentime resolution is sufficiently good that it can be ignored.

6.5 Determination of Δm

Making explicit the binned nature of the data, the measured asymmetry in the n^{th} bin is calculated as in equation 6.3

$$A^n_{\Delta m}(\text{measured}) = \frac{N^n(\Delta S = 0)_C - N^n(\Delta S = \pm 2)_C}{N^n(\Delta S = 0)_C + N^n(\Delta S = \pm 2)_C}$$

where $N^n(E)_C$ is the number of events of type E in the n^{th} bin, corrected by the appropriate normalisation factor. I wish to use a simple χ^2 minimisation to determine a value of the mass difference from the data and thus group together the bins at large eigentimes to get sufficient statistics in all bins. All of the structure of the asymmetry is below $15\tau_S$ and I use $1\tau_S$ wide bins in this region.

Bin number (n)	Eigentime region ($T^n_- - T^n_+$)
1	0-1
2	1-2
⋮	⋮
15	14-15
16	15-20
17	20-25
18	25-30
19	30-40
20	40-50

For a given value of the mass difference I can calculate for each bin an expected asymmetry, $A^n_{\Delta m}(\Delta m)$, where

$$A^n_{\Delta m}(\Delta m) = \frac{I^n(\Delta S = 0) - I^n(\Delta S = \pm 2)}{I^n(\Delta S = 0) + I^n(\Delta S = \pm 2)}$$

Having calculated the expected asymmetry for each bin, I calculate a χ^2_{df} function for the difference between the measured asymmetry and the calculated asymmetry†.

$$\chi^2_{df}(\Delta m) = \frac{1}{19}\sum_{n=1}^{20}\left(\frac{A^n_{\Delta m}(\Delta m) - A^n_{\Delta m}(\text{Measured})}{\sigma(A^n_{\Delta m}(\text{Measured}))}\right)^2$$

Using the minimisation routines in MINUIT [19] the mass difference is varied until a minimum of the function χ^2_{df} is found. MINUIT also returns a statistical uncertainty on the determined value of the mass difference.

There are two possible ways to calculate the expected asymmetry. The first is to take the functions I^n to be the rates evaluated at the centre values of each bin. In this case the predicted asymmetry in the n^{th} bin is equal to the function of equation 6.3 evaluated at $t = \frac{1}{2}(T^n_+ + T^n_-)$, where T^n_+ and T^n_- are the upper and lower edges of the bin. This method effectively ignores the binned nature of the data. It also has the disadvantage that it is not very amenable to a study of the systematics, since they have mainly been cancelled out in arriving at equation 6.3.

The more precise method is to take the functions I^n to be the decay rates integrated over the width of the bin. The expressions for these functions are long and are given

†There are twenty bins and one parameter is free to vary, thus giving nineteen degrees of freedom, i.e. $\chi^2_{df} = \chi^2/19$

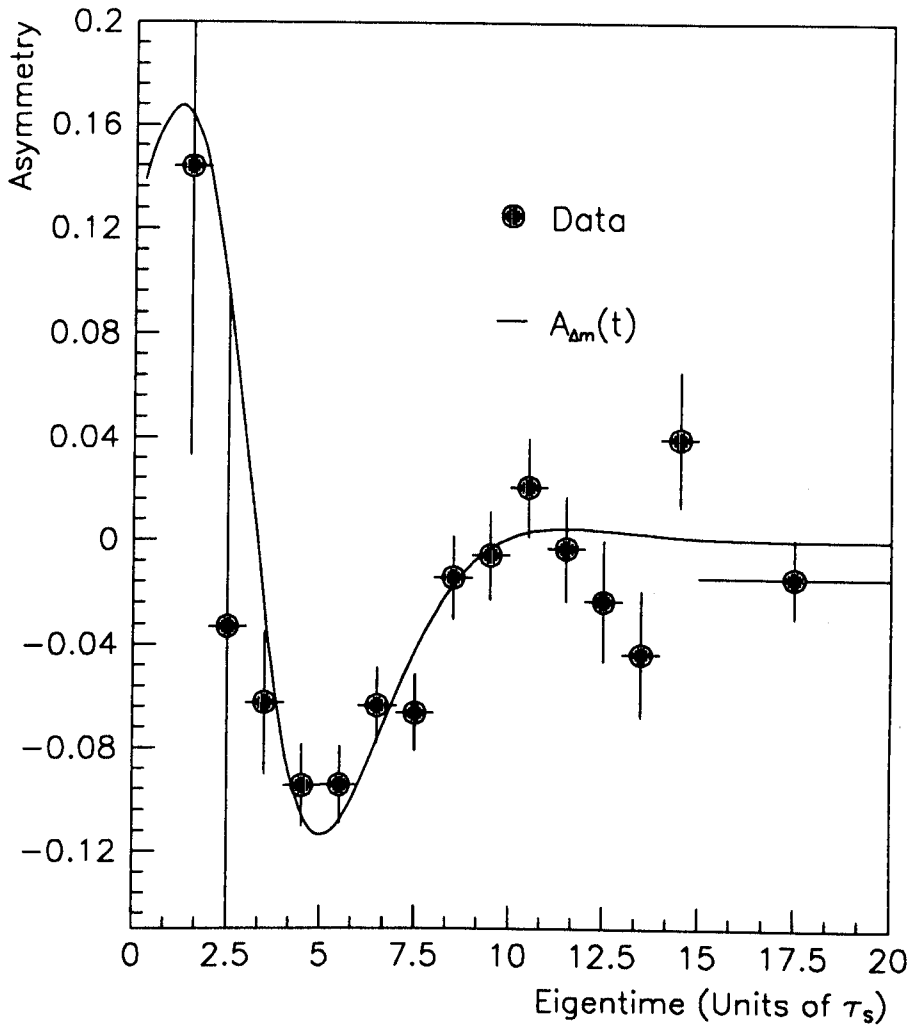

Figure 6.5: The measured asymmetry. The function $A_{\Delta m}(t)$, calculated with the fitted value $\Delta m/\gamma_S = 0.477$, is superposed.

in full in appendix B. This method also allows a study of the systematic effects of uncertainties in $\epsilon_{\pi\pi}$, η, etc..

Using this second (integral fit) method the mass difference is determined to be

$$\boxed{\Delta m/\gamma_S = 0.477 \pm 0.016}$$

with $\chi^2_{df}(0.477) = 1.32$. Figure 6.5 shows the measured asymmetry. The superposed curve is equation 6.6 with $\Delta m/\gamma_S = 0.477$.

The value of the mass difference obtained by fitting the measured asymmetry with the continuous function $A_{\Delta m}$ (i.e. the former method) is 0.4695 ± 0.0162 with the same χ^2_{df}. Thus the less precise fitting procedure introduces an error of -0.007 to the value of the mass difference.

The dependence of the value of the mass difference on the assumed values of the background levels etc. is discussed in the next section.

6.6 Systematic uncertainties

The fit to the measured asymmetry depends on the values of the parameters, η and ζ, and the background levels $\epsilon^+_{\pi\pi}$, $\epsilon^-_{\pi\pi}$ etc.. The uncertainty on the value of the mass difference returned by MINUIT (i.e. the statistical error) is further increased by the uncertainty in these parameters.

The table below shows the effect on the measured value of the mass difference of varying the normalisations and the background levels. The nominal values given refer to the large eigentime (i.e. $> 3\tau_S$) region and the range of variation refers to the actual change in the parameter, e.g. $\epsilon^+_{\pi\pi}$ is varied between $(3 - 0.7) \times 10^{-3}$ and $(3 + 3) \times 10^{-3}$. The change in the mass difference from the fitted value is shown in the final column.

Parameter	Nominal value	Range of variation	$\delta(\Delta m)$
$\left.\begin{matrix}\delta\eta/\eta \\ \delta\zeta/\zeta\end{matrix}\right\}$	0	$\left\{\begin{matrix}\pm 2\times 10^{-2} \\ \pm 2\times 10^{-2}\end{matrix}\right\}$	-10^{-4}
$\epsilon^{+}_{\pi\pi}$	$(3\pm 0.4)\times 10^{-3}$	$\begin{matrix}-7\times 10^{-4} \\ +3\times 10^{-3}\end{matrix}$	$\begin{matrix}+4\times 10^{-3} \\ +4\times 10^{-3}\end{matrix}$
$\frac{\epsilon^{+}_{\pi\pi}-\epsilon^{-}_{\pi\pi}}{\epsilon^{+}_{\pi\pi}}$	0	$0\rightarrow 10\%$	$+10^{-4}$
$\epsilon^{+}_{\pi\pi\pi^0}$	$(6\pm 1)\times 10^{-4}$	$\begin{matrix}-0.4\times 10^{-3} \\ +6\times 10^{-3}\end{matrix}$	$+4\times 10^{-5}$
$\frac{\epsilon^{+}_{\pi\pi\pi^0}-\epsilon^{-}_{\pi\pi\pi^0}}{\epsilon^{+}_{\pi\pi\pi^0}}$	0	$0\rightarrow 10\%$	$<10^{-5}$
$\epsilon^{+}_{\pi\mu\nu}$	$(6.5\pm 0.4)\times 10^{-2}$	$\pm 0.8\times 10^{-2}$	$<10^{-5}$
$\frac{\epsilon^{+}_{\pi\mu\nu}-\epsilon^{-}_{\pi\mu\nu}}{\epsilon^{+}_{\pi\mu\nu}}$	0	$\pm 10\%$	$<10^{-5}$

The background levels in the small and large eigentime regions are slightly different. However since the basic selection criteria are the same for both regions I take the levels to be correlated. Thus, for example, if I increase the value of $\epsilon^{+}_{\pi\pi}$ in the large eigentime region by one standard deviation above its nominal value, I also increase it by one standard deviation in the small eigentime region.

In section 6.2 it was shown that fractional errors in the normalisation parameters of the order of 10^{-2} lead to a small, almost constant offset in the asymmetry of the order 10^{-4}. The integral fit allows explicitly for small normalisation errors, i.e. $\delta\eta$ and $\delta\zeta$ non-zero. The bracketed entry in the table means that both $\delta\eta/\eta$ and $\delta\zeta/\zeta$ were simultaneously and independently varied over the range ± 2 standard deviations around zero. The largest effect is a reduction in the mass difference by 10^{-4}. Since both normalisations are determined from the data their errors and hence their contribution to the uncertainty of the mass difference will decrease with increased statistics.

I have also investigated the effect of using time dependent normalisations. Since the normalisations were measured in each eigentime bin, it is possible to apply the normalisation correction factors, η and ζ, bin-by-bin. This results in an increase in the fitted value of $\Delta m/\gamma_S$ of 2×10^{-4}.

The dominant source of uncertainty in the mass difference is due to the level of two pion background which is mainly determined by the probability for a pion to be identified as an electron. In section 5.5.2 I set an upper limit to the two pion acceptance of approximately twice the nominal value. Thus to determine the uncertainty in the

mass difference I must double $\epsilon^+_{\pi\pi}$ and $\epsilon^-_{\pi\pi}$. It is also necessary to explore the effect of $\epsilon^+_{\pi\pi} \neq \epsilon^-_{\pi\pi}$. From the data $\epsilon(e^+)/\epsilon(e^-) \sim 0.95$, and thus it seems at least possible that $\epsilon(e^+|\pi^+\pi^-) \neq \epsilon(e^-|\pi^+\pi^-)$. In the absence of a detailed study of the origin of the charge asymmetry It is not even clear which of $\epsilon(e^+|\pi^+\pi^-)$ or $\epsilon(e^-|\pi^+\pi^-)$ will be the bigger. To cover all possibilities I vary the ratio over the range

$$0.95 < \frac{\epsilon(e^+|\pi^+\pi^-)}{\epsilon(e^-|\pi^+\pi^-)} < (0.95)^{-1}$$

Taking $\epsilon(e^+)/\epsilon(e^-) = 0.95$ this then translates into a range of values for $\epsilon^+_{\pi\pi}$ and $\epsilon^-_{\pi\pi}$. Taking

$$\frac{\epsilon(e^+|\pi^+\pi^-)}{\epsilon(e^-|\pi^+\pi^-)} = 1$$

gives

$$\epsilon^+_{\pi\pi} = 0.513\frac{\text{Acceptance}(\pi^+\pi^-)}{\text{Acceptance}(\pi^\pm e^\mp \nu)}$$

and

$$\epsilon^-_{\pi\pi} = 0.488\frac{\text{Acceptance}(\pi^+\pi^-)}{\text{Acceptance}(\pi^\pm e^\mp \nu)}$$

thus giving

$$\frac{\epsilon^+_{\pi\pi} - \epsilon^-_{\pi\pi}}{\epsilon^+_{\pi\pi}} = 0.049 \text{ i.e. } 5\%$$

Similarly taking $\epsilon(e^+|\pi^+\pi^-) \neq \epsilon(e^-|\pi^+\pi^-)$ gives

$$\epsilon^+_{\pi\pi} = \epsilon^-_{\pi\pi} \quad \text{for} \quad \frac{\epsilon(e^+|\pi^+\pi^-)}{\epsilon(e^-|\pi^+\pi^-)} = 0.95$$

and

$$\frac{\epsilon^+_{\pi\pi} - \epsilon^-_{\pi\pi}}{\epsilon^+_{\pi\pi}} = 0.097 \text{ i.e. } 10\% \quad \text{for} \quad \frac{\epsilon(e^+|\pi^+\pi^-)}{\epsilon(e^-|\pi^+\pi^-)} = (0.95)^{-1}$$

Thus for the range of $\epsilon(e^+|\pi^+\pi^-)/\epsilon(e^-|\pi^+\pi^-)$ considered $(\epsilon^+_{\pi\pi} - \epsilon^-_{\pi\pi})/\epsilon^+_{\pi\pi}$ varies from 0 to 10%. Similar figures hold for the three pion final state.

Since the two pion decays fall off with the K_S lifetime they mainly affect the small eigentime region. Figure 6.6 shows the effect on the shape of the $A_{\Delta m}$ curve of varying $\epsilon^+_{\pi\pi}$ and $\epsilon^+_{\pi\pi\pi^0}$. Though there is a very large change in the curve below about $4\tau_S$ there is little change at later eigentimes. These small eigentime points have large errors and have little effect on the χ^2_{df} and thus on the value of the mass difference determined by the fit. The systematic uncertainty in the mass difference due to the two pion decays is only 0.8% compared to the statistical uncertainty of around 3%.

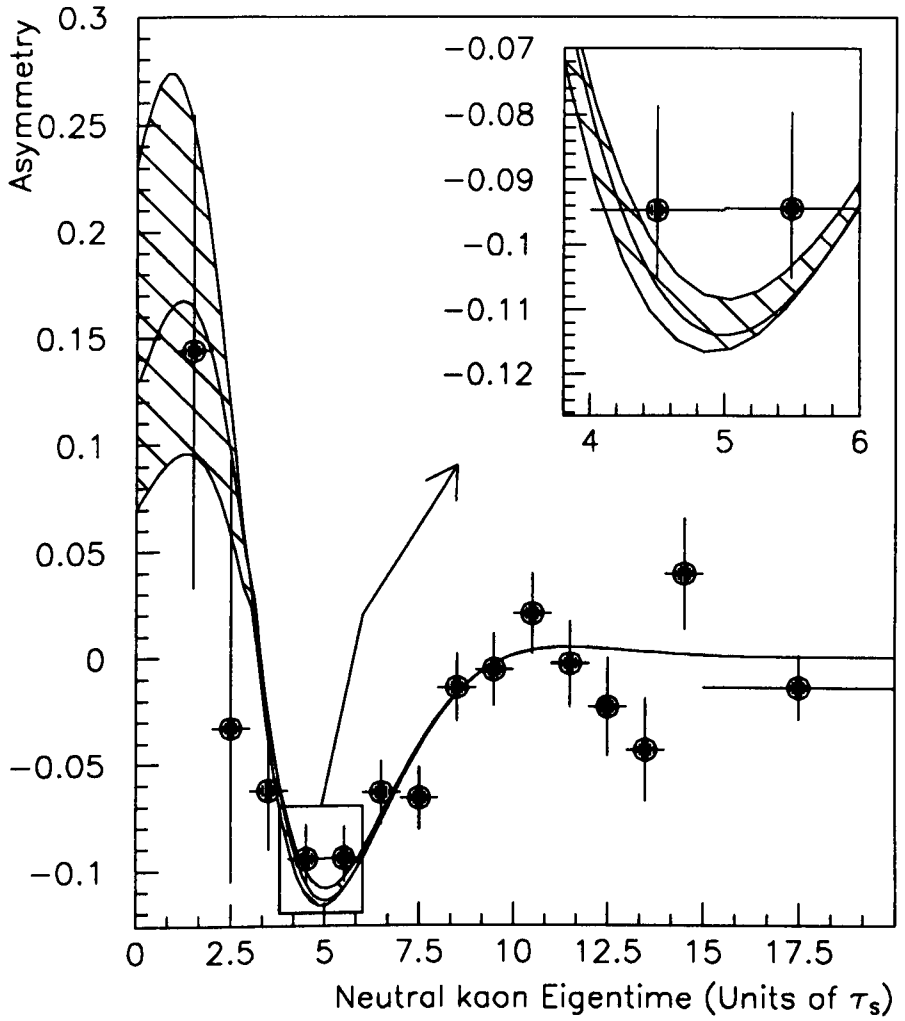

Figure 6.6: The effect of varying the level of background on the shape of the function $A_{\Delta m}(t)$. In this plot $\epsilon_{\pi\pi}$ is varied from 50% to 200% of its nominal value and $\epsilon_{\pi\pi\pi^0}$ is varied from 0 to 500% of its value. The shaded region is swept out as the background levels change. The data points are shown for comparison.

The mass difference is insensitive to the level of three pion background, doubling the amount increases the mass difference by only 4×10^{-5}. Similarly variations in the size of the contribution to the signal from muonic final states has negligible effect on the mass difference.

In addition to these parameters, the fit is dependent on the values of branching ratios and on the widths of the long and short lived eigenstates, all of which I have taken from the Particle Data Book [4]. The values I take for these quantities are listed in appendix B. The errors on the branching ratios are all less than 2% and since they only appear multiplied by one of the parameters above ($\epsilon^{+}_{\pi\pi}$ etc.) small variations in the branching ratios have no effect on Δm above that of varying the parameters, i.e. $\epsilon^{+}_{\pi\pi}$ etc.

The second largest source of uncertainty comes from variations in γ_S Varying γ_L by $\pm2\sigma$ changes the mass difference by only 10^{-4}, whereas changing γ_S by the same amount changes the mass difference by $\pm10^{-3}$.

To sum up the uncertainty in the mass difference due to background decay levels and uncertainties in various parameters of the system is about a quarter the size of the statistical uncertainty. Its main source is due to uncertainties in the level of two pion background.

$$\Delta m/\gamma_S(\text{systematic uncertainty}) = \begin{cases} +0.004 \\ -0.001 \end{cases}$$

Chapter 7

Conclusion

7.1 Mass difference determination

In this thesis, it has been shown that electron identification using the particle identification subdetector is possible. Electrons can be identified with a mean efficiency of 60 % between 70 MeV/c and 180 MeV/c, falling linearly off to about 10 % at 250 MeV/c. The probability for a pion to be identified as an electron is approximately constant at 1 % over all of this momentum region.

Event selection, based on this electron identification technique, has resulted in a final sample of 44 000 neutral kaon semileptonic decays. From this data I have constructed a time dependent asymmetry and determined a value of the $K_L - K_S$ mass difference. The value obtained is

$$\boxed{\Delta m/\gamma_S = 0.477 \pm 0.016(\text{stat.}) \left.\begin{matrix} +0.004 \\ -0.001 \end{matrix}\right\} (\text{syst.})}$$

Though not competitive with the most recent measurements, this result is very preliminary. The major systematic error is due to uncertainty in the level of $\pi^+\pi^-$ background in the final event sample. This uncertainty has two sources. Low statistics in the pion track sample, especially at momenta below 100 MeV/c, make it difficult to accurately measure the pion contamination probability which is necessary for the Monte Carlo estimation of the background level. Secondly the low statistics in the Monte Carlo data available at the time of the analysis means that very few background events passed the selection criteria and hence the precision on the estimated

acceptance is limited. Increased statistics in both data and Monte Carlo simulation will lead to a reduction in this systematic uncertainty.

7.2 Future prospects

Though it is not used anywhere in this thesis, the electromagnetic calorimeter is now operational. An algorithm has been developed to separate electrons and pions using the shape of the showers produced. It is useful only for tracks with a momentum above 200 MeV/c. Preliminary results show that, keeping the pion contamination to 1 %, gives at least a 30 % efficiency for electron selection from 200 MeV/c to the top of the electron momentum spectrum around 500 MeV/c. Since two thirds of the electrons in semileptonic decays have momenta above 180 MeV/c, this means that the use of electrons identified by the calorimeter will approximately double the semileptonic acceptance (as defined in section 5.5.2) from 7 % to 14 %.

The completion of the trigger will also increase the number of semileptonic decays at smaller eigentimes. Since kinematics is used online to bias the trigger against $\pi^+\pi^-$ decays, the IDL 4 trigger need no longer be used to collect semileptonic decays in sufficient numbers. Decays with a secondary vertex inside the proportional chambers will not be dominated by $\pi^+\pi^-$ decays.

For improving the measurement of Δm, small eigentime decays are important. The position and depth of the dip in the asymmetry $A_{\Delta m}$ is more tightly constrained when data is available on both the falling and rising edges.

The experimental proposal aims at achieving an accuracy on the mass difference of $\delta(\Delta m)/\Delta m \sim 2-3\times 10^{-3}$. Since there is at present no data available using the full trigger, it is impossible to quote exact numbers. However, using the data from period 8 (before the problems of the Čerenkov inefficiency) I can make a crude estimate as to the expected precision of a future measurement.

During Period 8 a total of 3×10^{11} antiprotons passed through the beam counter. From these 2.5×10^7 events were written to tape, 42 % of which were taken with trigger configuration 433, the remainder with 233. From the large eigentime data (i.e. T433) a total 8 300 semileptonic decays have been isolated.

To estimate the possible precision on a measurement of Δm I assume 10^{13} antiprotons will be collected. The efficiency for isolating semileptonic decays is doubled by the inclusion of electrons identified by the calorimeter. An accurate prediction for the total number of semileptonic decays that will be collected, however, requires a knowledge of what trigger configuration data will be collected with.

A lower limit to the number of events and hence the precision on the mass difference can be estimated from just these factors. A factor of thirty-three for the total number of annihilations and a factor of two for the calorimeter, gives just over half a million events. This gives a statistical error on $\Delta m/\gamma_S$ of ~ 0.005.

Preliminary results from 1992 data, collected with the full trigger, suggest that the number of semileptonic events will be a factor three more than quoted above, reducing the statistical error to ~ 0.003. This data should be collected before the end of 1993.

Blank Page

Appendix A

Constrained fits

An event consists of a number of charged tracks, intersecting at one or more vertices. In general there may also be unseen neutral particles associated with some vertices. An **event hypothesis** consists of assuming a particle type for each charged track and each neutral. The information available from an event consists of a set of measured momenta, $\boldsymbol{p}^m(a)$, $a = 1,2,3....$ A constrained (or kinematic) fit, for a particular hypothesis, may be applied if the application of four momentum conservation at each vertex leads to an over-constrained set of equations. In general due to momentum resolution the measured momenta will not satisfy these equations.

A constrained fit aims to do two things; to find a set of fitted momenta which do satisfy four momentum conservation, and to test the likelihood of the hypothesis being correct.

Denoting the fitted momenta $\boldsymbol{p}^f(a)$, the fit aims to find the values of these momenta closest to the measured values, subject to the constraints of four-momentum conservation at each vertex. These values are found by minimising a χ^2 function, defined by

$$\chi^2 = \sum_a (p_i^m(a) - p_i^f(a)) E_{ij}^{-1}(a) (p_j^m(a) - p_j^f(a)) \qquad \text{(A.1)}$$

where $E_{ij}(a)$ is the ij^{th} element of the momentum error matrix of track a. Note that since the neutral tracks have no measured momenta, the summation extends only over charged tracks.

If the fitted values of the momenta were unconstrained then the fitted momenta

would be equal to the measured momenta and the χ^2 would be identically zero. However the constraint of four-momentum conservation at each vertex means that the fitted components of the momenta cannot be varied independently, thus giving a non-zero value for χ^2.

In addition to giving the values of the momenta of the charged tracks the momenta of any neutral, unseen, tracks is also determined. This is a direct result of four-momentum conservation.

As an example consider a golden event primary vertex, $p\bar{p} \rightarrow K^- K^0 \pi^+$. The measured momenta are $\boldsymbol{p}^m(K^-)$ and $\boldsymbol{p}^m(\pi^+)$. The fitted momenta are $\boldsymbol{p}^f(K^-)$, $\boldsymbol{p}^f(\pi^+)$ and $\boldsymbol{p}^f(K^0)$ and these are subject to the constraints

$$\begin{aligned} \boldsymbol{p}^f(K^-) + \boldsymbol{p}^f(\pi^+) + \boldsymbol{p}^f(K^0) &= \mathbf{o} \\ E(K^-) + E(\pi^+) + E(K^0) &= 2m_p c^2 \end{aligned} \tag{A.2}$$

The χ^2 function is defined by

$$\begin{aligned} \chi^2 = &(p_i^m(K^-) - p_i^f(K^-))E_{ij}^{-1}(K^-)(p_j^m(K^-) - p_j^f(K^-)) \\ &+(p_i^m(\pi^+) - p_i^f(\pi^+))E_{ij}^{-1}(\pi^+)(p_j^m(\pi^+) - p_j^f(\pi^+)) \end{aligned}$$

The fit program varies the fitted momenta of the charged tracks, in an attempt to minimise the χ^2, but always subject to the constraints of equations A.2. The three unknowns of the neutral kaon momentum are removed by the first of these equations and then one of the components of the charged track momenta becomes a dependent variable because of the fourth constraint. The term, 1C, refers to this one dependent variable. Once the fitted values of the momentum are found for the charged kaon and pion, the neutral kaon momentum is given by the constraint equations.

The second aim of the constrained fit is to test the likelihood of the assumed hypothesis being correct. This is done by comparing the value of χ^2 with a standard function and determining the probability that the hypothesis of the event and the measured momenta are consistent to within the magnitude of the momentum resolution. The size of the measured χ^2 depends on the number of dependent momenta in equation A.1. A 1C fit has one dependent vector component, a 2C fit has two, etc..

Thus the χ^2 is compared with different functions depending on the number of dependent variables. For a correct hypothesis the returned probability should be distributed evenly between zero and one.

If the hypothesis is wrong then the fit should return a small probability. However within the limits of the momentum resolution some (different) decay types look very similar and thus different hypotheses can be fitted with similar probabilities. These decay channels cannot be distinguished from kinematics alone, for example $K^0 \rightarrow \pi e \nu$ and $K^0 \rightarrow \pi \mu \nu$ cannot be separated.

Further details of constrained fits can be found in [20].

Blank Page

Appendix B

Transition rates

The eigentime dependence for those neutral kaon decay processes important for this thesis are listed below. The notation $N(K^q X^+ X^- X^0)$ represents an event with a primary charged kaon of charge q, with a final decay state $X^+X^-X^0$). A shorthand is used for the semileptonic decays, e.g. $N(K^+e^+)$ stands for $N(K^+\pi^-e^+\nu)$.

Semileptonic decays

$$\boxed{\begin{aligned} N(K^+e^+) &= \tfrac{1}{4}W_{\pi e\nu}(1+4Re(\epsilon))g(t) \\ N(K^+e^-) &= \tfrac{1}{4}W_{\pi e\nu}f(t) \\ N(K^-e^+) &= \tfrac{1}{4}W_{\pi e\nu}f(t) \\ N(K^-e^-) &= \tfrac{1}{4}W_{\pi e\nu}(1-4Re(\epsilon))g(t) \end{aligned}}$$

$$\begin{aligned} f(t) &= e^{-\gamma_L t} + e^{-\gamma_S t} + 2e^{-\frac{1}{2}(\gamma_L+\gamma_S)t}\cos(\Delta m t) \\ g(t) &= e^{-\gamma_L t} + e^{-\gamma_S t} - 2e^{-\frac{1}{2}(\gamma_L+\gamma_S)t}\cos(\Delta m t) \end{aligned}$$

$$W_{\pi e\nu} = \gamma_L BR(K_L \to \pi e\nu)$$

$\pi^+\pi^-$ decays

$$\boxed{\begin{aligned} N(K^+\pi^+\pi^-) &= \tfrac{1}{2}(1+2Re(\epsilon))W_{\pi\pi}F(t) \\ N(K^-\pi^+\pi^-) &= \tfrac{1}{2}(1-2Re(\epsilon))W_{\pi\pi}G(t) \end{aligned}}$$

$$F(t) = e^{-\gamma_S t} + |\eta_{+-}|^2 e^{-\gamma_L t} - 2|\eta_{+-}| e^{-\frac{1}{2}(\gamma_L+\gamma_S)t} \cos(\Delta m t - \phi_{+-})$$

$$G(t) = e^{-\gamma_S t} + |\eta_{+-}|^2 e^{-\gamma_L t} + 2|\eta_{+-}| e^{-\frac{1}{2}(\gamma_L+\gamma_S)t} \cos(\Delta m t - \phi_{+-})$$

$$W_{\pi\pi} = \gamma_S BR(K_S \to \pi^+\pi^-)$$

$\pi^+\pi^-\pi^0$ decays

$$\boxed{N(K^\pm\pi^+\pi^-\pi^0) = \tfrac{1}{2} W_{\pi\pi\pi^0} e^{-\gamma_L t}}$$

$$W_{\pi^+\pi^-\pi^0} = \gamma_L BR(K_L \to \pi^+\pi^-\pi^0)$$

Parameter values

The following quantities are taken from the particle data book [4]

$$\begin{aligned}
\gamma_S &= 7.377 \times 10^{-12} \text{ MeV} \\
&= 1.121 \times 10^{10} \text{s}^{-1} \\
\gamma_L &= 1.271 \times 10^{-14} \text{ MeV} \\
&= 1.93 \times 10^{7} \text{s}^{-1} \\
Re(\epsilon) &= 0.00162 \\
|\eta_{+-}| &= 0.00227 \\
BR(K_L \to \pi e \nu) &= 38.6\% \\
BR(K_L \to \pi \mu \nu) &= 27.0\% \\
BR(K_L \to \pi^+\pi^-\pi^0) &= 12.37\% \\
BR(K_S \to \pi^+\pi^-) &= 68.61\%
\end{aligned}$$

Appendix C

Integral fit

I present here the explicit form of the functions used in section 6.5 to fit for the mass difference. The asymmetry expected in bin n for a mass difference value of Δm is given by

$$A^n_{\Delta m}(\Delta m) = \frac{I^n(\Delta S = 0) - I^n(\Delta S = \pm 2)}{I^n(\Delta S = 0) + I^n(\Delta S = \pm 2)}$$

where

$$I^n(\Delta S = 0) = (1 + \frac{\delta\eta}{\eta})I^n_{-+} + (1 + \frac{\delta\zeta}{\zeta})I^n_{+-}$$

and

$$I^n(\Delta S = \pm 2) = I^n_{++} + (1 + \frac{\delta\eta}{\eta})(1 + \frac{\delta\zeta}{\zeta})I^n_{--}$$

The quantities I^n_{++} etc. are derived by integrating equation 6.4 and the three corresponding functions over the interval of the n^{th} bin. The upper and lower edges of the bin are denoted T^n_+ and T^n_-. As an example of consider I^n_{-+}

$$\begin{aligned} I^n_{-+} &= \epsilon^+_l \int_{T^n_-}^{T^n_+} N(K^-e^+)(t)dt + \epsilon^+_{\pi\pi} \int_{T^n_-}^{T^n_+} N(K^-\pi^+\pi^-)(t)dt \\ &+ \epsilon^+_{\pi\pi\pi^0} \int_{T^n_-}^{T^n_+} N(K^-\pi^+\pi^-\pi^0)(t)dt \end{aligned}$$

where

$$\epsilon^\pm_l = \left(1 + \epsilon^\pm_{\pi\mu\nu} \frac{BR(K_L \to \pi\mu\nu)}{BR(K_L \to \pi e\nu)}\right)$$

i.e., the electron and muon type semileptonic events are combined. The quantities $\epsilon^\pm_f$ are as per section 6.6, e.g.

$$\epsilon^+_{\pi\pi} = \frac{\epsilon(e^+|\pi^+\pi^-)}{\epsilon(e^+)}$$

There values are given in the same section. The integrals are performed using the rates from the equations presented in the previous section

$$\begin{aligned}\int_{T_-^n}^{T_+^n} N(K^-e^+)(t)dt &= \frac{1}{4}W_{\pi e\nu}(1+4Re(\epsilon))\int_{T_-^n}^{T_+^n} g(t)dt \\ &= \frac{1}{4}W_{\pi e\nu}(1+4Re(\epsilon))(N_L^n+N_S^n-2N_{LS}^n(0))\end{aligned}$$

$$\begin{aligned}\int_{T_-^n}^{T_+^n} N(K^-\pi^+\pi^-)(t)dt &= \frac{1}{2}W_{\pi\pi}(1-2Re(\epsilon))\int_{T_-^n}^{T_+^n} G(t)dt \\ &= \frac{1}{2}W_{\pi\pi}(1-2Re(\epsilon))\left(N_S^n+|\eta_{+-}|^2 N_L^n+2|\eta_{+-}|N_{LS}^n(\phi_{+-})\right)\end{aligned}$$

$$\begin{aligned}\int_{T_-^n}^{T_+^n} N(K^-\pi^+\pi^-\pi^0)(t)dt &= \frac{1}{2}W_{\pi\pi\pi^0}\int_{T_-^n}^{T_+^n} e^{-\gamma_L t}dt \\ &= \frac{1}{2}W_{\pi\pi\pi^0}N_L^n\end{aligned}$$

The functions N_S^n, N_L^n and N_{LS}^n are given by

$$N_L^n = \int_{T_-^n}^{T_+^n} dt\, e^{-\gamma_L t} = \frac{1}{\gamma_L}\left(e^{-\gamma_L T_-^n} - e^{-\gamma_L T_+^n}\right)$$

$$N_S^n = \int_{T_-^n}^{T_+^n} dt\, e^{-\gamma_S t} = \frac{1}{\gamma_S}\left(e^{-\gamma_S T_-^n} - e^{-\gamma_S T_+^n}\right)$$

$$N_{LS}^n(\phi) = \int_{T_-^n}^{T_+^n} dt\, e^{-\frac{1}{2}(\gamma_S+\gamma_L)t}\cos(\Delta m t-\phi) =$$

$$\frac{2(\gamma_S+\gamma_L)}{4\Delta m^2+(\gamma_S+\gamma_L)^2}\left[e^{-\frac{1}{2}(\gamma_S+\gamma_L)t}\left(\frac{2\Delta m}{(\gamma_S+\gamma_L)}\sin(\Delta m t-\phi)+\cos(\Delta m-\phi)\right)\right]_{T_-^n}^{T_+^n}$$

The other three quantities, I_{--}^n, I_{++}^n and I_{+-}^n are calculated similarly and all four expressions are presented below for completeness

$$\begin{aligned}I_{++}^n &= \frac{1}{4}\epsilon_l^+ W_{\pi e\nu}(1+4Re(\epsilon))(N_L^n+N_S^n-2N_{LS}^n(0)) \\ &+ \frac{1}{2}\epsilon_{\pi\pi}^+ W_{\pi\pi}(1+2Re(\epsilon))\left(N_S^n+|\eta_{+-}|^2 N_L^n-2|\eta_{+-}|N_{LS}^n(\phi_{+-})\right) \\ &+ \frac{1}{2}\epsilon_{\pi\pi\pi^0}^+ W_{\pi\pi\pi^0}N_L^n\end{aligned}$$

$$\begin{aligned}I_{+-}^n &= \frac{1}{4}\epsilon_l^- W_{\pi e\nu}(N_L^n+N_S^n+2N_{LS}^n(0)) \\ &+ \frac{1}{2}\epsilon_{\pi\pi}^- W_{\pi\pi}(1+2Re(\epsilon))\left(N_S^n+|\eta_{+-}|^2 N_L^n-2|\eta_{+-}|N_{LS}^n(\phi_{+-})\right) \\ &+ \frac{1}{2}\epsilon_{\pi\pi\pi^0}^- W_{\pi\pi\pi^0}N_L^n\end{aligned}$$

$$
\begin{aligned}
I^n_{-+} &= \frac{1}{4}\epsilon_l^+ W_{\pi e\nu}\left(N_L^n + N_S^n + 2N_{LS}^n(0)\right) \\
&+ \frac{1}{2}\epsilon_{\pi\pi}^+ W_{\pi\pi}(1 - 2Re(\epsilon))\left(N_S^n + |\eta_{+-}|^2 N_L^n + 2|\eta_{+-}| N_{LS}^n(\phi_{+-})\right) \\
&+ \frac{1}{2}\epsilon_{\pi\pi\pi^0}^+ W_{\pi\pi\pi^0} N_L^n
\end{aligned}
$$

$$
\begin{aligned}
I^n_{--} &= \frac{1}{4}\epsilon_l^- W_{\pi e\nu}(1 - 4Re(\epsilon))\left(N_L^n + N_S^n - 2N_{LS}^n(0)\right) \\
&+ \frac{1}{2}\epsilon_{\pi\pi}^- W_{\pi\pi}(1 - 2Re(\epsilon))\left(N_S^n + |\eta_{+-}|^2 N_L^n + 2|\eta_{+-}| N_{LS}^n(\phi_{+-})\right) \\
&+ \frac{1}{2}\epsilon_{\pi\pi\pi^0}^- W_{\pi\pi\pi^0} N_L^n
\end{aligned}
$$

References

[1] Frederik J. Gilman & Yosef Nir, Quark mixing: the CKM picture, Annu. Rev. Nucl. Part. Sci. 1990. 40: 213-38

[2] L.Adiels et al., CPLEAR Proposal, CERN/PSCC/85-6 (1985).

[3] S. Bard et al., Part. Accel. 26: 223-228 (1990)

[4] Particle data group, Review of particle properties, Phys. Rev. **D45** (1992)

[5] M. Cullen et al., A precision determination of the $K_L - K_S$ mass difference, Phys. Lett. **32B** 523 (1970)

[6] C. Geweniger et al., Measurement of the kaon mass difference $m_L - m_S$ by the two regenerator method, Phys. Lett. **52B** 108 ((1974)

[7] S. Gjesdal et al., A measurement of the $K_L - K_S$ mass difference from the charge asymmetry in semileptonic decays, Phys. Lett. **52B** 113 ((1974)

[8] Particle data group, Review of particle properties, Phys. lett. **170B** 132 (1986)

[9] I.J.R. Aitchison & A.J.G. Hey, Gauge theories in particle physics (second edition), Pub. Adam Hilger (1989)

[10] W. A. Mehlhop et al., Interference between neutral kaons and their mass difference, Phys. Rev. **172** 1613 (1968)

[11] E. Paul, Status of interference experiments with neutral kaons, in Springer Tracts in Modern Physics 79: Elementary Particle physics, Pub. Springer-Verlag

[12] M. Luke, Phys. Lett. B256:265-266 (1991)

[13] M. van den Putte et al., $\bar{p}$-beam monitoring system for CPLEAR, IEEE Transactions in Nuclear Science Volume 37 p 53.

[14] M. Dejardin, Nucl. Instr. and Meth. A283 p 484.

[15] A.Angelopoulos et al., The CPLEAR particle identification detector, Nucl. Instr. and Meth. A311 (1992) 78.

[16] P. Bloch et al., Development of small high gain tubes for the electromagnetic calorimeter of the CPLEAR detector, Nucl. Instr. and Meth. A297 (1990) 126.

[17] R. Adler et al., Design and test of a prototype gas-sampling calorimeter of high granularity for the CPLEAR experiment, CERN–PPE/92–68 (submitted to Nucl. Instr. and Meth.)

[18] R. Fernow, Introduction to experimental particle physics, Pub. Cambridge University Press (1986).

[19] Function minimization and error analysis, CERN program library entry D506.

[20] J. P. Berge et al., Kinematical analysis of interaction vertices from bubble chamber data, The Review of Scientific Instruments **32** (1961) p 538.